PHYSIK-DEPARTMENT

Development and Performance Studies of a Small Animal Positron Emission Tomograph with Individual Crystal Readout and Depth of Interaction Information
and
Studies of Novel Detector Technologies in Medical Imaging

Dissertation
von
Virginia C. Spanoudaki

TECHNISCHE UNIVERSITÄT
MÜNCHEN

Fakultät für Physik der Technischen Universität München
Physik Department E18

Klinikum rechts der Isar der Technischen Universität München
Nuklearmedizinische Klinik und Poliklinik

Development and Performance Studies of a Small Animal Positron Emission Tomograph with Individual Crystal Readout and Depth of Interaction Information and Studies of Novel Detector Technologies in Medical Imaging

Virginia C. Spanoudaki

Vollständiger Abdruck der von der Fakultät für Physik der Technischen Universität München zur Erlangung des akademischen Grades eines

Doktors der Naturwissenschaften (Dr. rer. nat.)

genehmigten Dissertation.

Vorsitzender:	Univ.-Prof. Dr. W. Weise
Prüfer der Dissertation:	
	1. Univ.-Prof. Dr. St. Paul
	2. Univ.-Prof. Dr. R. Senekowitsch-Schmidtke

Die Dissertation wurde am 10. März 2008 bei der Technischen Universität München eingereicht und durch die Fakultät für Physik am 2. April 2008 angenommen.

This work is dedicated to my sister Eirini who has been and will always be the voice in my head telling me to keep going on...

Aderfoula I love you so much!

Abstract

The Munich Avalanche Diode PET–II (MADPET–II) is a positron emission tomograph aimed for radiopharmaceutical studies in mice and rats. The novel detector architecture of this system is based on readout of Lutetium Oxyorthosilicate (LSO) scintillation crystal arrays by Avalanche Photodiode (APD) arrays. In addition, a dual radial detector layer allows for extraction of depth of interaction information, thus improving the spatial resolution at the edges of the field of view (FOV). The scanner comprises of a total of 1152 LSO-APD detectors which are processed individually by the same number of electronic channels, providing time and energy information for each channel. The individual crystal readout minimizes the system's dead time and allows for detection of Compton scatter events between the discrete crystal elements. The tomograph has a mean energy resolution of 22% and a temporal resolution of 10 ns (FWHM). The dependence of these values on various factors, such as the performance of signal processing electronics, the temperature and the detector bias has been studied. A reconstructed spatial resolution of 1.3 mm at the center of the FOV has been measured. Experimental results show a good compromise between spatial resolution and sensitivity, which is expected to further improve if intercrystal scatter is taken into account. A preliminary assessment of the tomograph imaging capability has been realized by performing an animal scan.

PET/CT, which is currently implemented in clinical routine, combines two different imaging modalities thereby measuring both, anatomical and functional information. PET/MR is an alternative multimodal imaging technique which provides higher contrast in soft tissues while minimizing the radiation dose received by the patient. However, it requires a more sophisticated detector design that does not create interference between the two modalities. The feasibility of using silicon photomultipliers (SiPMs), a promising new photodetector, in PET/MR has been investigated. Attractive features of these devices are their high gain, their fast timing and their insensitivity to magnetic fields. Experimental results with single channel devices coupled to scintillation crystals exhibit a comparable energy resolution and a superior time resolution compared to LSO-APD detectors even by eliminating the need for complicated amplification electronics. Operation under the presence of magnetic fields has not shown degradation of the mentioned performance. A detector concept based on 1×1 mm^2 scintillation crystals coupled individually to arrays of 1×1 mm^2 SiPMs is considered the appropriate approach for submillimeter resolution PET imaging.

Kurzfassung

Der MADPET-II Tomograph (Munich Avalanche Diode PET-II) ist ein Positronen-Emissions-Tomograph, der für Studien von Radiopharmaka an Mäusen und Ratten ausgelegt ist. Der neuartige Detektoraufbau des Systems basiert auf eins-zu-eins Kopplung von Lutetium Oxyorthosilikat (LSO) Kristallen und Lawinen-Photodioden (APDs). Eine zusätzliche zweite radiale Detektorlage ermöglicht es, Informationen über die Tiefe der Wechselwirkung von 511 keV Gammaquanten im Kristall (depth of interaction, DOI) zu gewinnen. Hierdurch wird die Ortsauflösung am Rand des Gesichtsfeldes verbessert. Der Tomograph besteht aus 1152 unabhängigen LSO-APD Detektoren, deren Signale von der gleichen Anzahl an selbstständigen elektronischen Kanälen prozessiert werden und Information über Zeit und Energie jedes Ereignisses liefern. Diese Art der Auslese minimiert Totzeiteffekte und bietet die Möglichkeit, Ereignisse zu identifizieren, die durch Compton-streuung zwischen Detektorelementen erzeugt werden. Der Scanner hat eine mittlere Energieauflösung von 22%, eine Zeitauflösung von 10 ns (FWHM) und eine rekonstruierte Ortsauflösung von 1.3 mm. Experimentelle Ergebnisse zeigen einen guten Kompromiss zwischen Ortsauflösung auf der einen und Empfindlichkeit auf der anderen Seite. Eine erste Evaluierung der Bildgebungseigenschaften des Tomographen wurde durch eine Herz-Aufnahme einer Maus realisiert.

Die klinisch etablierte PET/CT kombiniert zwei unterschiedliche Bildgebungsmodalitäten und liefert dadurch sowohl funktionelle als auch anatomische Informationen. PET/MR stellt ein alternatives multimodales Bildgebungsverfahren dar, welches einen höheren Weichteil-Kontrast erzielt und gleichzeitig die Patientendosis minimiert. PET/MR benötigt allerdings ein technisch anspruchvolleres Detektordesign, welches Interferenzen der beiden Modalitäten ausschließt. Die Realisierbarkeit der Verwendung von Silizium-Photomultipliern (SiPM), welche einen neuen, vielversprechenden Photodetektor-Typ darstellen, in PET/MR wurde untersucht. Die Vorzüge dieser Detektoren sind unter anderem ihre hohe Verstärkung, ihr schnelles Ansprechverhalten und ihre Unempflindlichkeit gegenüber magnetischen Feldern. Experimentelle Untersuchungen von Einkanal-SiPMs in Kombination mit Szintillationskristallen zeigen eine zu LSO-APD-Detektoren vergleichbare Energie- und eine bessere Zeitauflösung. Durch die genannten Vorzüge der SiPMs kann sogar auf eine komplizierte elektronische Signalbearbeitung verzichtet werden. Beim Betrieb in Gegenwart magnetischer Felder wurde keine Beeinflussung der Leistung von SiPMs beobachtet. Ein Detektor Konzept, welches auf individueller Kopplung von 1 × 1 mm^2 Szintillationskristallen an 1 × 1 mm^2 SiPMs basiert, wird als geeigneter Ansatz für PET im Submillimeter Bereich erachtet.

List of Abbreviations

ADC	Analog to Digital Converter
APD	Avalanche PhotoDiode
ASIC	Application Specific Integrated Circuit
CCI	Clock Control Interface
CFD	Constant Fraction Discriminator
CSP	Charge Sensitive Preamplifier
CT	Computed Tomography
DAC	Digital to Analog Converter
DAQ	Data Acquisition
DOI	Depth Of Interaction
EMI	ElectroMagnetic Interference
ENC	Equivalent Noise Charge
^{18}F-FDG	^{18}F-FluoroDeoxyGlucose
FIFO	First In First Out
FOV	Field Of View
FPGA	Field Programmable Gate Array
FT	Fourier Transform
FWHM	Full Width at Half Maximum
HPGND	High-Pass Ground
LOR	Line Of Response
LSO	Lutetium Oxyorthosilicate
LYSO	Lutetium Yttium Oxyorthosilicate
MADPET-II	Munich Avalanche Diode PET-II
MCA	Multi-Channel Analyzer
MLEM	Maximum Likelihood Expectation Maximization
MRI	Magnetic Resonance Imaging
MWPC	Multi-Wire Proportional Chamber

NIM	Nuclear Instrumentation Module
OSEM	Ordered Subsets Expectation Maximization
PDE	Photon Detection Efficiency
PET	Positron Emission Tomography
PMT	PhotoMultiplier Tube
PSF	Point Spread Function
PVE	Partial Volume Effect
QE	Quantum Efficiency
RF	Radio Frequency
ROI	Region Of Interest
RSDP	Receiver Shaper Discriminator Peak detector
SiPM	Silicon PhotoMultiplier
SNR	Signal to Noise Ratio
SPECT	Single Photon Emission Tomography
TDC	Time to Digital Converter
TOF	Time Of Flight
TOR	Tube Of Response
US	Ultra Sound

List of Figures

Positron Emission Tomography: physics and instrumentation

The Munich Avalanche Diode PET-II (MADPET-II) project

Results: Front-end and system performance evaluation

Characterization of LYSO-SiPM detector modules and comparison with an LSO-APD detector

Discussion of Part II

List of Tables

Positron Emission Tomography: physics and instrumentation

The Munich Avalanche Diode PET-II (MADPET-II) project

Results: Front-end and system performance evaluation

Characterization of LYSO-SiPM detector modules and comparison with an LSO-APD detector

Contents

I Development and Performance Studies of a Small Animal Positron Emission Tomograph with Individual Crystal Readout and Depth of Interaction Information 21

Chapter 1

Introduction

Nowadays, there is a variety of medical imaging modalities being used in clinical routine in order to diagnose and monitor non-invasively human diseases. Modalities such as planar or Computed Tomography (CT) x-ray imaging, Ultrasound (US) and Magnetic Resonance Imaging (MRI) are able to provide high resolution anatomic information on the level of organs and eventually (in the case of MRI) on the tissue level. However, their reduced sensitivity, which is limited to molar and millimolar concentration ranges, does not allow for imaging of biological processes. On the other hand, the increased sensitivity of nuclear medicine imaging techniques, namely Single Photon Emission Tomography (SPECT) and Positron Emission Tomography (PET), on the nano-/pico-molar range allows for imaging on the the level of cells, proteins, as well as DNA, as described in Figure 1.1. Thus, a large number of biological processes, and the various diseases related to them, can be monitored with high accuracy.

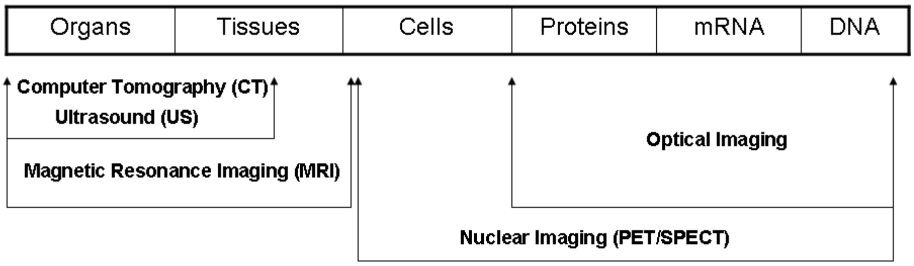

Figure 1.1: Block diagram indicating the sensitivity limits of each imaging modality used in modern medicine.

1.1 Imaging in nuclear medicine

Image formation in nuclear medicine is achieved through the administration of a radiopharmaceutical into the patient's body and the detection of gamma radiation emitted from it. Depending on the disease or the lesion that is to be monitored, the radiopharmaceutical, alternatively called radiotracer, is made of biomolecules, typically metabolized by the part of the human body in question (e.g a malignant tumor, the heart or the brain).

The distribution of the radiotracer within the human body is such that the highest concentration is observed in the biological structures of interest. These biomolecules are labelled with a radioactive substance, hence the localization of a lesion is achieved through the measurement of the radiotracer spatial distribution within the human body by means of radiation detection.

In order to reproduce as accurately as possible the radiotracer distribution, it is highly desirable in nuclear medicine that the radiation emitted by the patient suffers as few alterations as possible within the patient's body and that it is fully absorbed by the imaging device that surrounds the patient. The essential element of the imaging device is typically a combination of a scintillation crystal, which converts the incident gamma radiation to visible light, and a photodetector, which collects the scintillation light and converts it into an electrical pulse.

Gamma radiation passing through matter can loose energy via numerous different processes, the most important of which are: photoelectric absorption, Compton scatter and pair production. During the first process, the gamma quantum is fully absorbed by a bound atomic electron, which in turn escapes from the atom leaving it positively ionized. The second process is the scattering of the incident photon by a loosely bound atomic electron. In this process the photon is not fully absorbed but only transfers a part of its energy to the electron, changing at the same time its direction of flight. The third process is the interaction of the incident radiation with the atomic nucleus during which the photon is fully absorbed and results in the production of an electron-positron pair. A minimum gamma energy of 1.02 MeV is necessary for this process to happen.

The nuclides used to label pharmaceuticals in nuclear medicine emit photons with energies at which the photoelectric effect and Compton scatter are dominant. These interactions take place both within the object to be imaged as well as within the scintillation crystal, affecting in different ways the performance of the imaging device. Photoelectric absorption and Compton scatter within the object to be imaged (defined as attenuation in Section 2.1.3) contribute to reduced image quality, as will be discussed in the following sections. On the other hand, photoelectric absorption should be enhanced within the scintillation crystal unlike Compton scatter in order to improve detection efficiency.

1.2 Multimodality imaging

The reconstructed images in PET and SPECT provide quantitative information about the radiotracer concentration and its temporal behaviour in a Region Of Interest (ROI). However, in order to accurately localize this ROI in the anatomical background of the patient, the PET or SPECT data are merged with the data from other imaging modalities, such as CT, and more recently MRI, which provide high-resolution anatomical information [22].

PET/CT is already well established in the clinical routine and typically involves a very fast CT acquisition of a few seconds, followed by a PET acquisition of several minutes. The acquired images are then appropriately coregistered. PET/MR may be implemented in a similar way to PET/CT, however, since an MR acquisition is not as fast as the CT acquisition, the overall time of a patient scan may increase significantly. Another approach, currently implemented in preclinical imaging, involves the implementation of a PET insert inside the bore Field Of View (FOV) of the MR tomograph [74, 39, 21]. This approach allows for simultaneous PET/MR acquisition, however the FOV of the PET insert is reduced. A more troublesome approach would be to integrate the PET hardware within the hardware of the MR tomograph.

The presence of stationary and alternate magnetic fields during an MR acquisition should be taken into account when designing a PET system for simultaneous PET/MR. The PET photodetectors should be insensitive to magnetic fields and, in addition, the subsequent processing electronics should be properly shielded. On the other hand, the MR signal may be distorted by magnetic components possibly existent in the PET hardware.

1.3 Clinical versus small animal imaging

In clinical routine, PET and SPECT images are mostly used in oncology, cardiology and neurology in order to diagnose a malignant lesion or to diagnose and monitor the evolution of various diseases non-invasively.

Small animal (preclinical) imaging, however, is a very powerful tool in pharmacology for the development and evaluation of new radiotracers. In addition, due to the similar physiology and genetic material of mice and rats to humans, small animals are widely used in biology in order to model human diseases. Since PET and SPECT are non-invasive imaging techniques that allow for in vivo monitoring of the radiopharmaceutical distribution, their use leads to a significant decrease in the number of animals sacrificed and consequently in the cost of these studies. A small animal imager may also be thought of as a tool for investigating novel detector hardware.

However, small animal imaging introduces a number of challenges that need to be confronted in order to achieve the goal of high resolution, quantitative imaging [99]:

- Since in preclinical imaging the object to be imaged is many orders of magnitude smaller compared to humans in clinical imaging, the requirements in spatial resolution become correspondingly higher. The typical spatial resolution of 4-6 mm achieved with clinical PET scanners needs to be reduced to the millimeter or even submillimiter range in order to be able to resolve the significantly smaller structures within the body of a rat or a mouse.

- The requirement for high spatial resolution leads to the necessity for high sensitivity, namely high detection efficiency for a given amount of injected radiotracer. Increased sensitivity will result in increased Signal-to-Noise Ratio (SNR) in the reconstructed image and thus improve the image quality. A straightforward, but nevertheless naive approach to the problem would be to increase the amount of the injected radiotracer. An obvious limitation to this approach is the small weight of the mouse or rat which restricts the amount of received dose to specific levels. In addition, given the smaller FOV of the small animal imager, dead time and pile up effects in the tomograph's hardware as well as increased number of random coincidences are likely to disturb the acquisition and degrade the image quality.

- Anesthesia of the animal is almost a necessity for artifact free PET images since it will prevent unnecessary movement during the acquisition. However, especially in the case of brain imaging, anesthesia may disturb the biological processes under study and thus is to be avoided. A small animal PET scanner aimed for conscious rat brain imaging has already been built and demonstrates promising results towards this direction [109]

1.4 Overview of this work

This work is organized into two parts, where the first part (Chapters 3 through 5) is dedicated to the development and evaluation a small animal scanner for high resolution PET and the second part (Chapters 6 through 7) is dedicated to the investigation of novel detector technologies for multimodality imaging.

Chapter 2 reviews the basic physics introduced in Positron Emission Tomography. The fundamental instrumentation and the most important features of PET imaging are also presented.

Chapter 3 describes a small animal PET tomograph, developed as a part of this work at the Nuclear Medicine Department, Klinikum rechts der Isar of the Technische Universität München. Its unique hardware features are emphasized. In Chapter 4, the results from performance evaluation measurements are presented and discussed in Chapter 5.

Chapters 6 and 7 form the second part of the thesis and focus on studies of a novel detector concept for the development of a small animal PET insert for simultaneous PET/MR imaging. The promising properties of a new type of photodetector are studied and the feasibility of using this photodetector in PET is investigated.

Chapter 2

Positron Emission Tomography: physics and instrumentation

2.1 Basic principles of PET imaging: advantages and limitations

PET is considered to be the most sensitive modality for performing quantitative in vivo imaging in modern medicine. The following paragraphs summarize the special features of PET imaging and describe how these features affect the image quality.

2.1.1 Positron emitters, finite positron range and annihilation photon acollinearity

The radiopharmaceuticals used in PET are labelled with β^+ emitters. The most probable deexcitation mode of the nucleus is through positron emission, according to which a proton of the nucleus is converted to a neutron with the simultaneous emission of a positron and a neutrino.

$$p \rightarrow n + e^+ + \nu \tag{2.1}$$

The positron, depending on its initial energy, will travel a specific distance in the surrounding material, loosing energy until it annihilates with an electron resulting in the emission of two photons. Table 2.1 lists the radioisotopes commonly used in PET, as well as their mean and maximum emitted positron energy.

Radionuclide	Mean e^+ energy (keV)	Maximum e^+ energy (keV)	Halflife
^{18}F	250	635	110 min
^{11}C	390	970	20.3 min
^{13}N	490	1190	10.0 min
^{15}O	740	1720	2.07 min

Table 2.1: The most commonly used positron emitters in PET and their characteristics.

Prior to annihilation the positron and the electron form a bound system called positronium, which may exist either in an antisymmetric singlet spin state of total spin $S = 0$ ("parapositronium") or in a symmetric triplet spin state of total spin $S = 1$ ("orthopositronium"). The parapositronium has a mean lifetime of 125 ps and annihilates to two photons, while the orthopositronium has a longer lifetime of 140 ns and annihilates to three photons, making thus the ratio of three-photon to two-photon annihilation cross sections equal to approximately $\frac{1}{370}$ [70, 6]. Currently PET techniques take into account only the fastest and most probable two-photon annihilation, however three-photon annihilation has recently attracted the interest in PET as a possible oxygen sensitive tracer due to the quenching of this annihilation type in oxygen rich environments [27, 24, 36]. Recent studies have demonstrated the feasibility of three-photon imaging as a simultaneous modality to the established two-photon PET imaging, however it is essential to overcome limitations on the sensitivity and energy resolution of current PET detectors in order to achieve sufficient spatial resolution [40].

The emitted positrons travel a specific distance within the object until they energetically reach their rest mass (511 keV) and annihilate with an electron. As a result, there is a distance between the point of positron emission, which also indicates the location of the radiotracer distribution, and the point of gamma ray emission, which will eventually be detected from the imaging device. The positron range depends mainly on the surrounding material and the maximum energy of the emitted positrons. For example, it reaches approximately 0.1 mm in water for positrons emitted by ^{18}F (635 keV maximum energy) [51].

In addition, assuming that both the electron and positron are at rest during annihilation, the momentum conservation law imposes that the two resulting gamma rays would be emitted back-to-back, namely at a π angle with respect to each other. However it may also be the case that the positron has some residual kinetic energy during annihilation which, in turn, will result in two emitted photons at an angle different than π. The distribution of this angular difference has a Full Width of Half Maximum (FWHM) of approximately 0.5°. Both phenomena of finite positron range and photon acollinearity are illustrated in Figure 2.1. Depending on the architecture of the PET scanner, it is possible

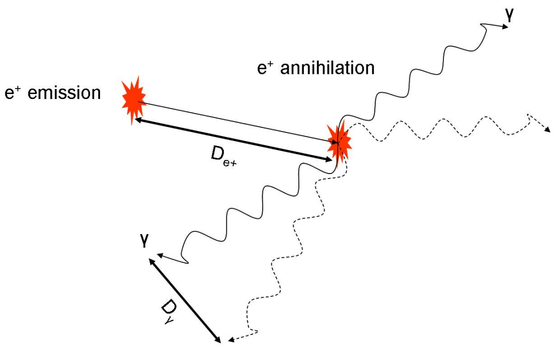

Figure 2.1: Illustration of the contribution of the finite positron range (D_{e+}) and the annihilation photon acollinearity (D_γ) to the accuracy of position information extracted in PET. The two effects are exaggerated in the figure.

due to acollinearity that the pair of photons would be detected by a different pair of detectors, hence introducing blurring in the reconstructed image. Photon non-collinearity becomes more significant in clinical imaging where the scanner diameter is relatively large. The dependence of blurring due to photon non-collinearity on scanner diameter D is given by the following equation:

$$D_{\gamma} = 0.0022 \cdot D \tag{2.2}$$

2.1.2 Coincidence detection: trues and accidentals

A true coincidence event is defined as the simultaneous detection, from two opposing detectors operating in coincidence, of two photons resulting from the same annihilation. In reality, due to the detectors' finite timing resolution, the coincidence events are not detected simultaneously, but within a time window which is typically chosen to be twice as wide as the detectors' timing resolution (approximately equal to 3σ of the time difference histogram for a detector pair in coincidence). It is also possible however that within the same window a number of coincidence events is detected, which however do not originate from the same annihilation, as illustrated in Figure 2.2. These accidental (or random) coincidences are added to the true events and usually result in a uniform enhanced background in the reconstructed image, thus reducing the SNR. The number of random coincidences has a linear dependence on the width of the time coincidence window and a quadratic dependence on the emitted radioactivity. Thus, the time coincidence window should be kept narrow enough in order to minimize the number of detected random coincidences, but well above the detectors' timing resolution so as not to result in underestimation of the true coincidence events.

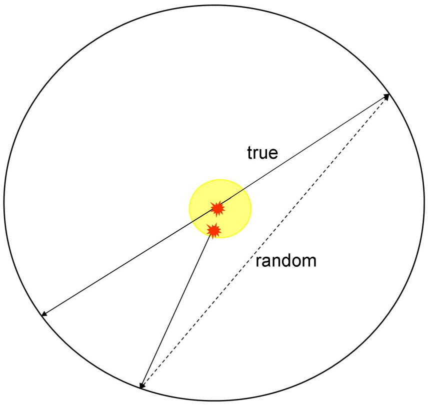

Figure 2.2: Illustration of a true and a random coincidence event as registered by a PET detector ring.

2.1.3 Attenuation and scatter

Since the radiopharmaceutical in nuclear medicine is injected into the patient's body (emission imaging), the emitted photons have a given probability of interacting within the body before being detected by the imaging device. This probability depends both on the energy of the emitted photons and on the composition of the material through which the photons are travelling. For the photon energies involved in PET, the most probable interaction is Compton scatter, however at energies below 100 keV photoelectric absorption is also a considerable effect.

Compton scatter may occur once or multiple times within the object. As a result, one or both annihilation photons may be deflected from their initial trajectory and they will either be still detected by a different detector pair than the expected, or they may escape the FOV of the tomograph. Photoelectric absorption within the object will result in the full absorption of one or both annihilation photons in the patient's body and therefore they will never be detected by the imaging device.

Attenuation correction applies in cases where the emitted photons are not detected by the imaging device, while scatter correction applies in cases where the photon, after being scattered, is detected by the imaging device thus giving wrong information about the initial emission point within the patient's body. The presence of scatter and attenuation in the reconstructed image leads to reduced image contrast and distortions, since a smaller number of "useful" events will be detected due to attenuation and false information about the emission point will be extracted due to scatter, as illustrated in Figure 2.3.

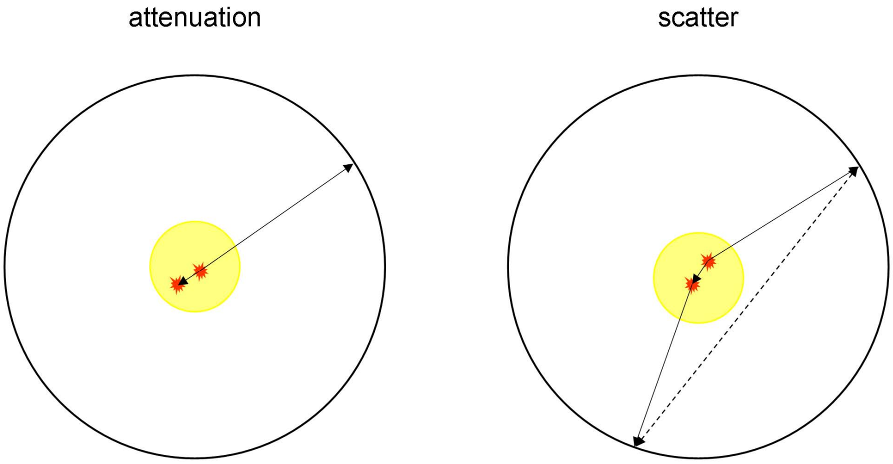

Figure 2.3: Illustration of attenuation and object scatter present in a PET acquisition.

PET imaging has the advantage that the attenuation effect does not depend on the position of the object to be imaged along a specific Line Of Response (a virtual line connecting the centers of two detectors in coincidence, LOR) but only on the length of the intersection of the object to be imaged with the LOR [23]. One method to correct for attenuation is to calculate a patient specific attenuation coefficient map which is then applied to the measured data. This is achieved by either using the measured data from a CT device, or by acquiring a set of a blank scan with an external source and with no object in the FOV and a transmission scan.

In the case of object scatter, the assigned LOR to such scatter events does not intersect with the annihilation point, thus resulting in event mispositioning in the reconstructed image (dashed LOR in Figure 2.3). In order to avoid the effects of object scatter, a PET acquisition is usually performed at a relatively narrow energy window around the photopeak of the acquired energy spectra. However, the efficiency of such a process is hindered by the poor energy resolution of typical PET detectors.

2.1.4 Spatial resolution

Spatial resolution in PET is defined as the FWHM of the reconstructed one dimensional profile of a point source in the center of the FOV, otherwise known as Point Spread Function (PSF). The spatial resolution is affected by a number of factors among which is the finite positron range and the annihilation photon non-collinearity mentioned in Section 2.1.1. An approximation of a PET scanner's spatial resolution may be given by the following equation:

$$FWHM = \sqrt{FWHM_{int}^2 + D_{e_+}^2 + D_{\gamma}^2} \tag{2.3}$$

where FWHM$_{int}$ is the intrinsic resolution of the detectors defined in Figure 2.4.

An additional blurring factor for the reconstructed image is the so-called parallax error, namely the dependence of spatial resolution on the radial distance of the object to be imaged with respect to the center of the FOV. As depicted in Figure 2.5, the larger the distance from the center of the FOV, the more significant the uncertainty in the determination of the LOR. Due to the finite dimensions of the PET detectors and since there is no information about the interaction point of incident radiation along the crystal length (Depth of Interaction (DOI) information), this uncertainty is represented by the broadening of the Tube Of Response (TOR), which, as opposed to the LOR definition given above, is a virtual tube connecting the volumes of two detectors in coincidence. The net effect on the reconstructed PET image would thus be larger (worse) spatial resolution. In order to compensate for the parallax error, one can decrease the scintillator thickness. However this will lead to reduced sensitivity of the imaging device as will be addressed in Section 2.1.5. Thus, there should be a compromise between sensitivity and spatial resolution when designing an imaging device for PET. In small animal PET, where the parallax error is more evident, a number of special detector architectures (Section 2.2.5) are used in order to better extract and make use of DOI information.

2.1.5 Sensitivity

High sensitivity, therefore high photon detection efficiency, is a requirement in PET imaging since it results in high SNR and hence to higher contrast in the reconstructed image. Sensitivity is strongly dependent on the material and the thickness of the scintillation crystal as well as on the material and the geometry of the septa, in the case of 2D imaging (Section 2.2.4). Long crystals of high Z material will increase the scintillator's stopping power and consequently the number of detected events. However, as already mentioned, there is a trade off between sensitivity and spatial resolution.

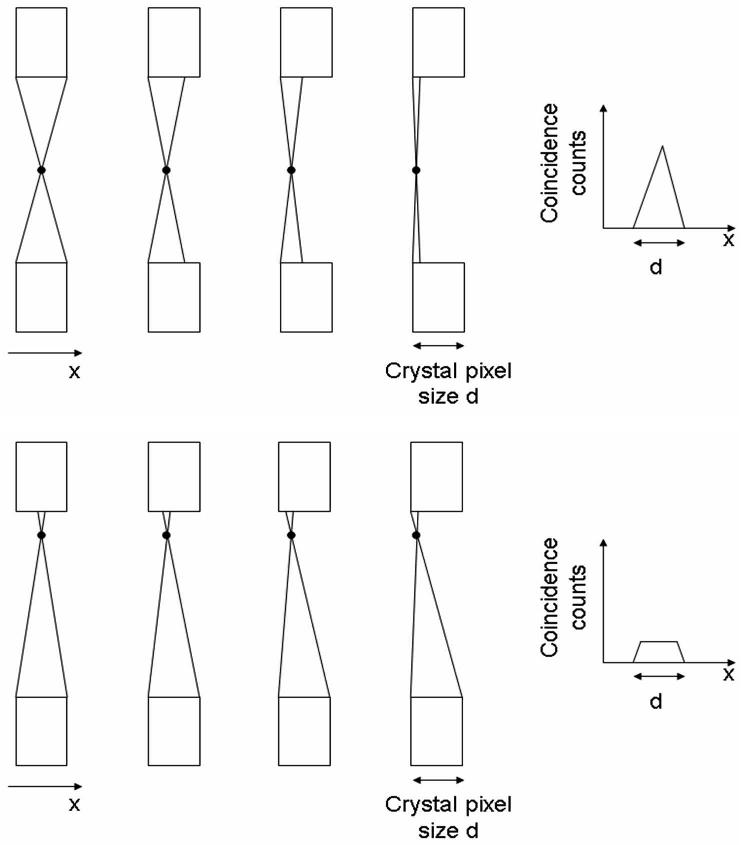

Figure 2.4: The intrinsic resolution of a detector pair is defined as the FWHM of the distribution of detected coincidences when moving a point source along the axial (x) dimension. At the midpoint between the two detectors the distribution is a triangle (top) and as approaching one of the two detectors, the distribution obtains a trapezoidal shape (bottom).

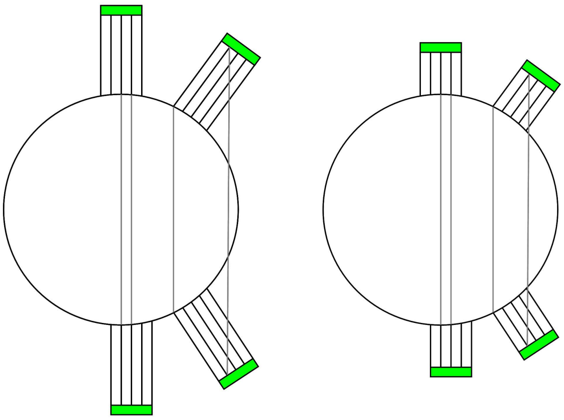

Figure 2.5: Illustration of the parallax error: The use of long crystals (left) may lead to degradation of the spatial resolution at the edges of the FOV due to the broadening of the TOR for oblique detector pairs. The use of shorter crystals (right) may eliminate this effect reducing, however, sensitivity.

It should be mentioned that variations in sensitivity (defined as number of detected coincidences) of every individual LOR are likely to be observed. These variations are attributed to a combination of the following factors:

- Variations in the intrinsic detector efficiencies and gains especially for systems which consist of discrete detector elements.
- Variations in the LOR geometry, namely oblique LORs are characterized by a smaller solid angle coverage and thus by decreased sensitivity. These variations have a strong dependence on the radial and axial position of each LOR.
- Dependence of the LOR efficiency on the photon incidence angle with respect to the detector face.
- Time misalignment between detectors may lead to inefficient coincidence detection and thus to reduced sensitivity.
- Mechanical misalignment between opposing detectors may hinder the reliability of a normalization measurement during which a specific position for the center of each detector is assumed.

Thus, an additional correction for these effects must be performed which is typically referred to as normalization. A direct method for normalization is to irradiate all LORs apparent in the FOV with a rotating rod source and to calculate the inverse number of counts detected at each LOR known as normalization factors. An indirect normalization method assumes that the detected number of counts in each LOR is the product of various components related to the previously mentioned geometric and intrinsic efficiency variations [34, 69]. The geometric components may either be calculated analytically or by means of a measurement with a rotating rod source. The intrinsic efficiency components may be calculated by means of a measurement with sources that illuminate uniformly all the LORs. Normalization is an essential correction for artifact-free and quantitative PET imaging.

2.1.6 Dead time losses and pile-up effects

In the case of large injected doses, the tomograph's hardware may be subjected to dead time losses. The dead time of a measuring system is defined as the minimum time interval between two separately detected events during which only one event may be processed. The system is either not sensitive to any other events occurring within the same interval or it considers all these events as one. Dead time depends on the system's detector and processing electronics. One effect of dead time losses is underestimation of counts in the reconstructed image. Compensation for this effect can be realized by mathematically modelling the counting system's dead time or by estimating the counting losses using an external pulse generator.

In addition, pile-up effects on the detector signals due to high count rates, namely pulse shape distortions occurring when an upcoming detector pulse is superimposed to the tail of a preceding pulse, may lead to distortions on the reconstructed image.

2.1.7 Other effects: Respiratory/cardiac motion and Partial Volume Effect

Respiratory or cardiac movement of the patient during acquisition requires correction of the acquired data in order to compensate for artifacts in the reconstructed image. Usually a number of gated acquisitions is realized for every breathing or cardiac cycle. Thus, from several such cycles, a set of reconstructed images, each corresponding to a specific time frame of the cycle is produced.

The Partial Volume Effect (PVE) is the bias introduced in the estimation of the radiotracer concentration due to the limited spatial resolution of the imaging device. It is dependent on both the size and shape of the object to be imaged and on the relative radiotracer concentration in the object with respect to the surroundings. In general the PVE is minimized if the size of the ROI is relatively large in comparison to the system's spatial resolution. In the opposite case, there might be an overestimation or underestimation of the radiotracer concentration due to contributions from or to neighbouring volumes. In order to acquire quantitative information about the radiotracer distribution in a ROI defined around the object, compensation for PVE is a prerequisite.

2.1.8 Image reconstruction algorithms

Tomographic image reconstruction is based on the measured estimation of the integral of radiotracer distribution as seen under different angles (projections). Several reconstruction algorithms have been developed in order to produce a visual representation of the radiotracer distribution inside the patient's body from the various acquired projections. These algorithms can be divided into two groups: analytical and statistical.

For each projection, the acquired data are organized as number of counts along each LOR. For the total number of projections, it is convenient to reorganize the data into a 2D matrix called a sinogram, which contains the number of counts for every LOR at each angular view, namely for every radial distance d and every angle θ as illustrated in Figure 2.6. Sinograms are then used as input to the reconstruction algorithms in order to generate the final image. Analytical reconstruction algorithms model the measurement of the radiotracer distribution in a simplified way so that an exact solution may be calculated analytically. However, these algorithms ignore a number of physical effects during acquisition such as limited sampling, Poisson statistics in photon counting and attenuation or radiotracer decay, thereby resulting in reduced image accuracy. Filtered Backprojection (FBP) is one of the most widely used analytical reconstruction algorithms. This algorithm applies to every projection a Fourier Transform (FT) and a filter eliminating the high spatial frequencies. Afterwards, the inverse Fourier transform is calculated and the algorithm distributes uniformly the detected number of counts along the LOR for every filtered projection.

On the other hand, statistical, iterative reconstruction algorithms compensate for the inaccuracies introduced in the image by including in the initial estimate of the image the above mentioned physical processes. Thus, the model becomes more complicated and an analytical solution is impossible to compute. An iterative calculation is thus needed that

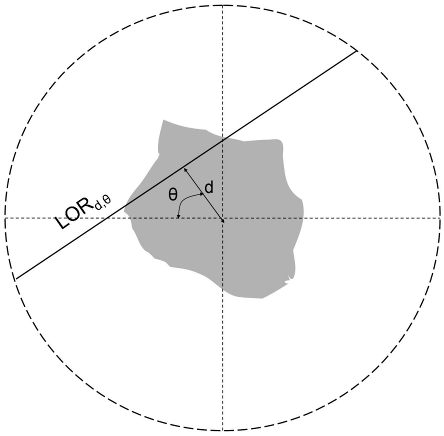

Figure 2.6: The concept of tomographic imaging: LORs characterized by different angles θ correspond to different angular views of the object to be imaged.

will converge after a specific number of repetitions (iterations) to a reliable estimation of the radiotracer distribution. Increased accuracy is achieved by iterative algorithms at the expense of time efficiency. The computation time of iterative models may be in some cases very large, hence demanding large computing power. Expectation Maximization (EM) algorithms are most commonly used, such as Maximum Likelihood Expectation Maximization (MLEM) or Ordered Subsets Expectation Maximization (OSEM). These algorithms include all the above mentioned statistical effects in order to estimate the most likely distribution of the radiopharmaceutical for each projection.

2.2 PET hardware

A typical PET detector commonly consists of a scintillation crystal read out by a photodetector. Alternative detector technologies opt for elimination of the scintillation crystal and the direct detection of incident photons by the use of semiconductor detectors or gas detectors. All these detector types will be described in the following paragraphs.

2.2.1 Scintillation detectors read by photodetectors

2.2.1.1 Scintillators used in PET

Depending on the application, a scintillator should combine a number of properties that will guarantee optimum detector performance in terms of energy and time resolution. Energy resolution is dependent on the scintillator's light yield and time resolution is dependent on both the scintillator's decay time and light yield. Typical values for energy resolution lie within the range 10 to 15% and a time resolution in the nanosecond or even subnanosecond range may be achieved by fast timing systems. Since the detection of a gamma quantum is realized by the deposition of its full energy into the detector's sensitive volume, the scintillation crystal should be made of a material of high effective atomic number and high density in order to enhance the possibility of the photoelectric effect and thus its stopping power. The light output, namely the number of produced optical photons when a specific amount of incident gamma ray energy is deposited in the scintillator, determines the scintillator's energy resolution. In addition, for fast timing applications, such as PET, a small decay constant of the scintillator light pulse is desirable.

The scintillators are divided in organic and inorganic materials with somehow complementary characteristics: Organic scintillators usually exhibit relatively low light output but are very fast, while inorganic scintillators are characterized by higher light output and a slower decay constant. The effective atomic number of organic materials is much lower compared to inorganic scintillators, making them less efficient. Table 2.2 summarizes the properties of the most commonly used scintillation crystals in nuclear medicine. Another important property shown in the table is the wavelength of maximum emission λ_{max} of the scintillator which has to match the wavelength at which the photodetector is most sensitive, in order to assure sufficient signal amplitude at the photodetector output.

	NaI(Tl)	BGO	LSO	YSO	GSO	BaF$_2$($fast$)	LaBr$_3$
Density($\frac{g}{cm^3}$)	3.67	7.13	7.4	4.53	6.71	4.89	5.29
Atomic Number (Z)	51	76	65	34	59	53	46
Decay Constant (ns)	230	300	40	70	60	0.6	26
Light Output ($\frac{photons}{keV}$)	38	8	28	46	10	2	63
Wavelength λ_{max} (nm)	410	480	420	420	440	220	380
Refractive index	1.85	2.15	1.82	1.8	1.85	1.56	1.90

Table 2.2: The most commonly used crystals in PET and their characteristics.

2.2.1.2 Photomultiplier Tubes (PMTs)

Photomultiplier Tubes (PMTs) have traditionally been used in PET in order to convert scintillation light into an electrical pulse [100, 37, 110]. The fast rise time of the order 1 ns or less and the high gain of the order 10^6 make the PMTs appropriate for fast timing applications and for gamma spectroscopy with good energy resolution. PMT performance is limited by the low Quantum Efficiency (QE), namely the ratio of the number of photoelectrons produced in the photocathode to the number of incident photons at the photocathode surface (typically 25 % at 420 nm). In addition, PMT performance is highly degraded inside magnetic fields making its use difficult for simultaneous MR/PET imaging.

2.2.1.3 Avalanche Photodiodes (APDs)

The use of semiconductor photodetectors, such as Avalanche Photodiodes (APDs), has largely evolved in the last years due to the increasing demand for multimodality imaging. The fact that APDs can be produced in various compact sizes and that their performance is insensitive to magnetic fields makes them appropriate for PET devices that can be inserted in an MR scanner for simultaneous PET/MR imaging. The main detector architecture consists of a p-to-n or n-to-p semiconductor junction operated at a reverse bias voltage, namely positive voltage on the n-side with respect to the p-side. Within the APD, a depletion region is created, inside which no free charge can exist. When radiation is absorbed in the depletion region the produced charge is swept out towards the respective electrodes. During its movement, the charge is accelerated by the electric field and moves towards the opposite polarity electrode entering an avalanche region where a number of secondary electrons is produced. The electron avalanche is collected by the corresponding electrode resulting in a current pulse. Compared to PMTs, APDs are characterized by low gain of the order 100, by higher QE (75 % at 420 nm) and by slower rise times of the order 5 ns.

2.2.1.4 Silicon photomultiplers (SiPMs)

A new photodetector is currently considered to be one of the promising future trends in detector technology for multimodality imaging in nuclear medicine. SiPMs consist of an array of individual APDs working in Geiger discharge mode (cells). In this mode, above breakdown, every illuminated cell results in a fast (rise time 1 ns), well defined single-photoelectron pulse of very high gain of the order 10^6. The individual cells are connected to each other through polisilicon resistors and the resulting current pulse is proportional to the number of illuminated cells. The fast timing and the high gain of SiPMs are accompanied by their response to a small dynamic range of detected radiation wavelengths, due to the limited number of cells in an array, by the low Photon Detection Efficiency (PDE) and by the high dark count rate. Currently, a large number of performance studies and improvements on the SiPM design are well underway [113, 88, 86, 78, 29, 28, 25, 18, 14]. Due to the well defined SiPM output signal, the use of complicated subsequent electronics, such as charge-sensitive preamplifiers, may be eliminated. This, in combination with their insensitivity to magnetic fields, may result in a potential simplified detector design for PET inserts in MR scanners, as will be shown in Chapter 6. Table 2.3 compares the characteristics of PMTs, APDs and SiPMs.

	PMT	APD	SiPM
Gain	10^6	50-1000	10^6
Rise time (ns)	1	5	1
QE @ 420 nm(%)	25	80	15-75
Bias voltage (V)	1000	300-1000	30-100
Insensitivity to Magnetic Fields	sensitive	insensitive	insensitive

Table 2.3: Operation characteristics of PMTs, APDs and SiPMs.

2.2.2 Multi-Wire Proportional Chambers (MWPCs)

Radiation detection by means of a scintillator read out by a photodetector usually results in poor energy resolution. The detection efficiency is inevitably hindered by the intermediate steps following radiation detection, namely the conversion of the gamma radiation to light and the conversion of light to electric charge. The small amount of produced charge is subjected to statistical fluctuations. The elimination of the scintillation detector has been introduced in PET hardware design by the use of Multi Wire Proportional Chambers. However, the efficiency of gas detectors is also limited given the significant lower densities of gases compared to scintillators or solid state detectors. The HIgh Density Avalanche Chamber (HIDAC) small animal PET scanner has achieved a submillimeter spatial resolution with the use of MWPCs [38] and an appropriate lead converter of the incident radiation to charge.

2.2.3 Semiconductor detectors

On the other hand, the small bandgaps of semiconductor materials, and especially of Germanium (Ge), enhances significantly the detection efficiency of these detectors, resulting in excellent energy resolution. Several groups are investigating the use of Cadmium Zinc Telluride (CZT) detectors in PET imaging [94, 89, 63]. A possible disadvantage of semiconductor detectors is their susceptibility to radiation damage effects.

2.2.4 Electronic and mechanical collimation in PET

As described above, PET imaging is based on the simultaneous detection of two photons, resulting from a positron annihilation, by two opposing detectors operating in coincidence. Since every pair of opposing detectors can be thought to define a LOR along which the emission point of the two annihilation photons should be localized, an electronic collimation is imposed on the photon detection in PET, as shown in Figure 2.2. Additional mechanical collimation made of a high Z material (septa) is sometimes applied to reduce the detection of scattered radiation or radiation from parts of the object outside the tomograph's FOV. Septa may be inserted between the individual crystals extending along the axial FOV of the scanner to allow only for recording of direct or cross coincidences (2D acquisition), as illustrated in Figure 2.7. In this way elimination of scattered events that may result in image distortions (Section 2.1.3) is achieved. The removal of the septa is also possible (3D acquisition), allowing for coincidences detected by every possible LOR, even with large axial opening angle. Compared to 2D acquisition, the recorded scatter fraction is significantly higher, but the sensitivity is also much higher, resulting in a higher SNR in the reconstructed image. New detector developments, mainly fast and luminous scintillators, together with reconstruction and scatter correction algorithms have improved 3D PET performance significantly, such that today most PET scanners are 3D-only.

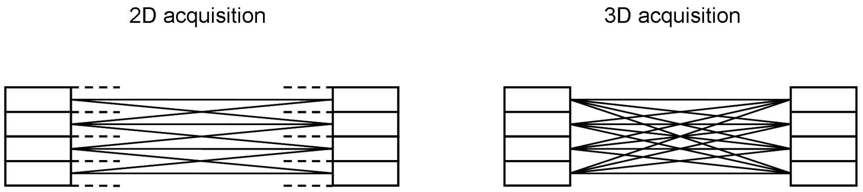

Figure 2.7: Comparison between 2D and 3D PET acquisition. In the case of a 2D acquisition inserted septa (shown as dashed lines in the figure) allow coincidences only between direct or cross planes. In the case of a 3D acquisition the septa are retracted and coincidences among all planes are allowed.

2.2.5 PET imaging devices

Block detectors are traditionally used in PET, which consist of a number of individual crystal elements read out by a small number of photomultiplier tubes (typically four). The four signals from the PMTs are used to determine the energy information, while the crystal where the interaction took place is also determined by the four PMT signals using light sharing algorithms. APDs have also recently been used in a block detector design for PET/MR imaging [76]. In addition, gamma cameras based on a continuous crystal read out by a number of PMTs have also been implemented in PET scanner designs.

A simplified PET scanner design consists of two block detectors placed opposite from each other, measuring in coincidence data acquisition mode. Tomographic acquisition requires rotation of the two detector heads around the object to be imaged. The rotation steps can be minimized by increasing the number of detectors. No rotation is required for scanner geometries with detectors covering the full 2π angle. Different PET scanner geometries are shown in Figure 2.8.

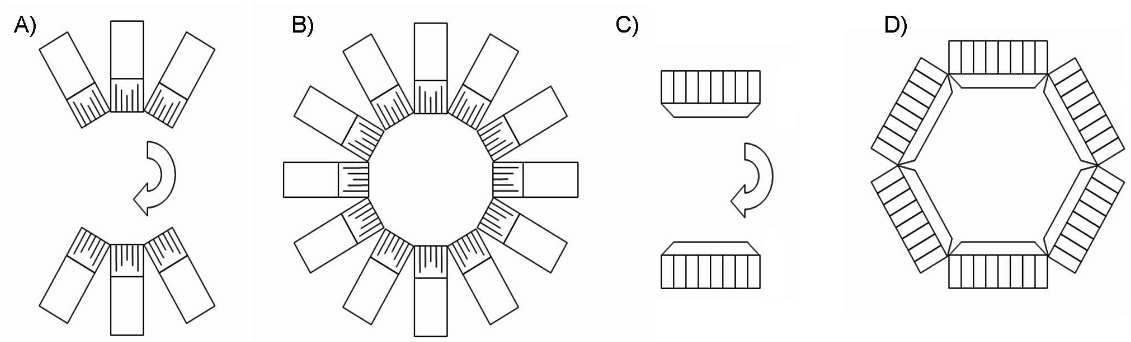

Figure 2.8: Different PET scanner configurations: A) a rotating partial ring of block detectors, B) a complete ring of block detectors, C) two opposed rotating gamma cameras in coincidence and D) a complete ring of gamma cameras in coincidence.

Alternative to the block detector concept is the individual crystal readout which can be achieved by using more compact photodetectors, such as APDs. This is a straightforward method for identifying the crystal of interaction compared to the light sharing technique employed in block detectors. However the need of a large number of electronic channels to individually process the large number of detector signals increases significantly the cost of such a design.

Some PET scanners are able to perform Time Of Flight (TOF) acquisition, by measuring the time difference in the detection of two coincident events. In this way, the positron annihilation is more accurately localized along the LOR. Nevertheless, the hardware requirements for such systems are more stringent in terms of time resolution, therefore very fast scintillation crystals, photodetectors and processing electronics are necessary.

As already mentioned in Section 2.1.5, the thickness of the crystal is critical in PET imaging. A thick (long) crystal increases the gamma detection efficiency, hence the sensitivity of the imaging device. However, especially in small animal PET systems, the parallax error is evident as the crystal thickness increases (Section 2.1.4), therefore the use of DOI information plays an important role in the improvement of the spatial resolution at the edges of the FOV. In order to minimize the crystal penetration effects and thus to determine more accurately the position along the crystal where the photon interaction took place, various detector configurations have been used.

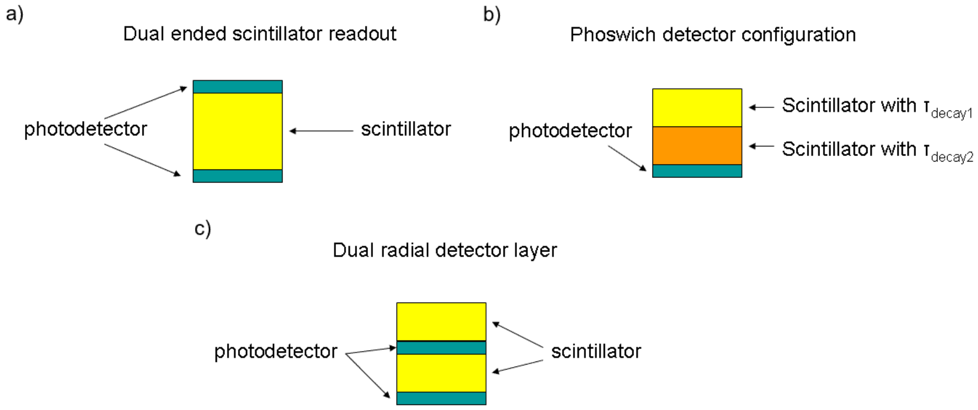

Figure 2.9: Different detector configurations used to extract DOI information: a) dual-ended crystal radout, b) phoswich detector and c) dual radial detector layer.

- The light produced by a single crystal is detected by two photodetectors placed at the two opposing ends of the crystal. Depending on the position of photon absorption along the crystal length, the two photodetectors will produce signals of different magnitude and thus the photopeak of the corresponding energy spectra will be in different positions [112, 91].

- The light produced by a dual radial crystal layer with different decay times is read by a single photodetector. Depending on whether the photon has been absorbed in the first or the second crystal, the photodetector will produce signals of different shapes [65, 97].

- The light produced by every crystal in a dual radial crystal layer is read out by its own photodetector. Thus, depending on which layer the photon has been absorbed in, the corresponding photodetector will produce a signal [84].

The various detector designs that provide DOI information are shown in Figure 2.9.

Finally, it should be mentioned that the scintillation light collection is more efficient for crystals with smaller thickness relative to crystal pixel size (denoted as d in Figure 2.4), since light loss mechanisms such as, reflection of light on the crystal sides and partial transmission, become less frequent.

Table 2.4 summarizes the performance characteristics of some state of the art, new generation small animal PET tomographs.

	Scintillator	Radial FOV (mm)	Axial FOV (mm)	Spatial resolution (mm)	Sensitivity (%)
microPET	LSO	172	18	1.8;2.0	0.56@250 keV
microPET R4	LSO	148	78	1.66;1.85	4.37@250 keV
microPET-II	LSO	160	49	0.8;1.1	2.26@250 keV
Focus	LSO	258	76	1.3;1.3	3.4@250 keV
Mosaic	GSO	210	119	2.6;3.6	1.1@410 keV
YAP-PET	YAP	100-250	400	1.8;1.8	1.7@50 keV
ATLAS	LGSO/GSO	118	20	1.8	1.8@250 keV
Sherbrooke	BGO	310	10.5	2.1;3.1	0.27@350 keV
Quad-HIDAC	none	170	280	1.1;1.1	1.1

Table 2.4: Operation characteristics of various state-of-the-art preclinical PET scanners.

Part I

Development and Performance Studies of a Small Animal Positron Emission Tomograph with Individual Crystal Readout and Depth of Interaction Information

Chapter 3

The Munich Avalanche Diode PET-II (MADPET-II) project

3.1 Objectives

The increasing demand for accurate imaging in modern nuclear medicine leads to detector architectures based on highly granulated crystals, since the size of the crystal pixel will set a lower limit on the achieved spatial resolution (Equation 2.3 of Section 2.1.4). Most commonly, large arrays of minute crystals are read out by a significantly coarser array of photodetectors in order to minimize the number of electronic channels and, subsequently, the fabrication cost (block detector design defined in Section 2.2.5). However, in such a configuration a number of physical issues are introduced which, if not taken into account, may degrade the performance of the imaging device:

- Block detectors may be subjected to pile-up effects if multiple scintillation pulses are incident to one photodetector within a small time window, resulting to either event mispositioning or count losses [30]. Since every photodetector in a block reads the scintillation light from many crystals, the above mentioned situation is very likely to occur especially when the incident gamma ray flux is high.
- Compton scatter of the incident gamma ray in one crystal may also induce a simultaneous signal in neighbouring crystals within the same block. This phenomenon, known otherwise as intercrystal scatter, introduces an ambiguity in the definition of the LOR along which the corresponding coincident event has occurred, as illustrated in Figure 3.1 [90, 108, 61].

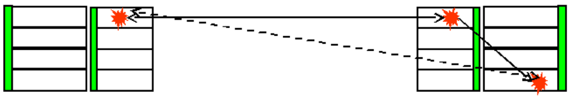

Figure 3.1: A case of intercrystal scatter: a photon which suffers Compton scatter in one crystal and is absorbed in a different crystal may result in the assignment of two different LORs for the same annihilation.

The Munich Avalanche Diode PET II (MADPET-II) is a small animal PET scanner featuring a unique detector architecture aimed to address the above mentioned effects and to investigate possible solutions.

3.2 Front-end architecture

The MADPET-II scanner consists of a ring of 18 dual layer detector modules, as shown in Figure 3.2. The axial FOV of the tomograph is 18.1 mm and the radial FOV is 71 mm, thus allowing for mouse and rat imaging. The tomograph performs fully 3D imaging, namely no septa are inserted between the different detector slices (Section 2.2.4). In total, 1152 individual detectors arranged in 8 rings (slices) of 144 detectors each are apparent on the system. The tomograph has the ability to rotate at ±10° in order to compensate for missing sampling due to the gaps between the detectors [82].

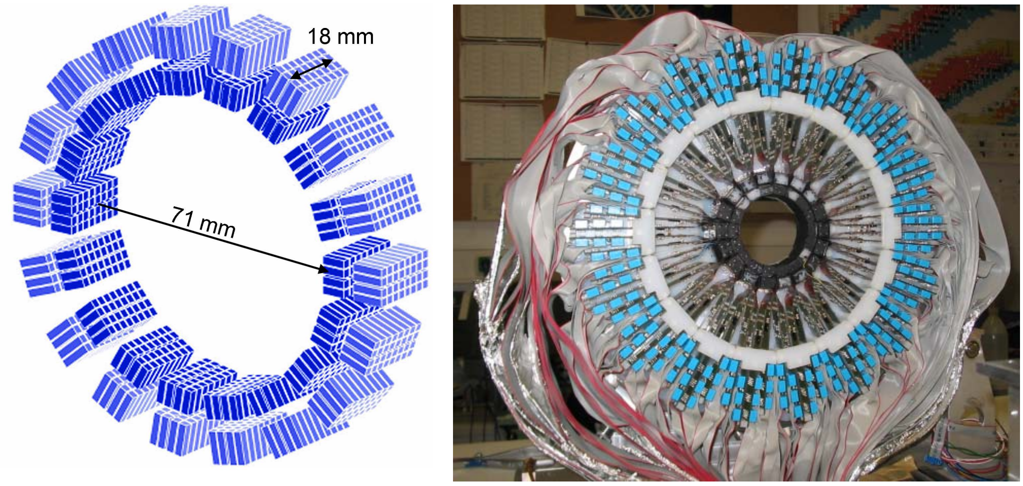

Figure 3.2: Crystal arrangement of the MADPET-II tomograph as reproduced by Monte Carlo Simulations (left) and the arrangement of the 18 dual-layer detector modules in the 1152 channel system (right).

Pre-processing of analog signals from the resulting 1152 individual channels is performed using 72, 16-channel low noise Charge Sensitive Preamplifiers (CSPs) followed by differential line drivers, both implemented in Application Specific Integrated Circuits (ASICs) using JFET/CMOS technology [75, 77]. Differential signal processing has been chosen since, compared to single-ended signal processing, it results in minimization of noise pickup. A schematic of the LSO-APD detector connection to the CSP is shown in Figure 3.3. Both the application of the APD bias and the APD readout is realized at the APD anode. Thus, the APD cathode is connected to ground and the detector is AC coupled to the preamplifier ASIC. The front end signals are transferred via approximately 5 m long differential lines to the processing electronics which are placed remotely in order to avoid interference with the detectors.

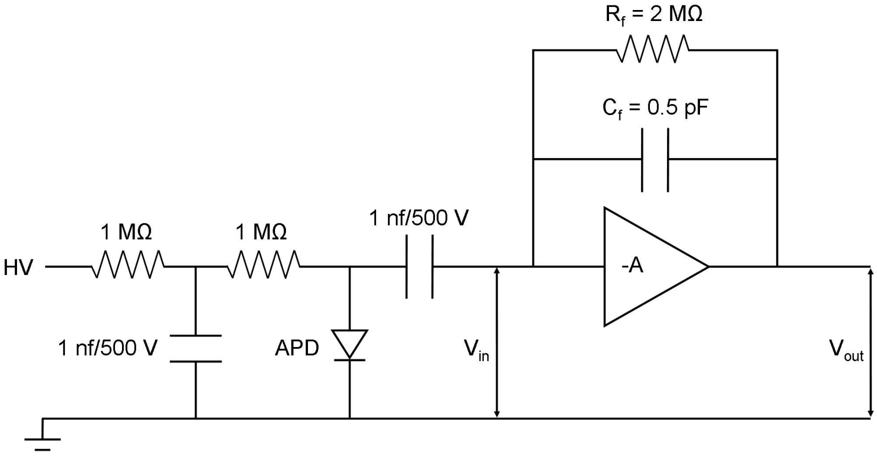

Figure 3.3: Schematic of the APD readout by means of a charge sensitive preamplifier.

3.2.1 The novel concept of individual detector coupling: LSO-APD detector arrays

Each one of the detector modules consists of a 4 × 8 Lutetium Oxyorthosilicate (LSO) crystal (CTI, Knoxville TN, USA) array optically coupled with one-to-one correspondence to a 4 × 8 APD array (S8550, Hamamatsu) [73], as shown in Figure 3.4. The crystal pixel area is 2 × 2 mm^2 resulting in a 1.6:1 mismatch between crystal and photodetector (APD pixel sensitive area: 1.6 × 1.6 mm^2). The crystal pixels are optically isolated from each other using several layers of specular reflector (3M Radiant Foil). The coupling between each individual crystal and the corresponding photodetector was achieved by means of UV cured optical adhesive (DELO Photobond, Germany) with a refractive index of 1.6.

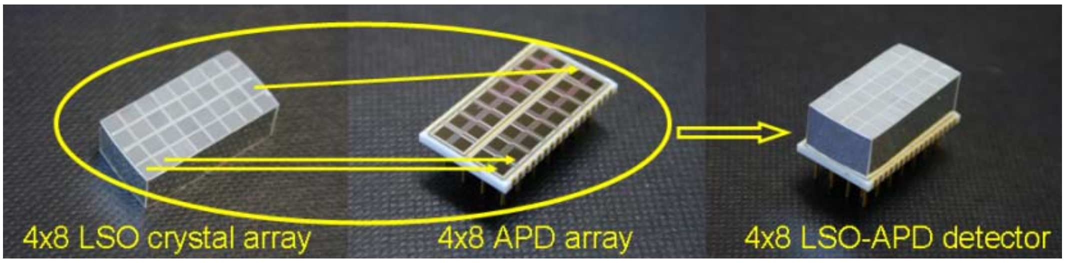

Figure 3.4: Photo of the 4 × 8 LSO array (left), the 4 × 8 APD array (center) and the complete detector array with one-to-one coupling (right).

3.2.2 Improvement of the spatial resolution: use of dual radial detector layer

In order to compensate for the parallax error addressed in Section 2.1.4, the front end detector modules consist of a dual radial layer, as illustrated in Figure 3.5. The crystal pixels used in the front layer measure 2 × 2 × 6 mm^3 and the ones used in the rear mea-

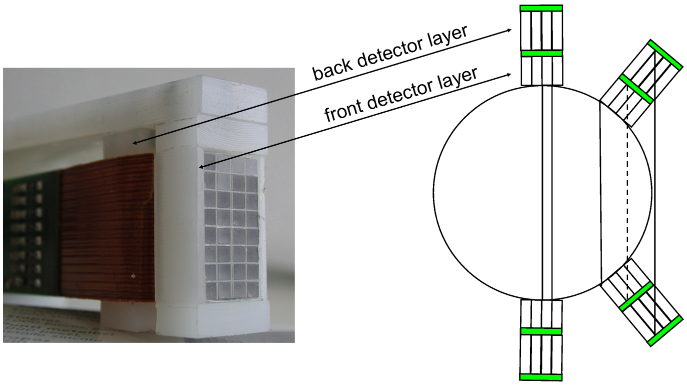

Figure 3.5: Left: photo of the 4 × 8 LSO array when mounted to the detector module. Right: extraction of DOI information using dual layer detector modules.

sure $2 \times 2 \times 8\ mm^3$. The lengths for the front and the rear crystal layers were selected empirically such that the sensitivity of a scanner consisting of only the front or only of the rear layer would be approximately the same [82]. MADPET-II is therefore able to provide "quantized" DOI information depending on whether the incident photon has been absorbed in the front or in the rear layer (detector configuration (c) in Figure 2.9).

3.3 Front-end special considerations: crystal surface treatment

In order to optimize the scintillation light collection, special care is taken regarding the surface treatment of the scintillation crystals [92, 87]. Figure 3.6 summarizes the treatment followed for the crystals of MADPET-II. Based on experimental findings, no significant

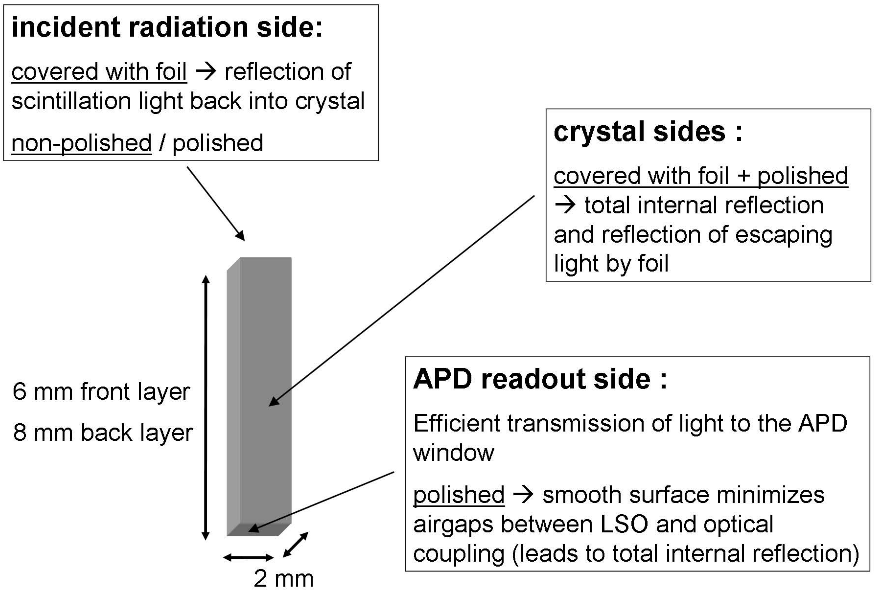

Figure 3.6: Crystal surface treatment of the LSO crystal pixels used in MADPET-II.

difference in the light output has been observed for gamma radiation incident on polished or rough crystal surfaces. This conclusion is also confirmed by simulation results shown in Figure 3.7.

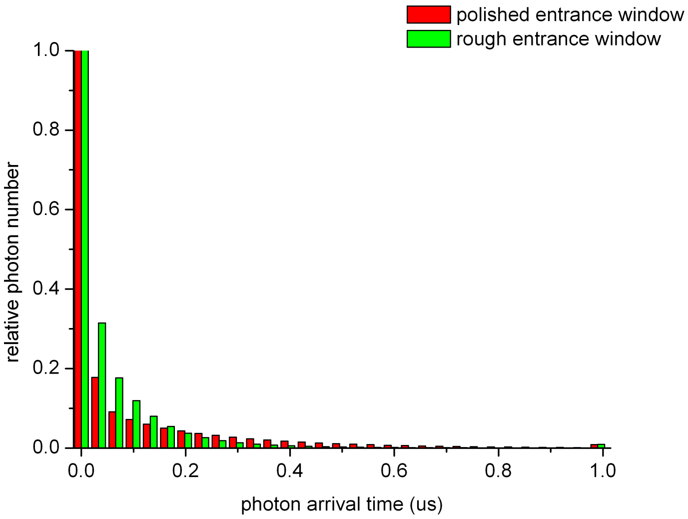

Figure 3.7: Simulated optical photon flight time histogram for polished and rough crystal entrance window. For the simulations, the DETECT2000 optical photon tracking simulation tool was used.

For the simulations, a number 2000000 initially produced optical photons is assumed and a detection time window of 1 μs has been used, which is identical to the integration window of the CSP used in MADPET-II. In Figure 3.7, the mean flight time of the detected optical photons is plotted for the two cases of crystal surface treatment. In the case of the polished surface, the probability of internal light trapping is enhanced, hence the longer histogram tail. However a reduction of only 4% in the total number of detected photons has been estimated, allowing for the use of this type of surface treatment in the system.

3.4 Integrated analog signal processing electronics

MADPET-II features individual crystal readout, therefore no use of light sharing, signal multiplexing or any type of data reduction is performed. To realize the goal of processing signals from 1152 channels independently, an ASIC containing the analog signal processing electronics has been developed. Each ASIC consists of a 4 channel differential receiver, shaping amplifier, peak detector and non-delay line constant-fraction discriminator (CFD). Thus, 288 ASICs will be required in the complete system.

The most straightforward and simple method for the extraction of time information is the leading edge technique, illustrated in Figure 3.8 (left). A specific energy threshold is set and the trigger signal is produced at the time point at which the detector pulse intersects this threshold. However, this method is inevitably subjected to timing walk effects, such that for two simultaneous signals with different pulse heights, the trigger signal will be produced at different time points.

For applications which involve a large variety of pulse heights and where accurate timing is a requirement, the constant fraction time pick-off method is usually preferred. Constant-fraction timing pick-off is performed by producing a trigger at the zero-cross level of a bipolar pulse, which is created by subtracting from the delayed version of the input pulse its attenuated version, as illustrated in Figure 3.8 (right) [42, 48, 1]. In this way, the trigger position is independent of the input pulse amplitude and, consequently, the time information is not distorted by variations in pulse height among different LSO-APD detectors. Amplitude independent time information is important for PET applications since gain variations between detectors in coincidence may lead to a degraded system-wide time resolution, a wide time coincidence window and, consequently, to an increased number of random coincidences which contribute to a reduced PET image quality [35]. Therefore, constant-fraction time pick-off is widely used in PET [9, 79].

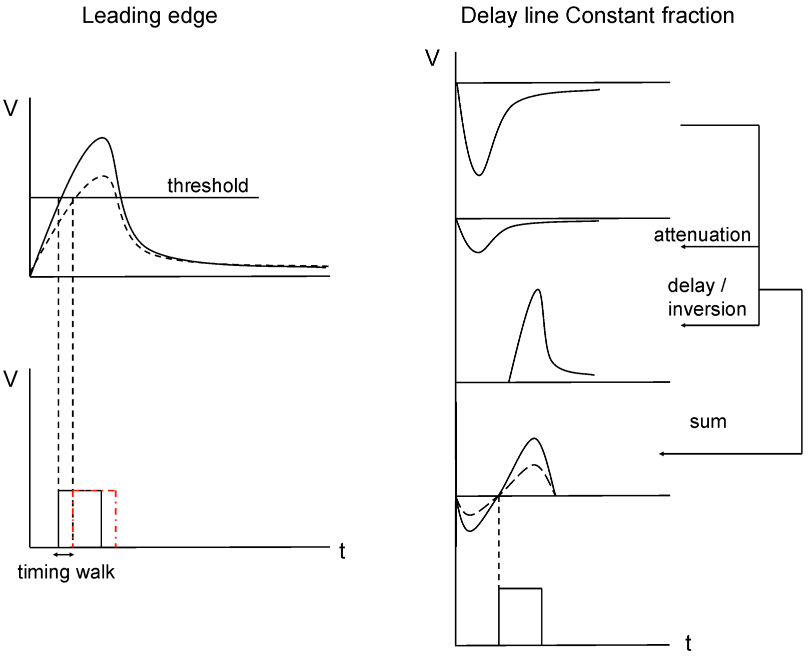

Figure 3.8: Commonly used methods for timing pick-off: leading edge timing (left) and constant fraction timing (right).

The CFD implemented in our system makes use of a one-pole high-pass CR circuit, rather than a delay line, which allows for fully monolithic integration of the timing circuit and, therefore, makes it appropriate for PET applications with many electronic channels, such as MADPET-II [8]. Non delay line CFDs with high or low-pass Gaussian filters have been previously realized and studied. Comparative measurements between non-delay and delay-line CFDs using BGO/PMT detectors, as well as Monte Carlo simulations, have shown that by proper selection of the filter time constant ($\tau = R \cdot C$) one can achieve comparable time resolution [8, 7].

Figure 3.9 illustrates the non-delay line CFD principle of operation. For simplicity, a step pulse is assumed as input in Figure 3.9. In the case of a low pass (RC) filter replacing the

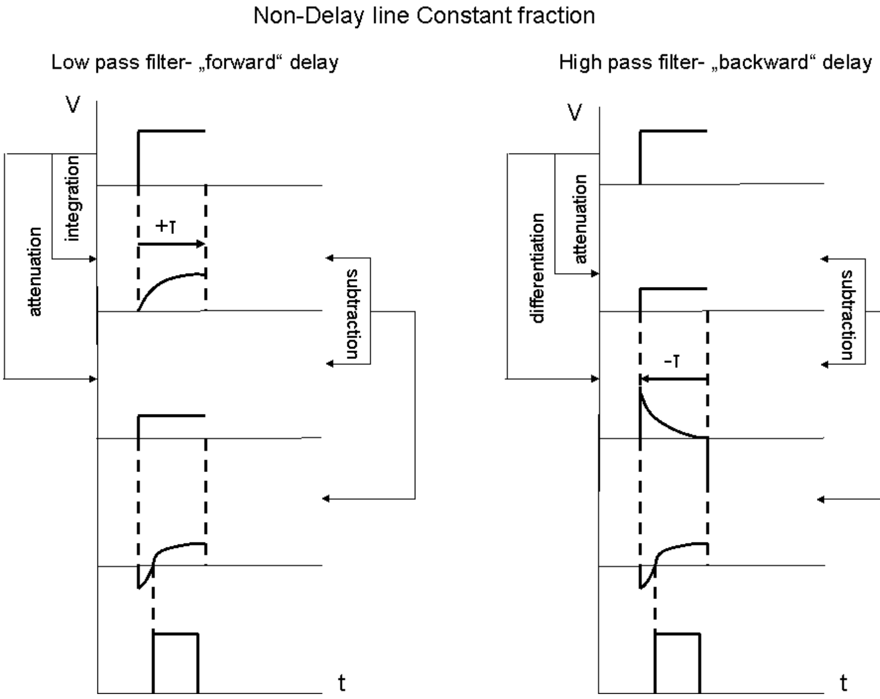

Figure 3.9: The operation principle of a CFD utilizing a low-pass (left) and a high-pass (right) filter instead of a delay line.

delay line, the input step pulse will be filtered from the high frequencies and the rising of the signal to its full amplitude will be delayed by a time approximately equal to the time constant of the filter ("forward delay" in left schematic of Figure 3.9). By proper attenuation of the input signal and subtraction from the filtered signal, a bipolar pulse is produced, whose zero cross point occurs on a constant fraction of the input pulse. In the case of a high pass (CR) filter replacing the delay line, the input pulse is filtered from the low frequencies, thus the signal preserves its fast rising edge, and at the same time the low frequency plateau is suppressed thus making the duration of the pulse smaller by approximately the time constant of the filter ("backward delay" in right schematic of Figure 3.9). In this case, the filtered signal has to be subtracted by the properly attenuated input pulse in order to obtain a bipolar signal similar to the one obtained in the low pass case.

As already mentioned, the information of interest in PET is primarily the event detection time, typically extracted by the CFD time discrimination method described above. However, energy discrimination is also required, since it allows setting an absolute energy threshold above noise level and may also set specific limits on the energy range of the detected events. This absolute energy threshold is set in addition to the relative threshold (set on a specific fraction of the input pulse height, as previously described) used for walk-free time discrimination, as shown in Figure 3.10. A logic AND operation between the outputs of an arming (leading edge) and the zero-cross discriminator in a CFD assures that a CFD trigger is only produced under the simultaneous presence of an arming trigger, thus only for those events whose pulse height is above the absolute threshold of

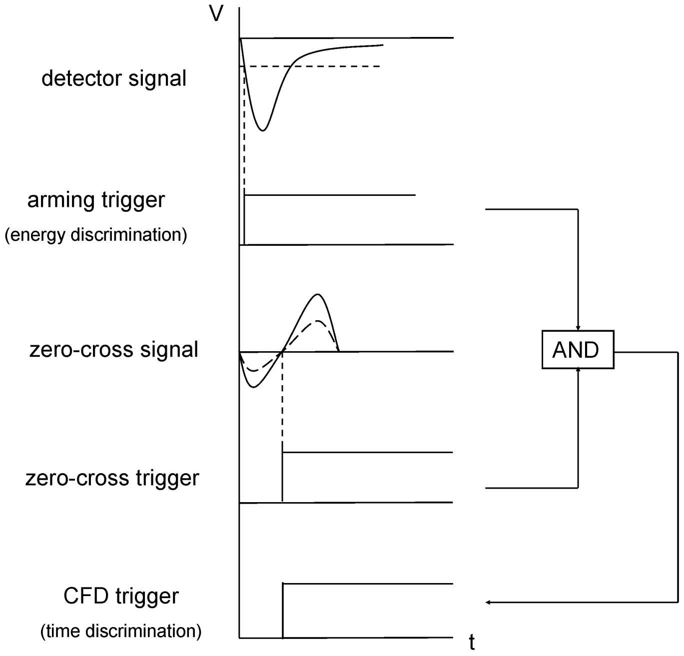

Figure 3.10: Illustration of the arming trigger logic typically implemented in a CFD.

the arming discriminator.

The ASIC developed for the time and energy discrimination in MADPET-II, is bonded in ceramic housing (JLCC44) and mounted on a PCB board measuring 8 × 4 × 0.16 cm^3 (Receiver Shaper Discriminator Peak detector, RSDP board). Also mounted upon this board are 0 Ω jumpers for adjusting the gain (gain range [0.6, 4.8]) and the shaping time (choice between 50 ns and 100 ns), 1 kΩ potentiometers for adjusting the bias currents of the shaper, the buffer amplifier, the peak detector and the trigger output, and other components which regulate the chip's performance. A picture of the RSDP board is shown in Figure 3.11 (left). Eight RSDP boards are mounted on a larger board (PET Board) which contains the digital signal processing electronics for 32 electronic channels (Figure 3.11, right).

One 4-channel ASIC is mounted on each RSDP board. The RSDP board has four differential inputs (one negative and one positive), four trigger (CFD) outputs, four peak detector outputs, which can be converted to shaper outputs via a toggle switch, four reset inputs and four Digital to Analog Converter (DAC) inputs used to set the hardware lower threshold (arming discriminator threshold). As can be seen in Figure 3.12, the differential receiver combines a negative and a positive input, which includes the gain function (selected using 0 Ω jumpers). The output of the differential receiver is fed to the shaping amplifier, which changes the signal's amplitude, rise time and decay time, as well as to the high-pass filter, used instead of a delay line. The peak detector holds the amplitude of the shaped signal. The differentiated signal is subtracted from the shaped output resulting in a bipolar input to a zero-cross discriminator. The CFD produces a 3.3 V TTL (Transistor-Transistor Logic) trigger signal as a result of a logic AND between

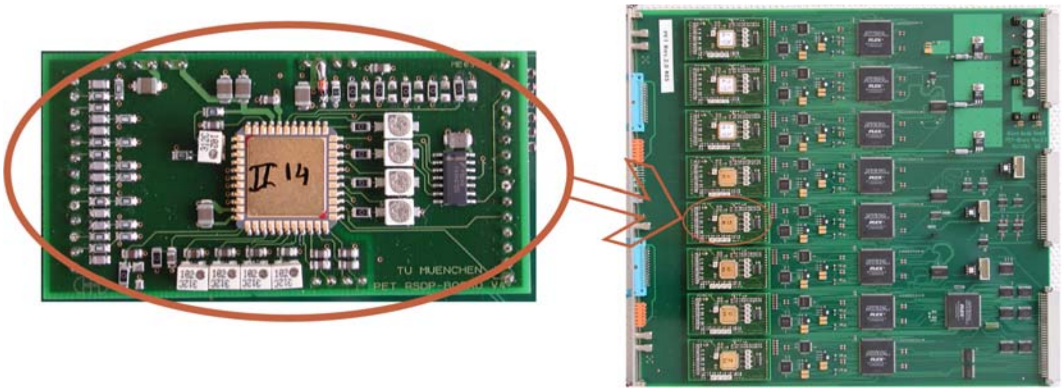

Figure 3.11: Picture of the RSDP board containing the analog signal processing electronics (left) and the PET board containing the RSDP boards and the digital signal processing electronics (right).

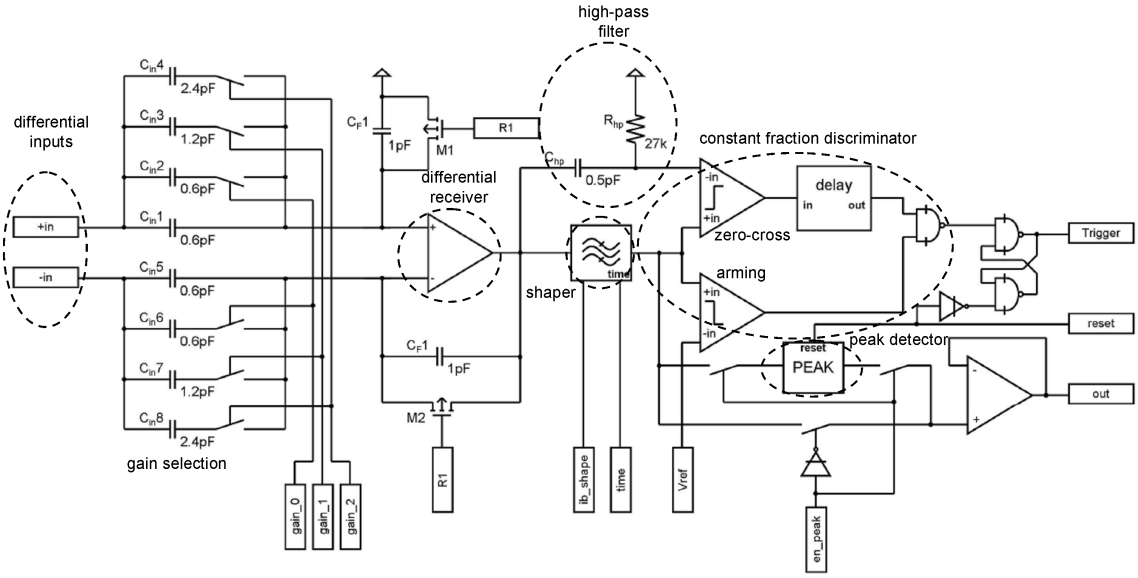

Figure 3.12: Schematic of the ASIC containing the differential receiver, the shaping amplifier, the peak detector and the constant fraction discriminator.

the output signals of an arming and a zero-cross discriminator. After digitization of the amplitude and time signals, a reset signal is sent to the RSDP board so that it is ready to process the next event. A flip-flop circuit assures that the next incoming signal will not produce a trigger until a reset signal arrives. A more detailed illustration of the shaper and the CFD circuits is shown in Figure 3.13.

3.5 Digital processing electronics

The PET board shown in Figure 3.11 contains the digital processing electronics, namely the Analog to Digital Converters (ADCs) and the Time to Digital Converters (TDCs) for the extraction of the digital pulse height and time information respectively. Each PET

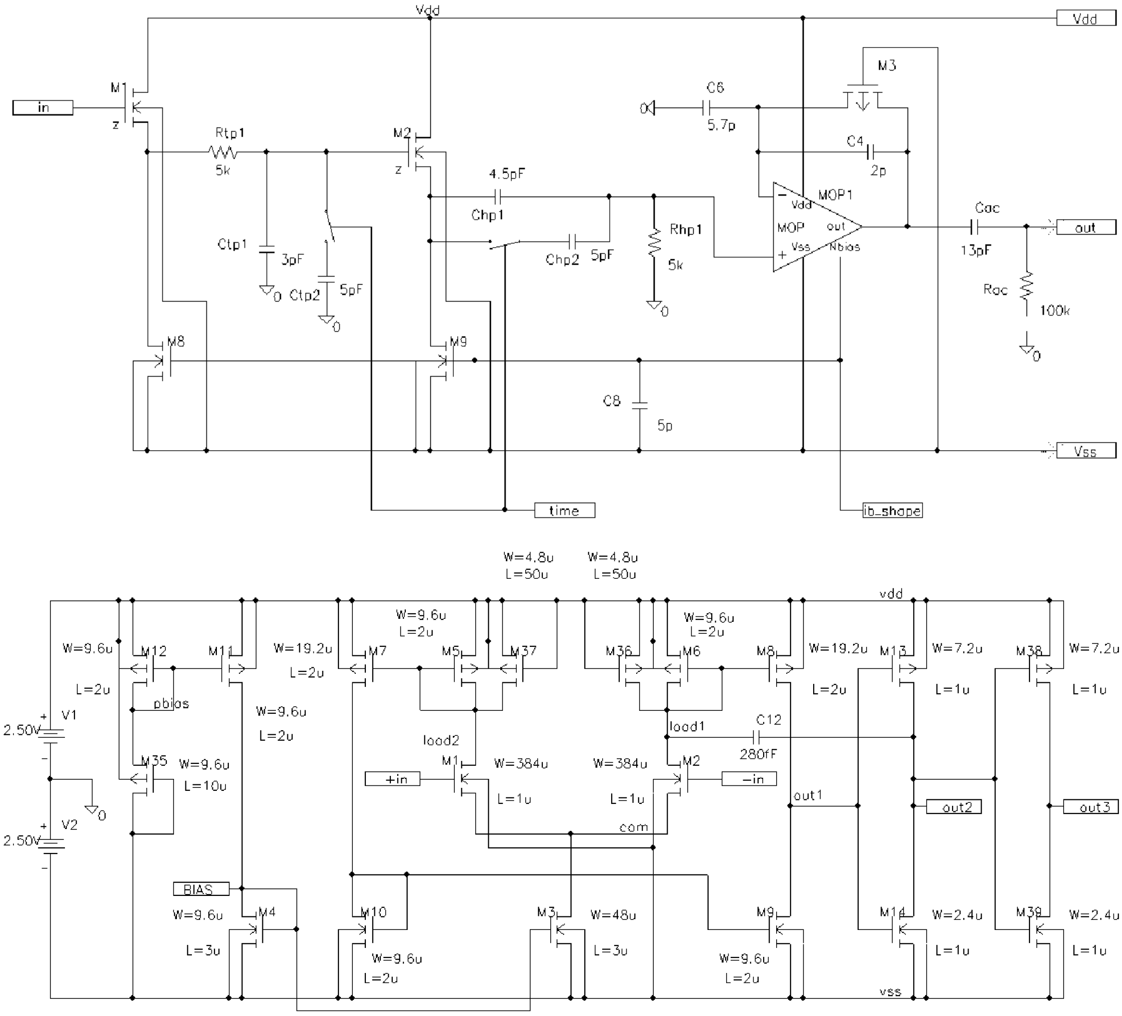

Figure 3.13: The shaper (top) and the CFD (bottom) circuits used in the analog signal processing ASIC of MADPET-II.

board contains 32 single-channel ADCs and TDCs, one for each analog electronic channel. The ADCs used (AD7470, Analog Devices) digitize the peak detector output based on the successive approximation principle [42] and have a 10-bit resolution. The TDCs used (TDC-GP1, ACAM Electronics) work in start-stop mode (15 bits, 333 ps for the LSB) and digitize the CFD output relative to an external reference clock (Global Sync). The Global Sync has a 3.2 μs period and is produced by a 40 MHz quartz clock. The generation of the Global Sync and its distribution among 18 PET boards is controlled by an additional board (Clock Control Interface, CCI) which also hosts the interface hardware with the acquisition server. As will be discussed in the following chapter, the peak detector output has been chosen to have a width of 5 μs in order to allow the shaper undershoot to return to the baseline. For that reason, the ADC initiates the digitization approximately 5 μs after the TDC, thus digitizing the maximum amplitude of the peak detector close to its falling edge. The ADC conversion process requires approximately 2 μs, after which the corresponding FPGA sends a reset signal to the analog and digital electronics in order to allow the system to process the next event. The dead time imposed by the electronics is approximately 7 μs, allowing for a maximum count rate of approximately 140000 counts/s per channel [55].

The PET board also hosts two First In First Out (FIFO) stages implemented in Field Programmable Gate Arrays (FPGAs) which facilitate the transfer of the digitized data from every individual LSO-APD detector to the hard disk of a Linux Workstation. The first stage FIFO (4 × 32 bit) is implemented in 8 FPGAs and processes the information of every electronic channel individually (1:1 FIFO). The second FIFO stage (256 × 32 bit) is implemented in a single FPGA which processes the information of all 32 electronic channels sequentially (32:1 FIFO). A third FIFO stage (32k×64 bit) is implemented on the CCI board and processes the information of 18 PET Boards (18:1 FIFO). The three FIFO stages limit the count rate performance of the system to approximately 10000 counts/s per channel.

In the complete system, 36 PET Boards process the signals of 1152 detectors. The Data Acquisition (DAQ) system is organized in two crates of 18 PET Boards and one CCI board each, as illustrated in Figure 3.14. The data are transferred from both crates via two independent Gbit Ethernet controllers.

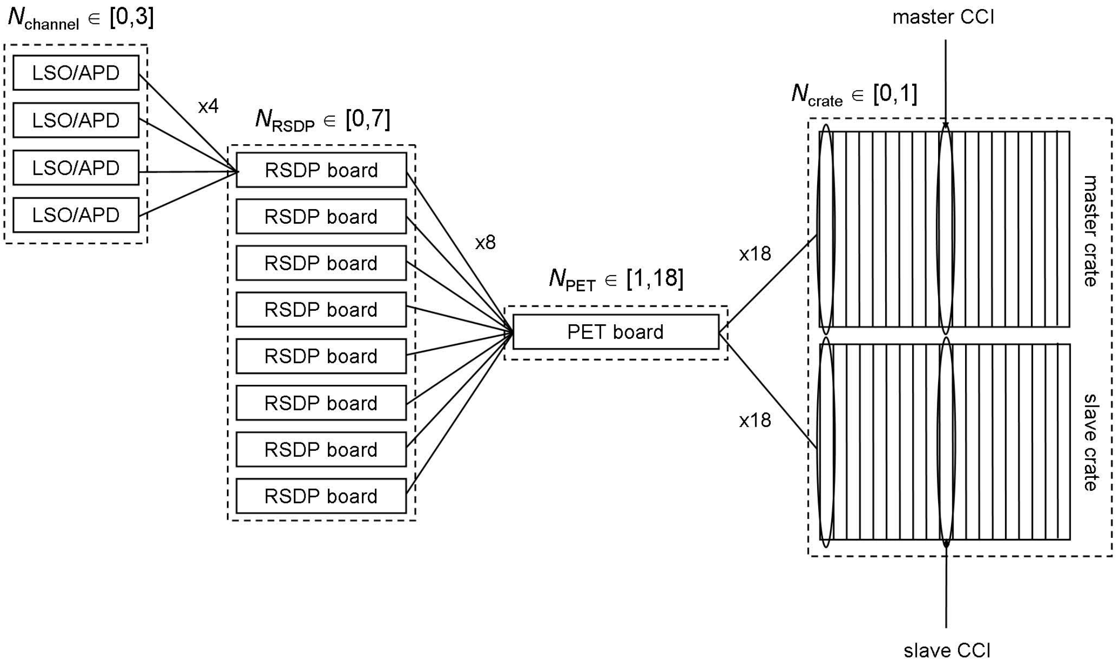

Figure 3.14: Block diagram showing the arrangement of the data acquisition electronics for MADPET-II.

A block diagram that summarizes the complete electronic path of one LSO-APD detector signal is shown in Figure 3.15.

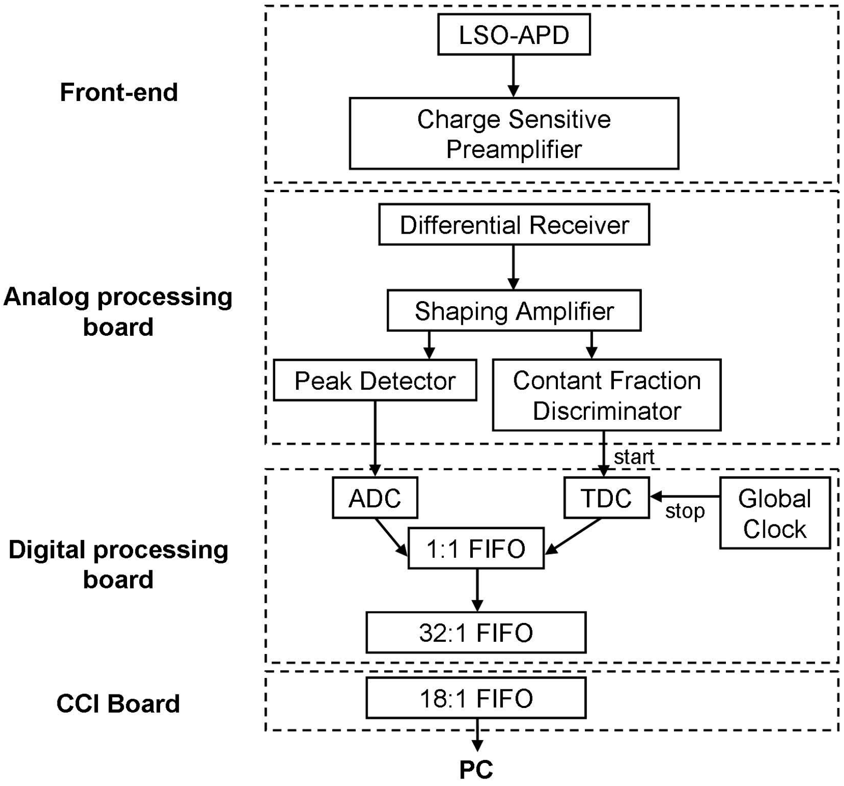

Figure 3.15: Summary of the complete electronic path from the front-end to the extracted pulse height and time stamp information.

3.6 True list-mode data acquisition, processing and reconstruction

The raw event data stream coming from the data acquisition electronics is organized in two 32-bit words for every detected singles event. The first word provides information about the crate number ($N_{crate} \in [0,1]$, 0 for master crate and 1 for slave crate, as shown in Figure 3.14), the RSDP board number ($N_{RSDP} \in [0,7]$, numbering refers to the 8 RSDP boards mounted in each PET board), the number of the triggered electronic channel ($N_{channel} \in [0,3]$, numbering refers to the 4 electronic channels of each RSDP board), the ADC output ($E_{ADC} \in [0, 2^{10} - 1]$) and the TDC output ($t_{TDC} \in [0, 2^{15} - 1]$). The second word contains information about the number of the PET board that contains the triggered channel ($N_{PET} \in [1,18]$, numbering refers to the 18 PET boards mounted in each crate) and the time counter ($t_{counter} \in [0, 2^{25} - 1]$). The time counter is initiated by the Global sync and provides a coarse time information which will be combined with the finer time information provided by the TDC in order to extract a time stamp attributed to every detected event. The actual number of the triggered electronic channel is calculated by Equation 3.1:

$$channel = N_{channel} + 4 * N_{RSDP} + 32 * (N_{PET} - 1) + 576 * N_{crate} \tag{3.1}$$

The actual time stamp of each detected event is calculated by Equation 3.2:

$$\begin{aligned} time = t_{TDC} * resolution_{TDC} + t_{counter} * resolution_{counter} + \delta t + \\ + overflows * t_{counter} * resolution_{counter} \end{aligned} \tag{3.2}$$

where δt is a time correction factor that compensates for inherent interchannel delays originating from the front-end, the analog and digital electronics. The calculation of the time correction factors for the 1152 electronic channels of the tomograph is described in Section 4.2. As previously mentioned, $resolution_{TDC}$ is 333 ps and $resolution_{counter}$ is 3.2 μs. The parameter $overflows$ indicates how many times the time counter had to reset during the acquisition.

The acquired data are stored in list-mode format, namely a data stream containing rows of the above calculated channel, energy and time stamp for every detected singles event is recorded. Since the scanner's hardware does not contain any coincidence units, coincidences are sorted in software from the acquired singles data stream. The coincidence sorting logic is illustrated in Figure 3.16.

The first event in the data stream initiates a time window whose width is traditionally chosen to be twice the system's measured time resolution, although timing windows of variable widths may be applied. The events that fall within this window are considered to be in coincidence with the event that initiated the window.

- If only one event is detected within the window, the attributed coincidence is labelled as a "double prompt"

- If two events are detected within the window, the attributed coincidence is labelled as a "triple prompt"

- If more than two events are detected within the window, the attributed coincidence is labelled as a "multiple prompt".

The process is then repeated for the next detected event that falls outside the coincidence window and continues until no detected events are left in the data stream. The sorted coincidences are characterized as "prompts" since they are the sum of the true, the random and the scattered coincidences, as defined in Sections 2.1.2 and 2.1.3.

For the estimation of the random coincidences, the delayed window method is currently applied on the measured data, however different estimation methods have been evaluated [105]. According to this method, every singles event which initiates a prompt window, also initiates a second time window shifted at a constant delay compared to the prompt (red window in Figure 3.16). Based on the assumption that the accidental coincidences are homogeneously distributed in time, a statistical estimation of random coincidences is made assuming that every singles event that falls within the delayed coincidence window is considered to form a random coincidence with the singles event that initiated the prompt window. Double, triple or multiple random coincidences may be sorted in the same way described above.

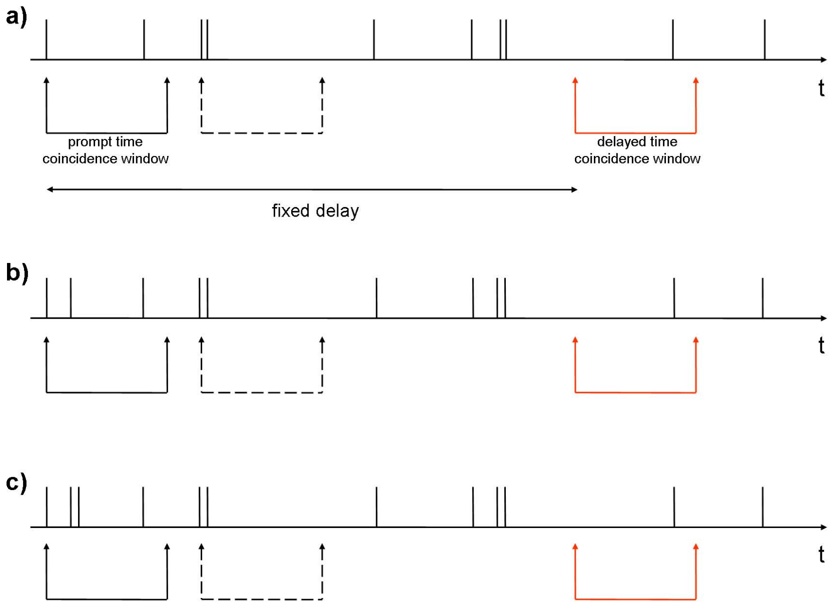

Figure 3.16: Illustration of the coincidence sorting logic in the case that a) one ("double prompt"), b) two ("triple prompt") or c) three ("multiple prompt") events fall within the prompt coincidence window (black solid line). The delayed coincidence window (red solid line) is also initiated by the trigger event for the estimation of accidental coincidences. A subsequent prompt coincidence window is also shown (dashed line) in order to demonstrate that the coincidence sorting technique is repeated for the next event that falls outside the previous coincidence window.

For every pair of channels, $channel_1$ and $channel_2$, which is found to be in coincidence, a LOR number is assigned as defined by Equation 3.3:

$$LOR = channel_1 + 1152 \cdot channel_2 \tag{3.3}$$

where $channel_1$ and $channel_2$ are defined by Equation 3.1 with $channel_1 > channel_2$. According to Equation 3.3, channel 0 will form with channels 1 to 1151 LORs 1 to 1151 respectively, channel 1 will form with channels 2 to 1151 LORs 1154 to 2303 and the numbering is repeated in a similar way for all 1152 channels. The condition $channel_1 > channel_2$ is set in order to avoid redundancy in the LOR numbering for a specific detector pair, as well as non-physically meaningful LORs, i.e the LOR formed between one detector and itself.

The coincidence sorting procedure will result in a file containing a list of all the LORs present in the system and the number of detected prompt coincidences in each LOR. A similar file is also created for the detected random coincidences. The two files are then used as an input to the image reconstruction algorithm. Therefore, MADPET-II does not make use of sinograms (Section 2.1.8).

It should be pointed out that the above presented methods for the estimation of prompt and random coincidences may be subjected to reduced accuracy in the same degree as any hardware-based coincidence detection method, i.e the use of coincidence units. However, the flexibility of sorting coincidences post acquisition from singles data streams allows for investigation of different coincidence sorting schemes [105, 102].

MADPET-II images are reconstructed using the MLEM algorithm. As mentioned in Section 2.1.8, MLEM belongs to the category of statistical iterative reconstruction algorithms which take into account a model of all the physical processes apparent to the detection of radiation from the specific tomograph [45]. This model is called System Matrix and in the case of MADPET-II is calculated using Monte Carlo simulations [85]. The reconstructed image is a three dimensional (xyz) array consisting of voxels (three dimensional pixels) with dimension of $0.5 \times 0.5 \times 0.5$ mm^3 each. Since the FOV of MADPET-II has dimensions of approximately $70 \times 70 \times 20$ mm^3, the array consists of $140 \times 140 \times 40$ voxels [11]. The intensity (number of counts) of each voxel in the reconstructed image is indicative of the radioactivity concentration. Figure 3.17 illustrates the structure of the reconstructed image with respect to the FOV of the tomograph.

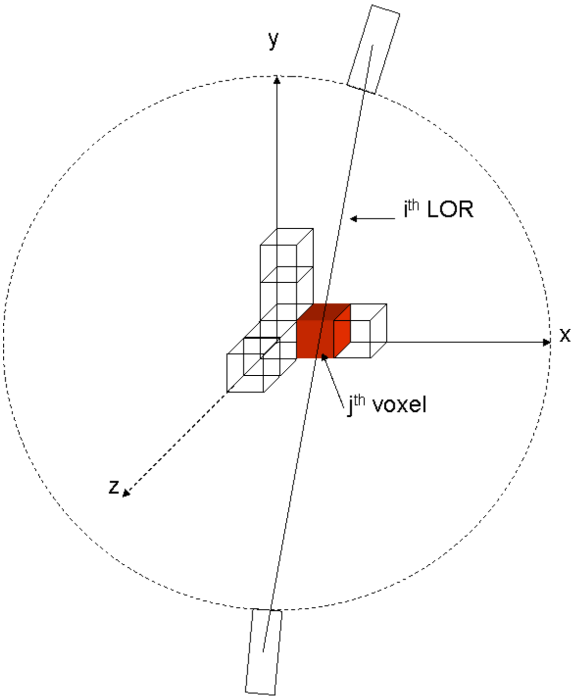

Figure 3.17: Voxelization of the MADPET-II FOV. The FOV consists of 140 voxels in the x, 140 voxels in the y and 40 voxels in the z direction. The voxel size is $0.5 \times 0.5 \times 0.5$ mm^3, but for clarity is exaggerated in the figure. A dashed circle with a detector pair is also illustrated in order to relate the physical FOV (shown in the figure only for the x-y plane) with the reconstructed FOV.

The system matrix, on the other hand, is a two dimensional array whose elements a_{ij} indicate the probability that a pair of photons emitted from voxel j will be detected along the LOR i (Figure 3.17). Thus, the intensity of each element in the system matrix varies in the range [0, 1]. By introducing this probability matrix (system matrix) to the reconstruction algorithm we are able to take into account both the specific geometry of MADPET-II, such as the crystal pixel size, the geometry of each 4×8 detector array and the dual radial detector layer, as well as the statistical variations introduced in the detection of photons by the system. Table 3.1 summarizes the advantages and drawbacks of the DAQ special features of MADPET-II.

DAQ features	**Advantages**	**Disadvantages**
List-mode data format: Recorded time stamp and pulse height for every detected event	Maximum flexibility in data processing	Disc space requirements
Post-acquisition coincidence sorting	Application of variable energy and time coincidence windows	Processing time
Software based tomograph tuning: • Pulse height calibration • Timing calibration • Randoms subtraction	Evaluation of different methods	Timing walk effects
3D list-mode MLEM reconstruction with a Monte-Carlo-based system matrix	Detection process taken into account	• Duration of reconstruction • Effect of limited statistics on image noise

Table 3.1: The pros and cons of the special acquisition features of MADPET-II.

Chapter 4

Results: Front-end and system performance evaluation

4.1 Evaluation of the analog signal processing electronics: pulse height linearity, timing walk and jitter.

Work published in Nuclear Methods
in Physics Research (V. C. Spanoudaki
et al. NIMA 564(2006) pg. 451–462)

As outlined in Chapter 3, the detector signals of MADPET-II have to undergo an analog signal processing step prior to digitization. Energy and time information is represented by the output of a peak detector and a constant fraction discriminator both implemented in the same integrated circuit (RSDP ASIC). The performance of this ASIC has been evaluated with test input pulses of 1 kHz frequency. The test input fed to the RSDP board, as well as the resulting output signals are shown in Figure 4.1.

The input to the differential receiver is a rectangular pulse of 500 mV amplitude, 2 ns rise time and 10 μs width (solid black line in Figure 4.1a). This input undergoes differentiation (dotted red line in Figure 4.1a). The amplitude of the filtered (differentiated) pulse can be regulated with the use of attenuators having a range from 140 mV to 14 mV, which corresponds to a 10:1 dynamic range. The peak detector (Figure 4.1c) detects and holds the maximum amplitude of the shaped signal (Figure 4.1b). The trigger output (Figure 4.1d) is a rectangular pulse of 3.3 V and its width, as well as the width of the peak detector output, is limited by the presence of the reset signal, namely both the trigger and the peak detector outputs switch to logic 0 when the reset pulse switches to logic 1 (Figure 4.1e). The reset input is a 2.5 V rectangular pulse of 6 μs duration and delayed with respect to the differential input pulse so that it occurs at its falling edge.

The trigger signal of the arming discriminator is produced when the shaped signal crosses a threshold voltage created by DACs mounted on the PET board. The threshold is set individually for every electronic channel to a level high enough to avoid triggering

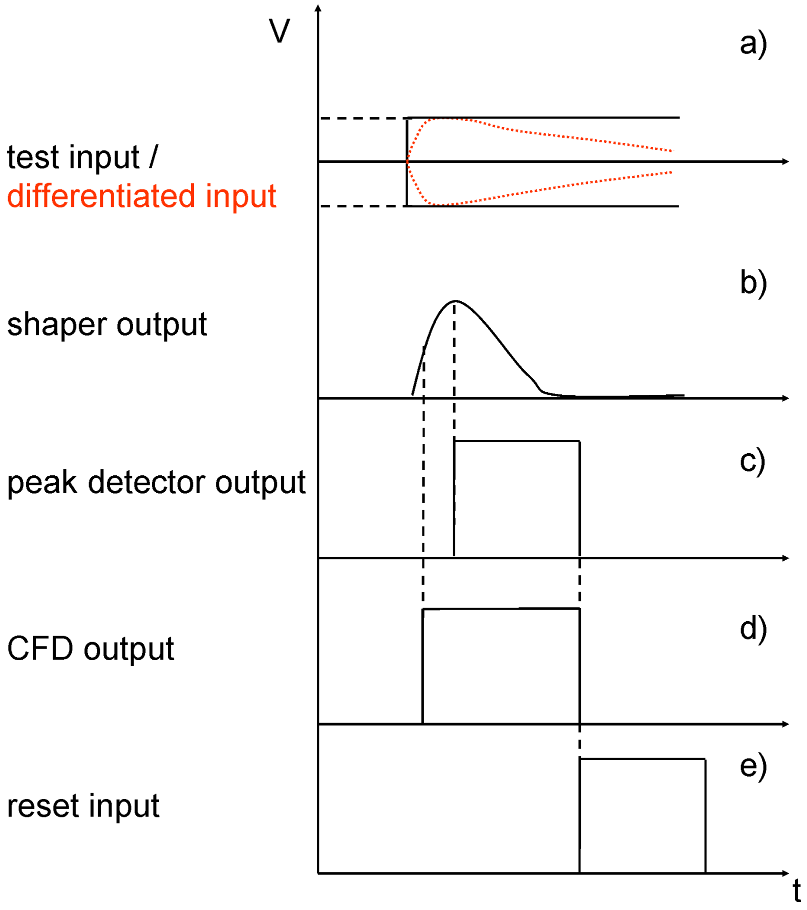

Figure 4.1: From top to bottom: (a) test input, (b) shaper output, (c) peak detector output, (d) CFD output and (e) reset input used to evaluate the performance of the RSDP boards. For illustration purposes, the amplitudes and durations of the signals are irrelevant.

on noise but low enough in order to record events with very low energies. In Figure 4.2, a typical distribution of lower hardware energy thresholds (arming discriminator thresholds) among 384 channels of the tomograph is depicted. It is obvious from the figure that the threshold values for most channels lie between 100 and 200 keV, which means that events below this threshold are excluded since they can not be distinguished from the noise level. However for a number of channels with poor gain and energy resolution, the hardware threshold needs to be set to higher values. Since all singles data are stored to disk and coincidences are sorted post-acquisition, the common lower energy threshold for all channels is set in software and events are discriminated based on ADC information.

To create the bipolar input of the zero-cross discriminator, CFD uses a one-pole high-pass filter instead of a delay line, as described in Section 3.4 (Figures 3.9 and 3.12). The C and R values of the high-pass filter will define the time constant of the high-pass output and, consequently, the undershoot and the zero-cross slope of the produced bipolar pulse (CFD input in Figure 4.3). Increasing undershoot until the undershoot-to-overshoot ratio of the bipolar pulse is approximately 1 to 3, and increasing zero-cross slope lead to

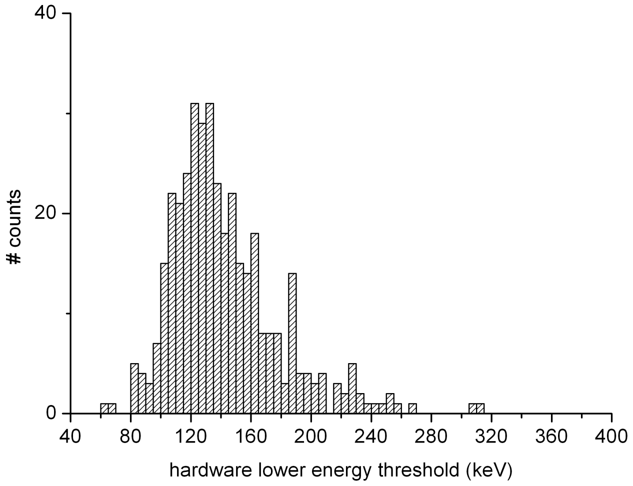

Figure 4.2: Distribution of lower energy thresholds set by hardware among 384 channels of the tomograph.

less walk, less jitter and thus more accurate time pick-off. Walk is the dependence of the trigger position on pulse height and/or rise time, as defined in Section 3.4 (Figure 3.8), and jitter is the time uncertainty with which a signal is crossing a threshold due to noise superimposed on the signal [1]. Timing jitter (measured in ns in the current analysis) is usually given by the formula

$$\sigma_{time} = \frac{\sigma_n}{\mid \frac{dV}{dt} \mid} \tag{4.1}$$

where σ_n (measured in the current analysis in mV) is the noise superimposed on the pulse and $\frac{dV}{dt}$ (in $\frac{mV}{ns}$) is the pulse slope at the crossing point between the pulse and the threshold.

The CFD subtracts the output of the high-pass filter from the shaped signal, and the zero-cross level of the resulting bipolar pulse defines the position of the CFD trigger output (Figure 3.12). The C component of the high-pass filter (C_{hp}) is a 0.5 pF capacitor and the R component (R_{hp}) is a 27 kΩ resistor connected in series with a 1 kΩ potentiometer. By properly adjusting the voltage drop across the terminals of this potentiometer, the DC voltage offset of the high-pass output and therefore the zero-cross level at which the CFD will produce the trigger may be regulated (bottom graph of Figure 4.3). This offset has to be set at a minimum value that results in best walk performance. Below this minimum value the time at which the logic AND of the zero-cross and the arming discriminator triggers is equal to the time at which the arming discriminator triggers (Figure 3.10), thus the CFD degenerates to a leading edge discriminator (Figure 3.8). The simulated input and output signals for C_{hp}=3 pF are depicted in Figure 4.3. As will be discussed in Section 4.1.3, C_{hp}=3 pF is expected to minimize the ASIC's walk to hundreds of ps. In the same figure a more detailed illustration of the dependence of the extracted time information on the DC zero-cross level is shown.

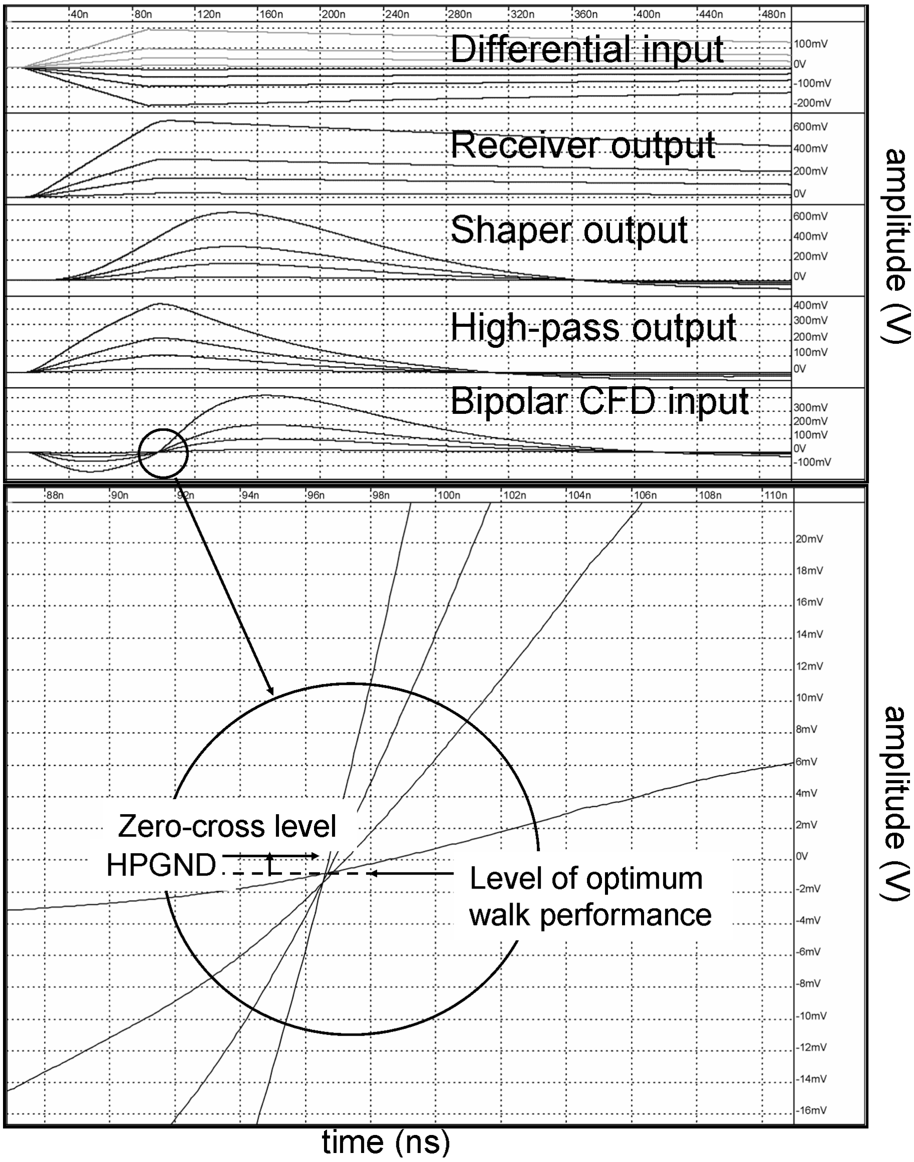

Figure 4.3: Simulated input and output signals for C_{hp}=3 pF. The dependence of CFD walk performance on the zero-cross level of the bipolar imput is also illustrated.

Although there is an optimum potentiometer setting for each individual electronic channel that guarantees the best timing performance, there is only one such potentiometer mounted on each RSDP board and therefore all four channels of the chip will have the same zero-cross level. The choice of this voltage level must be the highest of the four optimum values to assure that none of the four CFD trigger outputs becomes the trigger of the arming discriminator, as explained in the previous paragraph. This is a design flaw which will be addressed in Section 4.1.3. Consequently, three of the four channels of each board will not show optimum timing performance in terms of walk.

Finally, it has been found that the small fluctuations on the zero-cross level caused by fluctuations on the RSDP power supply (±2.5 V) can be minimized by implementing to the RSDP board a voltage reference (LM4041, National Semiconductor) whose output voltage has a fixed value of 1.225 V for values of the supply voltage above 2 V. Therefore, for fluctuations of the supply voltage within the range 2 to 3 V around the mean value of 2.5 V, the voltage reference has a stable output of 1.225 V with small fluctuations within the range 1.224 to 1.226 V. With the above power supply of approximately 1.225 V, the voltage across the potentiometer that regulates the zero-cross level of the CFD has been measured to range from 0 to 66.3 mV and can be adjusted to a fixed value with an accuracy in the order of 0.1 mV, minimizing therefore the variation in walk performance in the order of hundreds of ps. Such a voltage reference has been implemented to every RSDP board to assure the stability of the DC zero-cross level for every four electronic channels.

The performance of each of the electronic parts of the chip can be controlled using variable resistors, which regulate the bias currents of the shaping amplifier, the differential receiver, the peak detector, and the zero-cross discriminator. Henceforth these bias currents will be labeled with the initials S, D, P and T respectively. The bias currents were adjusted to the appropriate values to obtain signals exhibiting the following characteristics:

- the output of the shaping amplifier should have a smooth shape, a short rise time (below 100 ns) and a large amplitude so that all signals within 5:1 amplitude dynamic range are distinguishable from noise (adjustment of S (shaper) and D (differential receiver) bias)
- the output of the peak detector should have a large amplitude and should perform linearly (adjustment of P (peak detector) bias)
- the walk and the jitter of the CFD trigger output should be as low as possible, less than one ns in order to achieve time resolution in the same range (adjustment of T (zero-cross) bias)

The above characteristics are very important for the extraction of energy and timing information. Provided the linear performance of the peak detector, a high amplitude of the shaper and the peak detector signals along the whole dynamic range of interest may lead to increased number of detected events above the noise level. The small rise time and, consequently, the steep slope of the signal will reduce the walk effects and time jitter.

According to the above criteria, the linearity of the peak detector and the susceptibility of the CFD to walk effects for 32 RSDP boards, or 128 individual electronic channels, have been studied.

4.1.1 Linearity of the peak detector

In order to measure the linearity of the peak detector, differential input pulses with different amplitudes were fed to the chip. The different pulse amplitudes were realized using an input pulse of constant amplitude and an attenuator with a step size of 2 dB within a range 10 to 32 dB, corresponding to a dynamic range of approximately 10:1. Linearity was measured for various gain settings, various peak detector bias currents P (in terms of bias voltage with a range -2.5 to 0 V rather than current since the latter is not easily measured on the PCB board) and different shaping time constants.

It has been observed that the gain value does not significantly affect the linearity. Figure 4.4 depicts linearity plots for one typical channel of a RSDP board and two different values of shaping time for the same gain value of 4.8. The experimental data plotted show that a linear behaviour is followed. The Pearson correlation coefficient calculated from linear regression of the above data has a value of $R^2 = 0.99939 \pm 0.00008$ for 100 ns shaping time and a value of $R^2 = 0.9962 \pm 0.0006$ for 50 ns shaping time. The integral linearity of the peak detector, that is the maximum deviation of the experimentally estimated curve from the best linear fit applied to it [42], has also been estimated to be (1.68±0.24)% and (4.4±0.6)% for 100 and 50 ns shaping time, respectively. Even though the difference in linearity is not significant for the different shaping times, the 100 ns value was chosen since the signals coming from the front-end electronics have a mean rise time of approximately 60 to 80 ns.

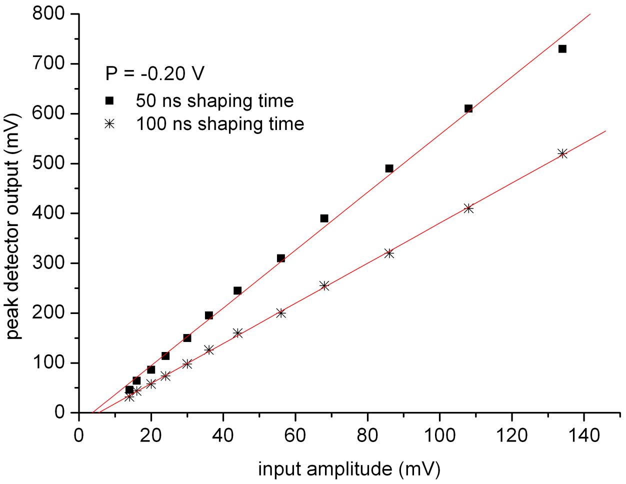

Figure 4.4: Linearity performance of the peak detector for 1 electronic channel and two shaping times (50 and 100 ns).

In Figure 4.5 the combined dependence of linearity on the peak detector bias voltage (label P on the figure) and on the shaping time selected for the shaper is shown. It is obvious from Figure 4.5 that a bias voltage P between 0.1 and 0.2 V (absolute values) for 100 ns shaping time results in the highest possible linearity of the peak detector (R^2 values). For 50 ns shaping time and for values of P smaller that 0.3 V, the linearity is degraded in comparison to the 100 ns shaping time. This trend is inversed for P values larger than 0.3 V, nevertheless the linearity is significantly smaller, for both shaping times, than the one achieved for P within the range from 0.1 to 0.2 V. The same linear behaviour has been observed for all the RSDP boards that have been tested and is characterized by $R^2 = 0.99945 \pm 0.00002$.

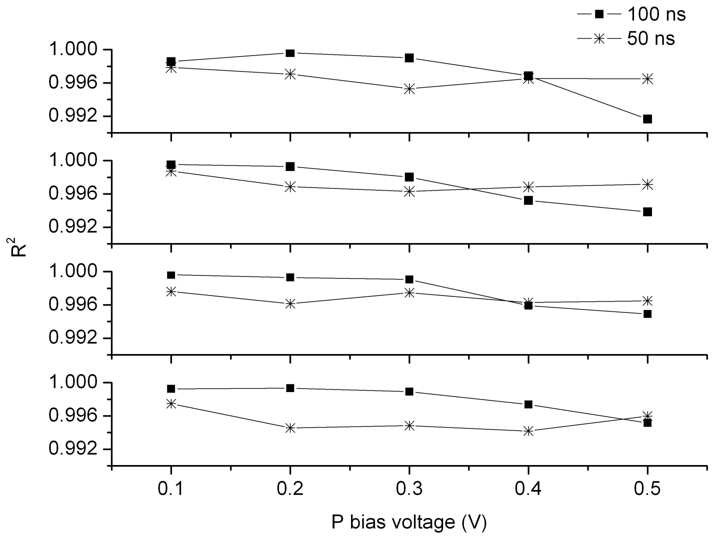

Figure 4.5: Dependence of the peak detector linearity on the selected value of the peak detector bias voltage (symbol P in the diagrams) for different shaping times (50 and 100 ns). The four graphs correspond to the first channel of four individual RSDP boards. Absolute values of the bias voltage P are used in this graph.

4.1.2 Walk and jitter performance of the Constant Fraction Discriminator

The performance of the CFD has been evaluated in terms of walk and jitter. For both measurements, a pulse with 2 ns rise time and an amplitude that varies with the use of an attenuator, has been fed to the ASIC. For an attenuation in the pulse amplitude from 20 dB to 36 dB, which corresponds to a 5:1 input dynamic range, the difference in the CFD trigger position has been measured (indicated as walk in Figures 4.6 and 4.7) for various values of the CFD zero-cross level. In addition, the trigger jitter has been determined by measuring the deviation of the trigger position with respect to a mean value when attenuating the input test pulse from 20 dB to 36 dB. It has already been mentioned that the front-end output pulses, which would be the real input of the RSDP boards, have a rise time between 60 and 80 ns. Nevertheless, this difference in rise time between the test and the real input pulse is expected to slightly affect the results of the performance measurements since the shaped signal, from which both energy and time information are extracted (see Figure 3.12) has a fixed shaping time of 50 or 100 ns.

The dependence of timing walk (measured shift of trigger position for an input amplitude dynamic range of approximately 5:1) on the zero-cross DC level of the CFD, which will be henceforth referred to as HPGND, is shown in Figure 4.6 for two different RSDP boards and for 100 ns shaping time. This dependence was plotted for different values of the trigger bias voltage (labeled T on the figure). It is obvious that the smallest walk is approximately 2 ns for a small HPGND (value approximately 6 mV) and for values of the trigger bias voltage between -1 and -1.1 V. The strong dependence of the CFD performance, in terms of walk, from HPGND is predicted by simulations of the ASIC as shown in Figure 4.3.

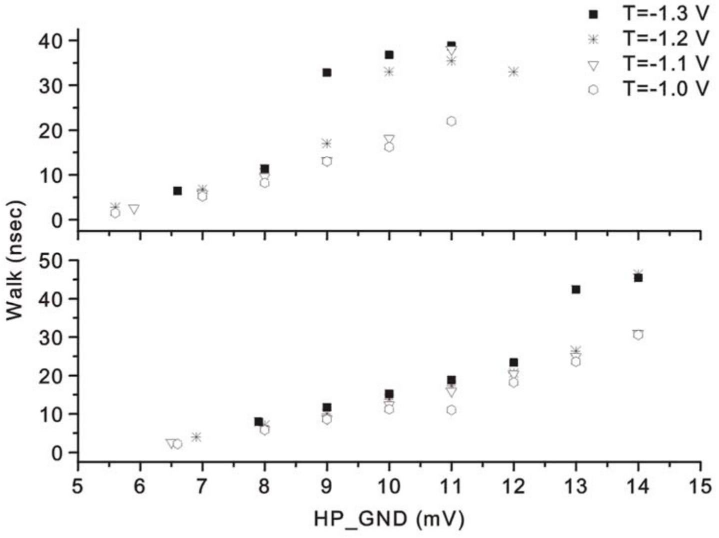

Figure 4.6: Time walk performance for two different RSDP boards and for different values of the trigger bias voltage (symbol T in the diagrams).

In general, the HPGND varies from a minimum value below which the CFD trigger degenerates to the arming trigger, as previously outlined, up to a maximum value above which the jitter of the trigger for 36 dB attenuation becomes significant, as shown in Figure 4.7. In this figure, the CFD trigger position, as displayed on an oscilloscope screen, is depicted for 20 and 36 dB attenuation of the input signal. Since it has been observed that the trigger bias voltage does not affect the jitter, all measurements presented here have been performed for the optimum value of T=-1.1 V. The histograms drawn upside down on the upper part of the display are indicative of the trigger jitter which, for high attenuation and high HPGND value (HPGND=14 mV for this measurement, optimum HPGND=6.5 mV), is on the order of 10 ns peak-to-peak value (bottom picture of Figure 4.7).

The dependence of jitter (peak-to-peak) on the HPGND values is shown in Figure 4.8. Increasing HPGND leads to higher jitter and this dependence becomes more significant at lower input pulse amplitudes. The rms values of jitter are 0.8 ns for 20 dB and vary within the range from 2 to 4 ns for 36 dB and increasing HPGND value. In Figure 4.9, the variation of minimum (optimum) HPGND setting as a function of the trigger bias voltage T is shown. The range -1 to -1.1 V for T is the preferred one since it corresponds to the minimum possible value of HPGND and thus, as seen from Figure 4.6, to minimum walk performance.

It is important to note that a small variation in the value of HPGND can lead to significant increase in walk. The dependence of walk on the HPGND shown in Figure 4.6 is not perfectly linear, especially for higher absolute values of T, where a shift in walk may be observed, as the HPGND increases. Nevertheless, a linear fit applied to the curves that correspond to T=-1 and -1.1 V indicates a walk dependence of 3.77 ns per 1 mV increase

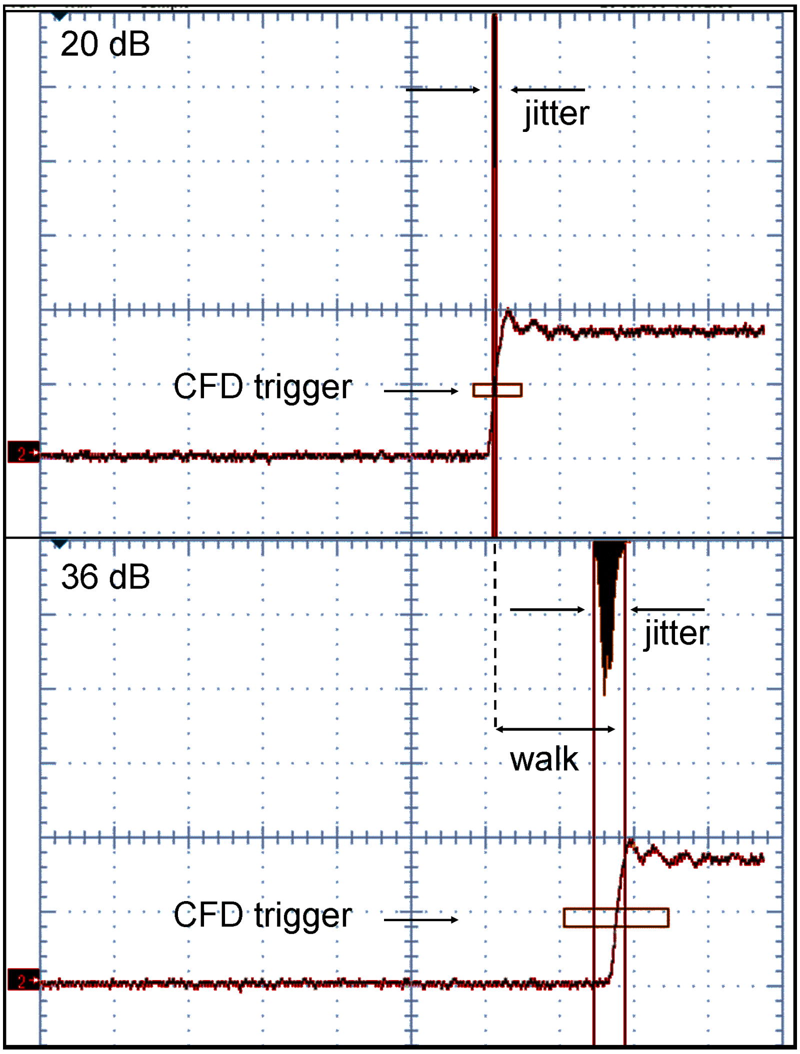

Figure 4.7: CFD output, as observed on the oscilloscope display for 20 dB (top) and 36 dB (bottom) attenuation of the signal. Walk (difference in the trigger position for the two amplitudes), as well as jitter (variation of trigger position around a mean value) are evident.

in HPGND. The linear fits are characterized by $R^2 = 0.982$ for T=-1.0 V and $R^2 = 0.977$ for T=-1.1 V.

It can be seen from Figures 4.7 and 4.9 that the sensitivity of walk performance to variations of the zero-cross discriminator DC level, as well as its minimum possible value, are not optimal for the development of a high performance small animal LSO-PET scanner.

4.1.3 The problem of fully integrated CFDs: degradation to leading edge performance and inherent delays among electronic channels

For every RSDP board there exists only a single adjustment of the zero-cross level and therefore only one of the four electronic channels may exhibit optimum timing performance. This necessitates the application of a correction on the timing information received by the analog signal processing electronics. Figure 4.10 shows an example of one

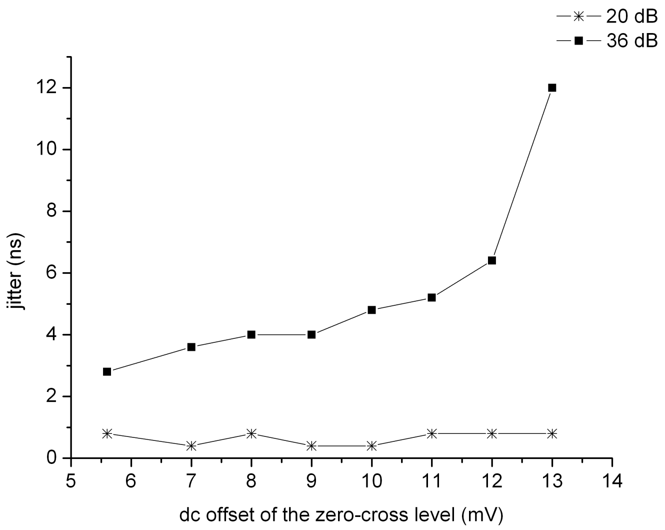

Figure 4.8: Dependence of jitter on HPGND for 20 dB and 36 dB attenuation of the input signal which corresponds to approximately 5:1 amplitude dynamic range.

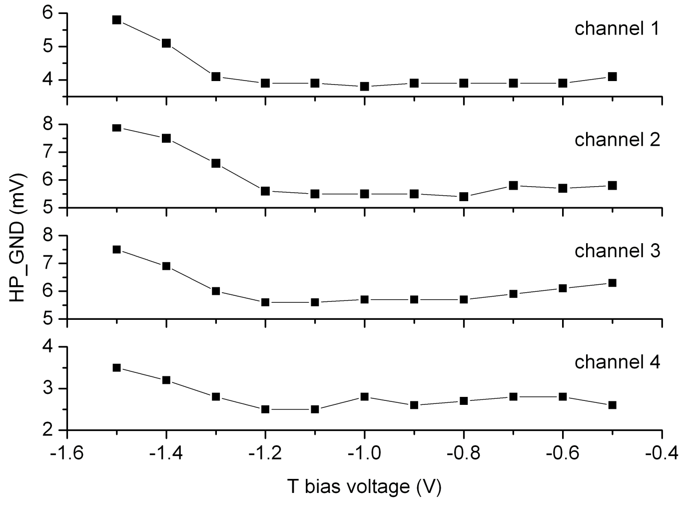

Figure 4.9: Dependence of the minimum (optimum) HPGND setting on the trigger bias voltage T for the four different channels of the same ASIC.

RSDP board for which channels 1, 2, 3 and 4 are characterized by minimum HPGND values of 8.8, 2.9, 2.8 and 1.8 mV respectively. In order to avoid the situation where one or more of the four channels trigger on the arming discriminator threshold, the HPGND value for this RSDP board is set to 8.8 mV. Thus, the dependence of the trigger position on the pulse amplitude (walk) is minimized, even though it is not optimum, for the first electronic channel and worsens for the other three, especially for small pulse amplitudes, as seen in Figure 4.10.

Theoretically, the output of a CFD is a trigger signal at the same time point (zero-cross point of the bipolar input pulse) for signals of different amplitudes but identical rise

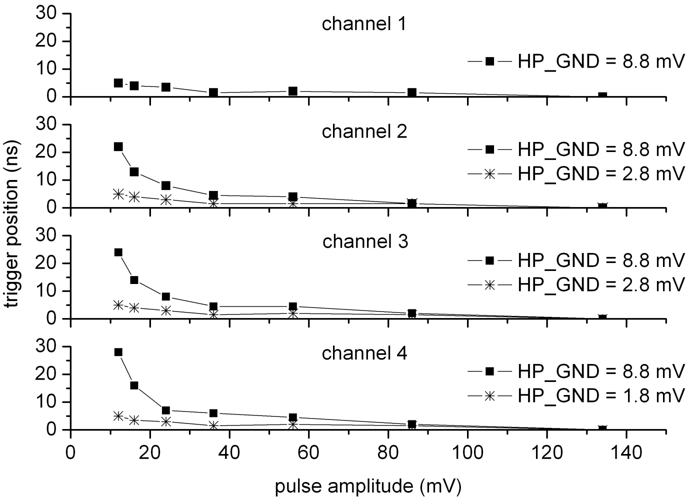

Figure 4.10: Trigger position as a function of input pulse amplitude for the 4 different electronic channels of the same ASIC. The first channel is characterized by the highest optimum HPGND value (8.8 mV). In the three last graphs, the trigger position versus amplitude for both channel significant optimum and highest optimum HPGND values are plotted.

times. From the above graphs, the trigger position seems to be not only dependent on the HPGND but also on the amplitude, and this dependence becomes significantly important for small amplitudes. This behaviour can be comparable to the leading edge time pick-off. Figure 4.11 shows the simulated walk effect of leading edge time pick-off (time and amplitude in arbitrary units) in comparison with the walk effect of one electronic channel for which the HPGND value is set to a value higher than the minimum one. It can be concluded that the performance of the CFD degenerates to leading edge performance if the zero-cross level is not set as low as possible. Plotting in the same graph (Figure 4.12) the trigger-amplitude dependence for the four channels of an ASIC for which channels 1, 2, 3 and 4 are characterized by HPGND values of 9.5, 5.6, 9.3, 7.8 mV respectively, one can see that for the same input amplitude, delays between channels are observed which increase with decreasing pulse amplitude. Modelling the walk behaviour of each individual electronic channel by applying fits to the curves of Figure 4.10, an amplitude dependent time correction can be assigned to each channel.

A histogram of the deviation of the final HPGND setting from the optimum value $(HPGND - HPGND_{optimum})$ for 128 electronic channels is plotted in Figure 4.13. The zero column of the histogram corresponds to the 32 electronic channels (1 for each RSDP board) for which the HPGND setting corresponds to their optimum. It can be seen from the graph that the distribution of HPGND stability is rather random in the range 0.1 to 5 mV. It is expected that for the complete system of 1152 electronic channels, the corresponding distribution would be limited within approximately the same range, and therefore a significant number of channels would have a HPGND setting greater than 1 mV above their channel specific optimum.

Provided that every electronic channel is time aligned with respect to the others, it is

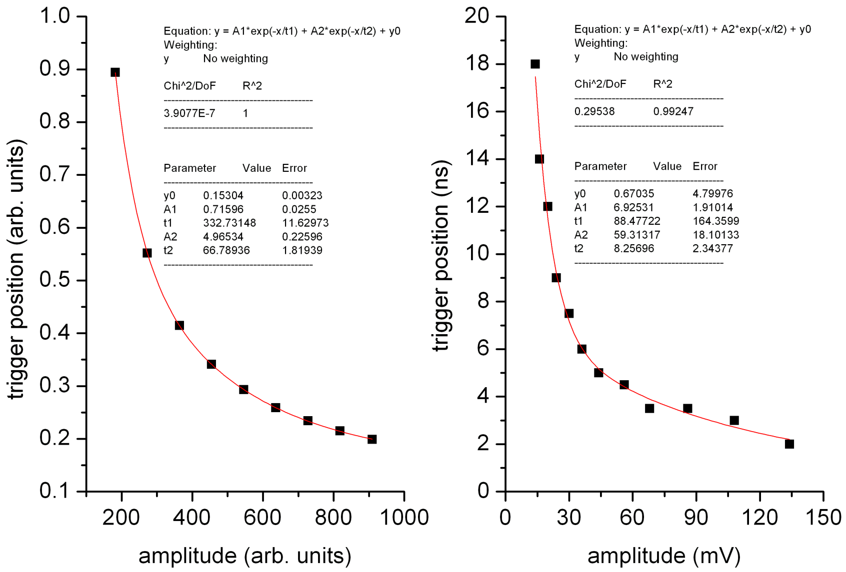

Figure 4.11: Simulated walk performance for leading-edge time pick-off (left) and walk performance for the constant-fraction time pick-off performed in one ASIC channel for a non-optimum CFD zero-cross level (right).

expected that the main contribution to the degradation of time resolution comes from the noise introduced in the signal from the peripheral electronics and the power supply as well as the jitter performance of the CFD. It should be noted that the power supply of the ASIC introduces a noise level of 15 mV rms and 70 mV peak-to-peak. According to Equation 4.1, the contribution of this noise to jitter has been estimated to vary from 2 to 8 ns for a 5:1 input amplitude dynamic range. From Figure 4.8, and for the worse case of approximately 5 mV variation of the HPGND setting (10 mV) from the optimum (5.6 mV for the specific electronic channel studied in this figure) the rms jitter varies from 0.8 to 4.8 ns for the same dynamic range. These numbers are consistent with the system-wide time resolution of the tomograph which has been measured to vary between 17 and 12 ns FWHM for lower energy thresholds 100-450 keV.

Walk and amplitude dependent delays between channels can significantly increase the system-wide timing resolution since the time coincidence spectra for every possible LOR are characterized by different centroid values (Section 4.2). In order to compensate for this effect a number of possibilities are currently under investigation:

- Possible redesign of the ASIC with a different value of the C component of the high-pass filter (current value C_{hp}=0.5 pF, new value C_{hp}=3 pF). Simulations of the new ASIC design have shown a decrease of the timing walk to approximately 200 ps for a 5:1 input dynamic range, as shown in Figure 4.14. The jitter is also expected to decrease due to the increasing undershoot and the zero-cross slope with increasing C_{hp} value.

- Possible redesign of the ASIC with 4 individual potentiometers in order to regulate

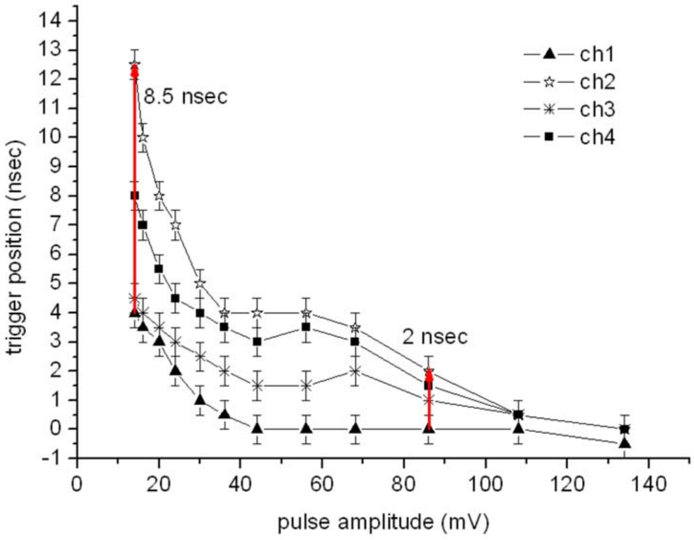

Figure 4.12: Trigger position as a function of input amplitude for the 4 different electronic channels of the same ASIC. The CFD zero-cross level has been set to the maximum of the four optimum HPGND values. The value for the trigger bias voltage T is set to -1.1 V.

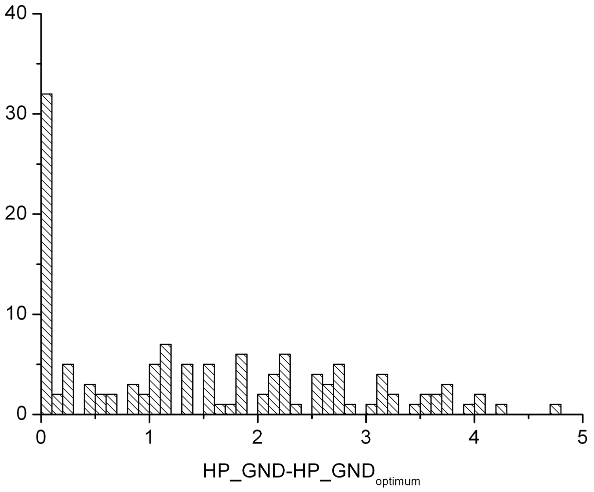

Figure 4.13: Distribution of the variation of the HPGND values among 128 electronic channels.

the zero-cross level of each electronic channel separately. In this way the zero-cross level will be set to the optimum value for every channel, so that walk and delays between channels are expected to be minimized.

- A time correction characterizing each electronic channel on the system can be estimated either iteratively [93] or by using a central alignment timing probe [57]. Another option, as mentioned before, would be to calculate the amplitude dependent channel delays from fitted curves on the walk graphs and store them in a look-up-

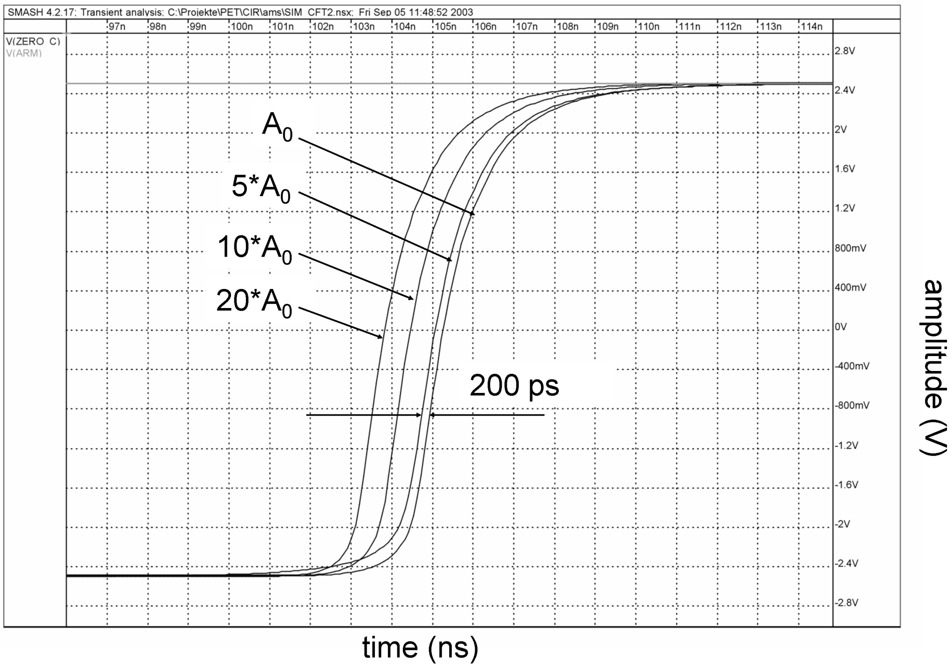

Figure 4.14: Simulated CFD output. The estimated walk is 200 ps for a 5:1 input dynamic range.

table. Applying these time corrections to every singles event detected by a specific channel leads to significant improvement of the system-wide time resolution.

4.2 Correction of interchannel delays and timing walk

The inherent delays among the numerous electronic channels of the tomograph and the walk effects addressed in the previous section may result in inefficient detection of coincidences within a finite time coincidence window. This leads to a decreased SNR in the reconstructed image. In the following paragraphs, two different methods used to correct for the interchannel delays in the case of MADPET-II are described. The last paragraph of this section describes the approach followed to compensate for timing walk.

4.2.1 An iterative, minimization method for correction of interchannel delays

For simplicity an example of a scanner consisting of four detectors, namely two detectors placed opposite to two others, as shown in Figure 4.15, is initially considered. The nomenclature for the channel and corresponding LOR numbering is also shown. Figure 4.16 illustrates the effect of interchannel delays on the time resolution for the above mentioned simplified case. The time difference histogram for a pair of detectors a and b in coincidence, which define a specific LOR i, is constructed by the difference $t_a - t_b$ of the corresponding time stamps for every detected coincidence event and characterized by a centroid value m_i. Due to delays between different detectors, the centroid values

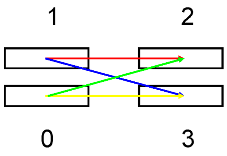

Detector pair	LOR #
0+2	0
0+3	1
1+2	2
1+3	3
$\frac{i-\mathrm{mod}(i,n)}{n}+(n+\mathrm{mod}(i,n))$	i

Figure 4.15: Example of a four-detector coincidence setup (2 detectors in coincidence with 2 opposite ones (n=2)). The numbering of the involved channels and LORs is explained in the table on the right.

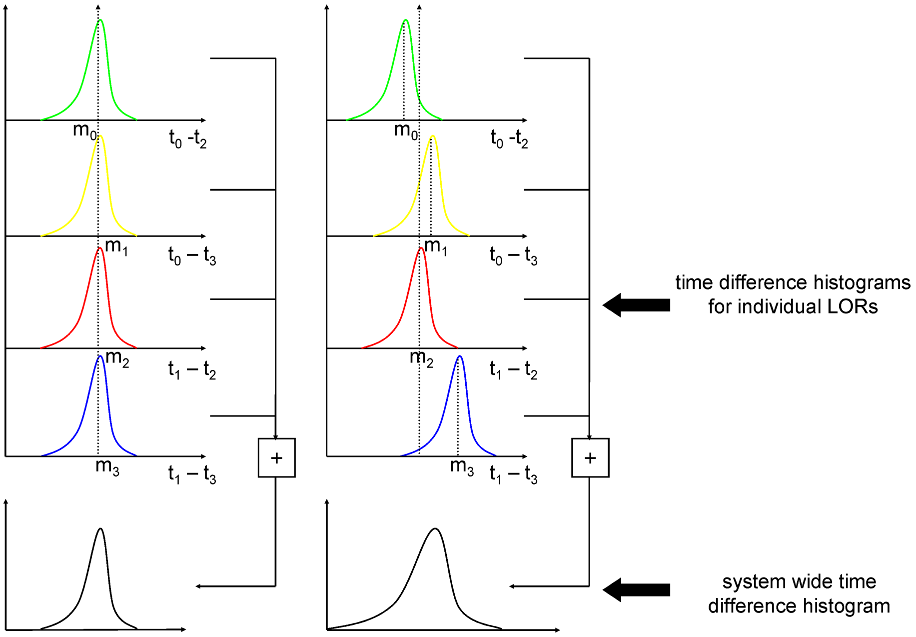

Figure 4.16: The problem of time alignment for four detector pairs in coincidence. If the detectors are correctly aligned in time (left), the system wide time resolution will be approximately equal to the individual detector pair time resolution. In the presence of interchannel delays, the centroids m_i of the corresponding time histograms (right) are shifted with respect to each other resulting in a broadening of the system wide time resolution.

m_i for all i LORs would deviate relative to their mean value m. If delays δt_a and δt_b are applied to the corresponding time stamps, then the resulting time difference histogram will be characterized by a new peak value

$$m_i' = m_i + \delta t_a - \delta t_b \tag{4.2}$$

The delays δt_a and δt_b are calculated so that the standard deviation f of the new peak values m_i' for all i LORs relative to their mean value would be a minimum.

An iterative method based on minimizing f has been developed [93]. The standard deviation f as a function of the vector $\vec{\delta t}$ containing the applied time delays for each individual channel is described by the following formula

$$f(\vec{\delta t}) = \frac{1}{\sqrt{n^2-1}} \times \sqrt{\sum \left(m_i + \delta t_{\frac{i-mod(i,n)}{n}} - \delta t_{n+mod(i,n)} - m - \frac{\sum \delta t_k - \sum \delta t_l}{n} \right)^2} \tag{4.3}$$

where n is the number of detectors on each side of the scanner and the variables k, l are given by the equations

$$k = 0...(n-1) \qquad l = n...(2n-1) \tag{4.4}$$

and

$$\vec{\delta t} = (\delta t_0, \delta t_1, ..., \delta t_{2n-1}) \tag{4.5}$$

In Figure 4.17, the time difference histogram for 256 channels before and after applying the calculated delays is shown. Data were taken for a centered flood Fluor-Deoxy-Glucose (^{18}F-FDG) source and coincidences were sorted for a lower energy threshold of 450 keV. A non-linear minimization algorithm was applied using the Conjugate Gradient method implemented in MINUIT [80, 60]. The calculated FWHM, and consequently the overall timing resolution, has been improved from 17.9 to 11.7 ns.

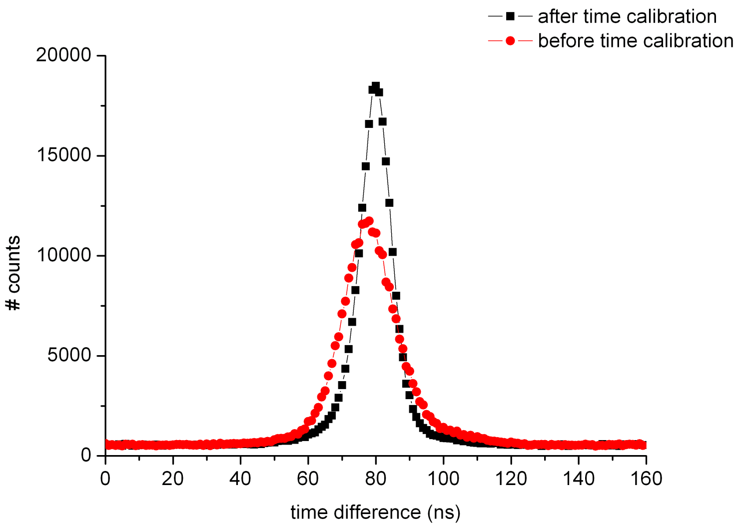

Figure 4.17: The summed time coincidence histogram before (red points) and after (black squares) time calibration using the iterative time alignment algorithm.

4.2.2 Use of an external signal reference for correction of interchannel delays

One very important drawback of the previously mentioned iterative method is that for increasing number of detectors and, therefore, for increasing number of possible LORs, the computational time can be very large, thus making the method cumbersome for the complete 1152 channel scanner. In comparison to the above method, a more straightforward and less time consuming way of time aligning the tomograph makes use of a timing probe (Scanwell Systems, Montreal) [103, 64, 57]. The probe consists of a ^{68}Ge positron emitting source incorporated into a plastic scintillator which is coupled to a PMT. In this case, the probe produces a signal for each positron decay of the source. The back-to-back emitted 511 keV photons resulting from the positron annihilation are detected by the LSO-APD detectors. Time difference histograms are plotted between the probe trigger signal and each individual detector signal. The time delays that will be applied as corrections to each detector are given by the centroids of the above time difference histograms. In contrast to the iterative method, the use of the timing probe provides a fast and more direct method of time alignment which is not restricted by the number of detectors in the scanner.

4.2.3 Correction for timing walk of the analog processing electronics

The two methods presented in the previous paragraphs result in a fixed delay value for every electronic channel of the system. This value would be accurate if estimated within an energy window around the photopeak; within this window, the output signals of a certain detector are characterized by a constant amplitude which may vary, however, due to the finite energy resolution. In addition, apparent variations in the gain among different detectors, even within a narrow energy window, lead to significant walk effects which further contribute to the values of the calculated delays. In Figure 4.18, a histogram of the photopeak position of all the 1152 channels of MADPET-II is shown. A coarse adjustment of the detector gain variations is performed prior to any software calibration through appropriate tuning of the APD bias voltage and the front-end temperature, as will be described in detail in Section 4.3. However, it is evident from the histogram that the large gain variations characterizing the MADPET-II detectors even after front-end

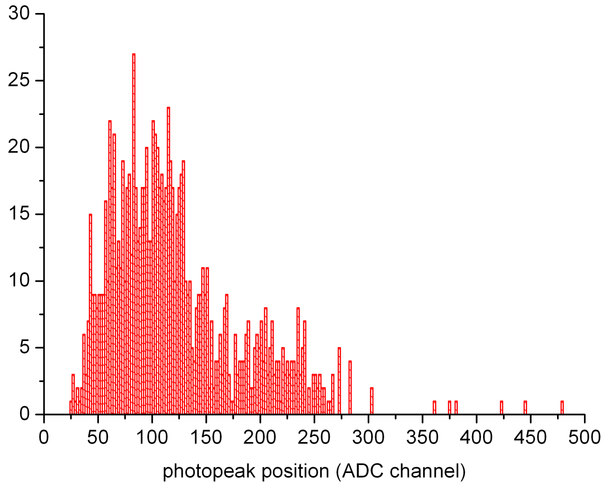

Figure 4.18: Histogram of the photopeak position among the 1152 detector channels of MADPET-II.

tuning, will inevitably lead to the above mentioned walk effects.

In addition, in the case of MADPET-II, the energy window would preferably be sufficiently wide extending down to the lowest possible values above electronic noise, in order to include the intercrystal scatter addressed in Section 3.1. In this case, there will be a large variety of different pulse amplitudes produced by the same detector due to the inclusion of the Compton continuum. Hence, a single delay value for the specific detector would be insufficient, as illustrated in Figure 4.19. The time resolution data presented in this figure have been corrected for interchannel delays which were calculated as follows:

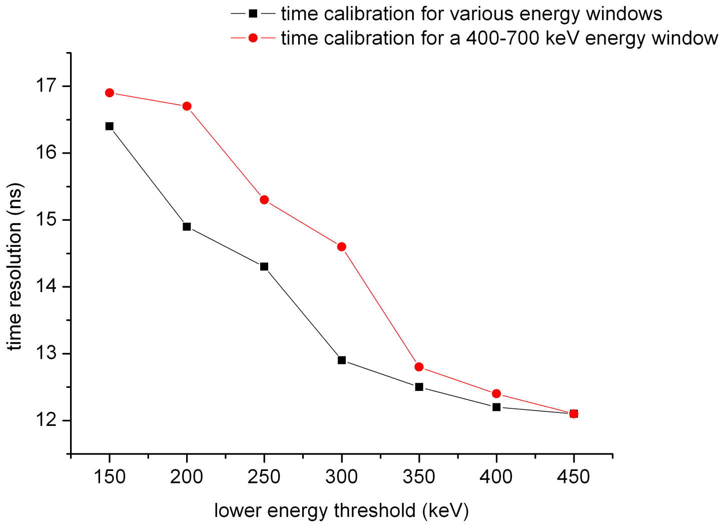

Figure 4.19: Calculated time resolution as a function of energy window. The upper energy threshold is set to 700 keV and the lower energy threshold varies from 150 to 450 keV, shown in the horizontal axis. A correction based on the methods presented in Sections 4.2.1 and 4.2.2 has been applied.

- for a narrow energy window around the photopeak (450-700 keV) (red circles in Figure 4.19)

- for various energy windows of fixed width, covering the complete energy range of 100 to 700 keV (black squares in Figure 4.19).

In both cases, as expected, the resolution values show an improvement as the lower energy threshold increases, namely as the energy window becomes narrower around the photopeak. However, an additional improvement in the resolution values for all lower energy thresholds is observed in the second case.

Taking this into account, a Look-Up-Table containing amplitude dependent delay values for every detector channel has been calculated, as already proposed in Section 4.1.3 and illustrated in Figure 4.20.

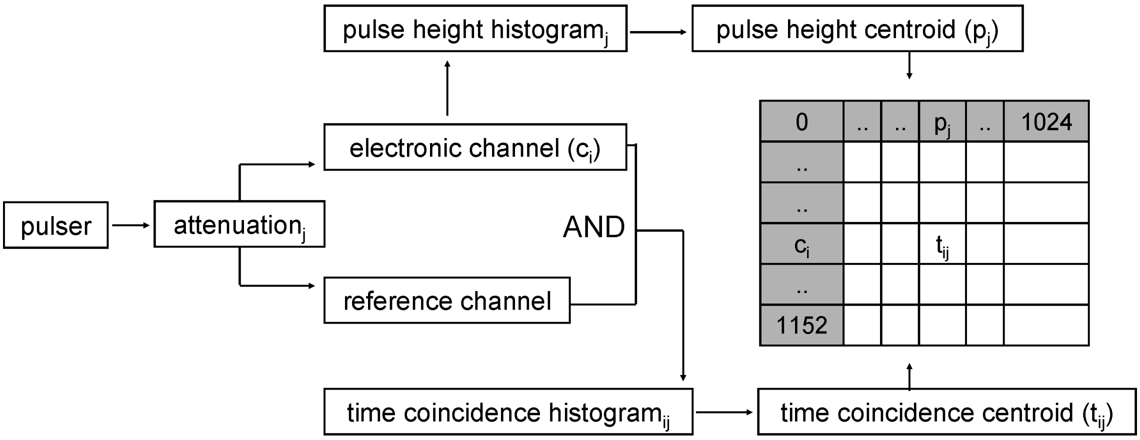

Figure 4.20: Block diagram of the measurement procedure followed in order to correct for interchannel delays and timing walk introduced by the analog processing electronics.

4.3 Evaluation of the front-end electronics: energy, time resolution as a function of temperature

Work published in Transactions on
Nuclear Science, Institute of Electrical
and Electronics Engineers (IEEE)
(V. C. Spanoudaki et al. TNS 55(2008)
pg. 469–480)

As outlined in Section 2.2.5, PET scanner detector technology is traditionally based on block detector architecture and light sharing techniques. However, systems employing individual readout of highly granulated crystals, such as MADPET-II, can offer improved spatial resolution and reduced dead time of the system due to minimum signal multiplexing. Nevertheless, these advantages are compensated by the requirement for both small size photodetectors as well as an equivalent large number of subsequent electronics that will collect the detector signals and further process them.

Depending on their power dissipation, the large number of front-end electronic channels can cause significant increase of temperature inside the tomograph gantry, thus affecting the gain of temperature sensitive photodetectors and the light output of the scintillation crystals. Despite a number of advantageous APD characteristics described in Sections 2.2.1 and 3.2, it has been shown that the APD gain decreases with increasing temperature [53]. The gain deterioration occurs since the magnitude of the lattice vibrations (phonons) in the APD material is enhanced with increasing temperature and the accelerated electrons lose energy by colliding with the crystal lattice, therefore they do not have sufficient energy to create secondary electrons by ionization [98, 2].

In addition, temperature dependence of the scintillation crystal light output has been observed. Studies have shown that the temperature dependence of the scintillator varies for different crystal materials [111]. In the case of LSO, the light output decreases in an almost linear way with increasing temperature for a wide range of temperatures, reaching a saturation point beyond which the light output is no longer temperature dependent [68]. Decreased light output is caused by thermal quenching, according to which increased temperature results in broadening of the emission and absorption bands of Cerium sites in the scintillation crystal [10]. As a result, the overlap between these bands increases and consequently a fraction of the produced optical photons is lost due to self absorption [42]. Hence, the combined performance of the LSO-APD detector module may deteriorate at high temperatures.

Decreased light output of the scintillator and decreased gain of the APD result in signals of smaller amplitude in the preamplifier output. Consequently, the acquired energy spectra will be shifted to smaller channels affecting the system calibration and possibly leading to degradation of the energy resolution. In addition, the results presented in Section 4.1 have demonstrated that the non-delay line CFD is subjected to walk and jitter effects which are enhanced at smaller pulse heights. Therefore, it is expected that increasing temperature will affect both time and energy resolution of the system.

The temperature effect on the stability and performance of the system has been evaluated by realizing a number of measurements focusing on the following:

- Investigation of the origin of temperature increase inside the tomograph gantry
- Measurement of the photopeak drift with increasing temperature
- Measurement of the energy and time resolution drift with increasing temperature
- Investigation of the behaviour of individual front-end detectors at temperatures below ambient in terms of dark current, energy and time resolution

All the temperature measurements have been performed with a digital thermometer (Voltcraft 304) that reads simultaneously the temperature from 4 thermocouple sensors with ± 0.1°C accuracy.

4.3.1 Investigation of the LSO-APD behaviour at temperatures above ambient

For the investigation of the front-end behaviour at temperatures above ambient, two of the sensors were placed in contact with the plastic housing of two LSO-APD detectors (front and rear layer of the same dual layer detector module) mounted on the scanner gantry. The other two sensors measured the temperature in the free space between the two 16-channel preamplifier chips that amplify the signals of each LSO-APD detector array, as shown in Figure 4.21. The preamplifier ASICs were turned on and a bias voltage was applied to the APDs. The preamplifier power dissipation initiates a temperature gradient along the length of the front-end detector. Under the presence of this gradient, temperature measurements have been performed over a period of several hours and energy spectra from a ^{18}F-FDG point source have been acquired. The position of the photopeak has been plotted versus temperature and the time resolution for all the irradiated

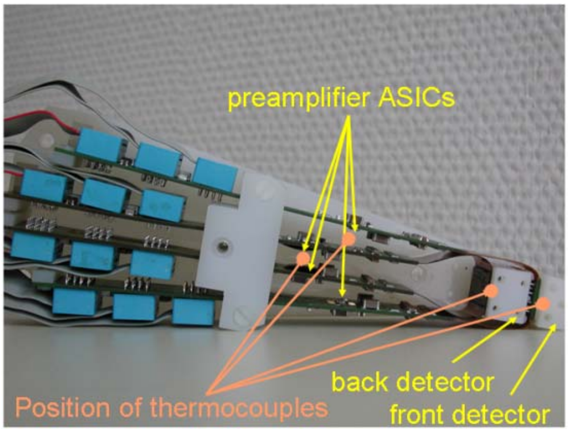

Figure 4.21: Picture of a dual layer detector module. The position of the preamplifier ASICs, which act as "heat" sources for the measurements above ambient, as well as the positions where the thermocouples were placed are indicated.

LORs has been estimated as a function of temperature above ambient. The temperature dependence of the charge sensitive preamplifier has also been investigated by feeding a test pulse of constant shape (200 mV amplitude and 2 ns rise time) directly to the chip input. All the measurements above ambient have been performed with the previous 256-channel prototype and using the previously described integrated data acquisition electronics (Sections 3.4 and 3.5).

In Figure 4.22, the temperature measured by the sensors as a function of time is plotted. It can be seen from the graph that the temperature variations in the neighbourhood of both the preamplifier and the detector block follow the same trend, even though in the first case the change is approximately 3 times larger (27.7 °C) than in the second (10.9 °C). A

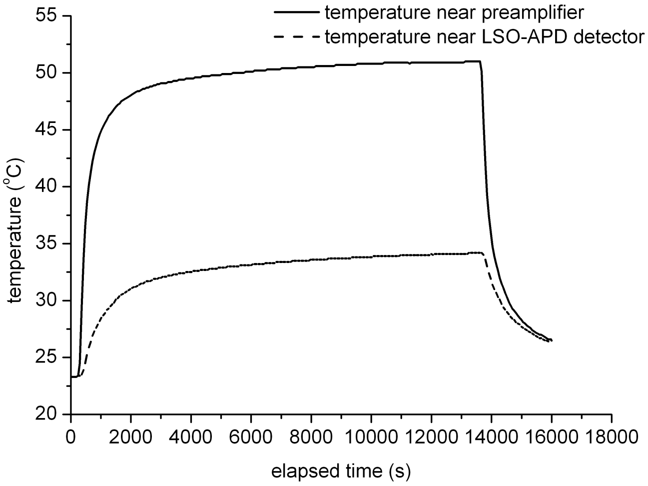

Figure 4.22: Temperature measurement between two preamplifier chips of the same LSO-APD module (top curve) and near the corresponding detector module (bottom curve) as a function of time.

separate temperature measurement has also been performed while applying bias to the APD without turning the preamplifier on. Since no temperature increase in the front-end area due to APD power consumption has been observed, it is concluded that the heat is generated by the power consumption of the preamplifier chip (30 mW per channel, 16 channels per chip) and is transferred to the detector module. As a result, a drift of the acquired energy spectra to smaller ADC channels is observed, which is depicted in Figure 4.23. The photopeak position as a function of measured LSO-APD temperature for various channels of an LSO-APD array is shown in Figure 4.24. From the graph, it can be derived that the photopeak position and thus the gain of the LSO-APD detector follows a linear relationship with temperature. A significant drift of the photopeak position has been measured for 256 detector channels having a mean value of (3.41 ± 0.07)% per degree Celsius. This value has been calculated by fitting linear curves to graphs similar to the graphs of Figure 4.24 for all 256 LSO-APD channels and calculating their slopes. The slope is then divided by the initial photopeak position. The mean R^2 value of all the performed linear fits is 0.9962 ± 0.0014.

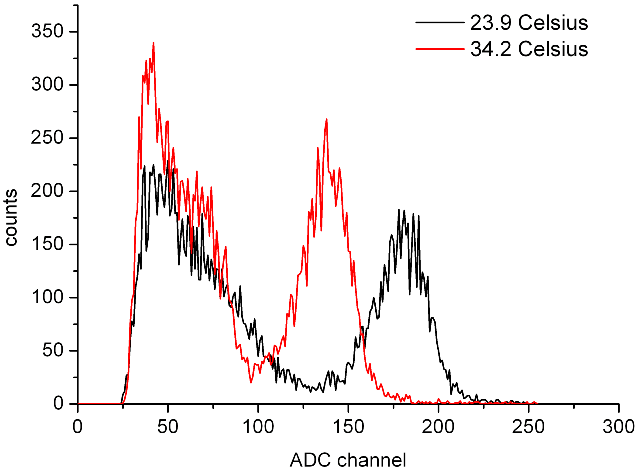

Figure 4.23: The acquired energy spectra from a single LSO-APD channel using a ^{18}F-FDG source for the highest and the lowest measured LSO-APD temperatures.

The photopeak drift can result from the combined temperature dependence of the LSO light output, the APD gain and the preamplifier gain. In order to isolate the contribution of the preamplifier, a rectangular test pulse was fed directly into each of its inputs. The preamplifier temperature dependence over time, as well as the temperature dependence of the observed position of the delta function in the acquired pulse height spectra are plotted in Figure 4.25.

For the measurements of Figure 4.25 the thermocouple was in contact with the protective cover of the preamplifier ASIC. Thus higher temperatures are measured than the temperatures presented in Figure 4.22, even though the temperature change of the LSO-APD detectors remains in the range shown in Figure 4.24. From Figure 4.25, it is obvious that the preamplifier gain is deteriorated during the first minutes of operation. This degra-

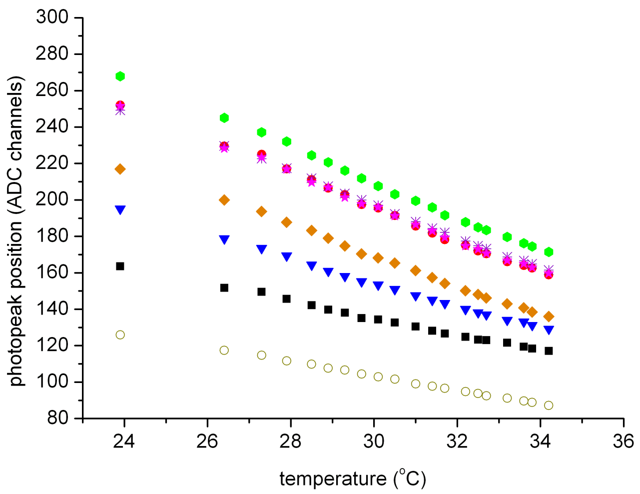

Figure 4.24: The photopeak position for various channels of an LSO-APD array as a function of temperature. All channels in the system exhibit similar behaviour to the ones shown in the graph.

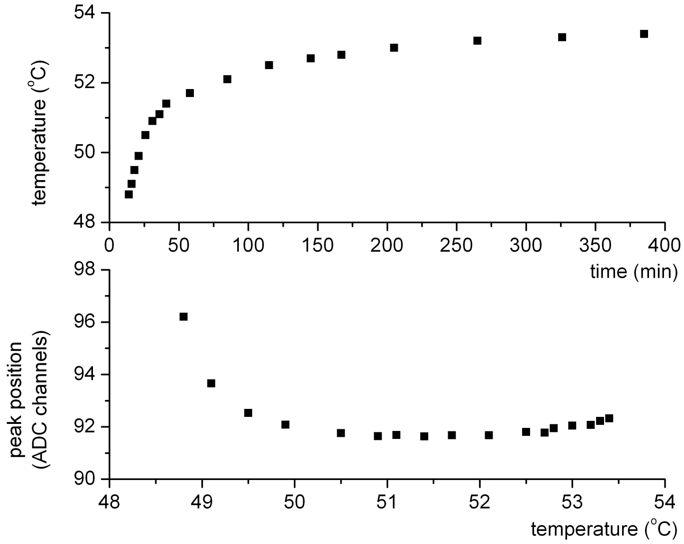

Figure 4.25: Top: temperature measured on the preamplifier ASIC as a function of time. Bottom: temperature dependence of the preamplifier gain.

dation of the preamplifier gain is approximately 4 ADC channels over the temperature range measured. Compared to the corresponding temperature dependence of the LSO-APD detectors (Figure 4.24), this change in preamplifier gain is negligible.

On the other hand, assuming linear dependence of both the APD gain and the LSO light output on temperature and taking into account that the measured photopeak is proportional to the product of the APD gain and the LSO light output, the overall temperature coefficient would be the sum of the temperature coefficients of APD and LSO (a detailed explanation is given on Appendix A). Based on the experimental results presented in [68], a maximum LSO temperature coefficient of 1.4% per degree Celsius has been estimated. We may thus attribute a 30% fraction of the measured photopeak drift due to LSO and a 70% fraction due to APD.

The mean measured energy resolution as a function of temperature is shown in Figure 4.26. The error bars are indicative of the variations on the calculated energy resolution among various detector channels of the system with respect to their mean value. Even though the mean experimental values appear to exhibit an increase up to a temperature of 30 °C and decrease at higher temperatures, no conclusion about a monotonic behaviour of the mean energy resolution with temperature can be drawn due to the large error bars. The large error introduced in the estimation of the mean energy resolution is mainly attributed to the fast temperature gradient applied to the detector modules, especially until the measured temperature reaches 30 °C (Figure 4.22). Above this temperature, the applied gradient becomes slower, hence the relatively smaller error bars (Figure 4.26).

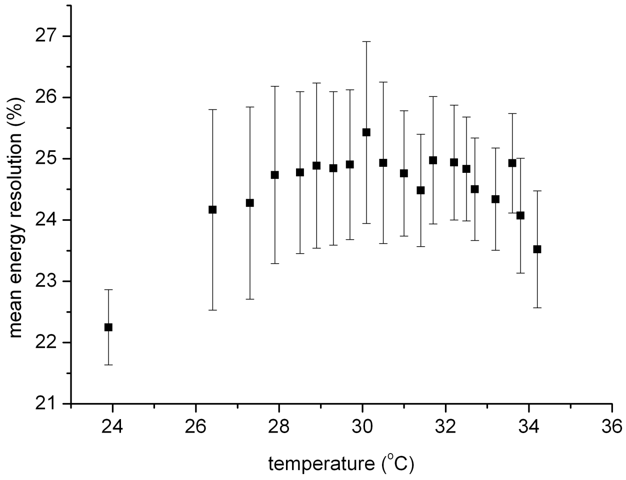

Figure 4.26: The mean energy resolution of a LSO-APD module as a function of temperature. The bias voltage of each APD was kept constant along the whole temperature range.

The dependence of the mean energy resolution on temperature may also be affected by a number of individual LSO-APD channels in the system (approximately 10% of the total number of channels that have been tested), which exhibit decreasing energy resolution with increasing temperature. The temperature dependence of one such channel is shown in the plots of Figure 4.27 which depict the photopeak position E, the photopeak FWHM and the energy resolution ($\frac{FWHM}{E}$) as a function of temperature. In Section 4.3.2, it will be shown that this behaviour is also theoretically predicted for detector channels for which multiplication noise dominates the energy resolution. These channels are characterized by large values of energy resolution in the range 26% to 30% at room temperature. This is significantly higher than the mean energy resolution of the tomograph (~23%) measured after the temperature inside the tomograph gantry has been stabilized at approximately 10 °C above ambient. For comparison, Figure 4.28 illustrates the dependence of energy resolution on temperature for an "aberrant" and a "regular" detector channel. It may be

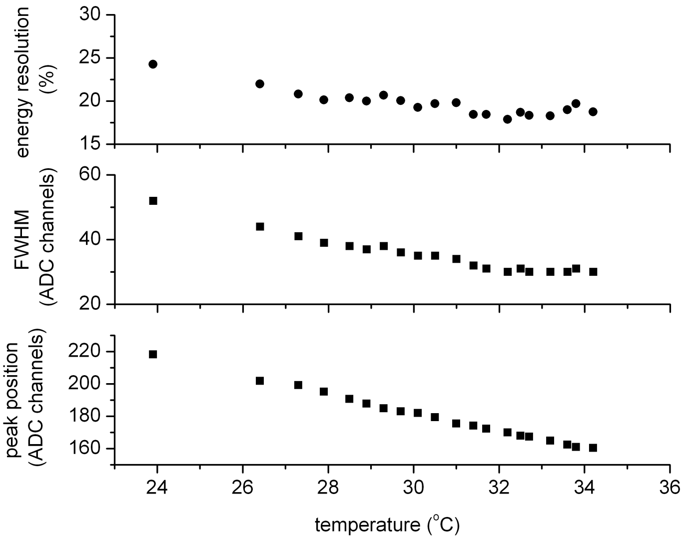

Figure 4.27: The energy resolution (top), the FWHM (middle) and the peak position (bottom) of the ^{18}F-FDG energy spectra acquired with one detector channel with "different" temperature dependence.

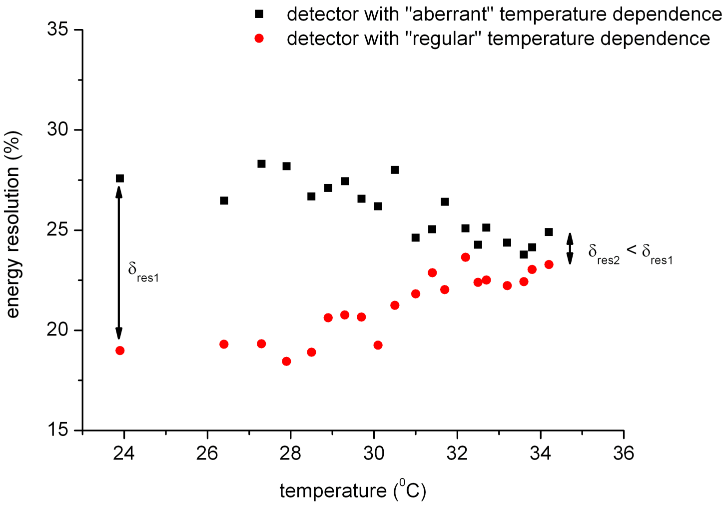

Figure 4.28: Comparative plot of the temperature dependence, in terms of energy resolution, of two detector channels that demonstrate discrepant behaviour.

observed from the graph that the deviation in the behaviour between the two detector channels is relatively large at room temperature (δ_{res1} in Figure 4.28) becoming smaller as temperature increases ($\delta_{res2} < \delta_{res1}$ in Figure 4.28).

In Figure 4.29, histograms of the distribution of energy resolution among 256 detector channels exhibit a shift of the mean from (22.1 ± 0.4)% to (22.8 ± 0.3)% and a more "Gaussian-like" distribution at higher temperatures due to the above mentioned phenomenon, namely the improvement (decrease) of energy resolution for a number of detector channels.

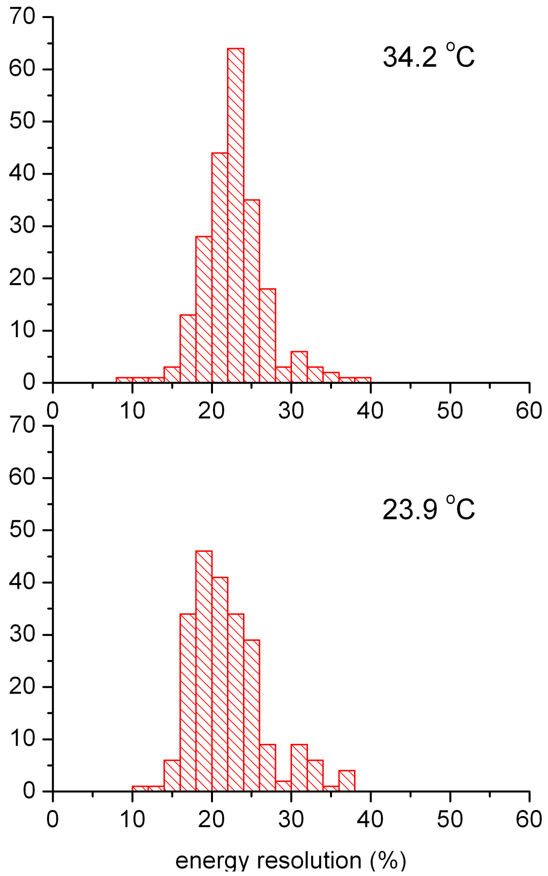

Figure 4.29: Distribution of energy resolution among 256 channels of the system for the highest (top) and the lowest (bottom) measured LSO-APD temperatures.

The estimated time resolution using a point-like ^{18}F-FDG source as a function of temperature is shown in Figure 4.30. The values depicted in this figure do not represent the system-wide time resolution since the source used in this measurement did not irradiate all possible LORs. The calculated time resolution has not been corrected for delays between electronic channels, mainly introduced by the analog signal processing electronics. As shown in Section 4.1, these delays depend strongly on the detector pulse height, therefore it is expected that with increasing temperature, the decreasing pulse height will lead to larger delays between channels and thus worsen the time resolution.

It should be emphasized that the accuracy of the results presented in the current analysis may be distorted by the apparent temperature gradients along the detector modules, as illustrated in Figure 4.22. Figure 4.31 presents a map of the behaviour of the 32 individual LSO-APD channels in the front and the rear detector array of a dual layer module in terms of photopeak shift.

No systematic variations are observed among the detector channels within the same array. However, the more significant photopeak shift (with temperature) of the rear detec-

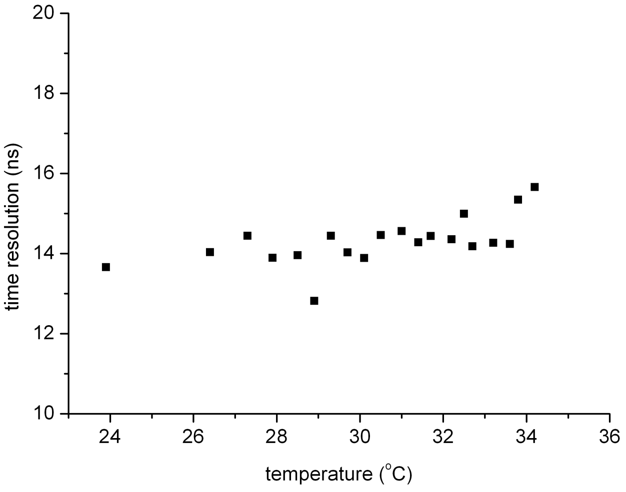

Figure 4.30: Time resolution as a function of temperature.

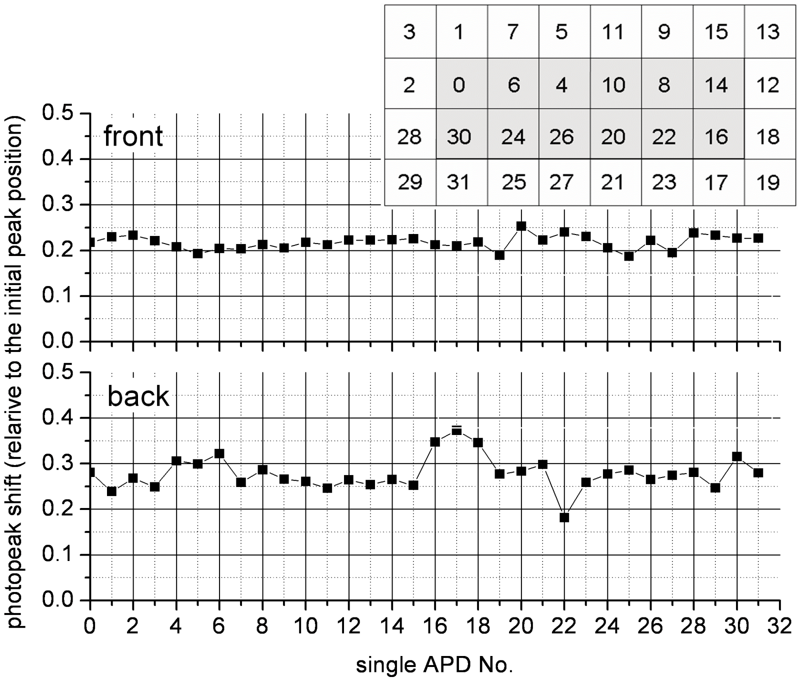

Figure 4.31: Plots of the photopeak shift (with temperature) for each of the 32 APDs in an array of a front and a rear detector. On the top right side of the graph, the numbering of the APD channels within an array is shown.

tor layer compared to the front, indicates a higher temperature gradient along the radial extent of the scanner. This is more apparent in Figure 4.32, where measurements of the photopeak shift and the temperature are shown for two detector channels of different layers, which at room temperature have approximately the same gain. In order to investigate both the temperature difference between front and rear detector layer, as well as the error introduced in the estimation of the actual detector temperature, the measurements are presented as a function of time, which, despite the fact that has no physical significance, is a variable free of any spatial dependencies.

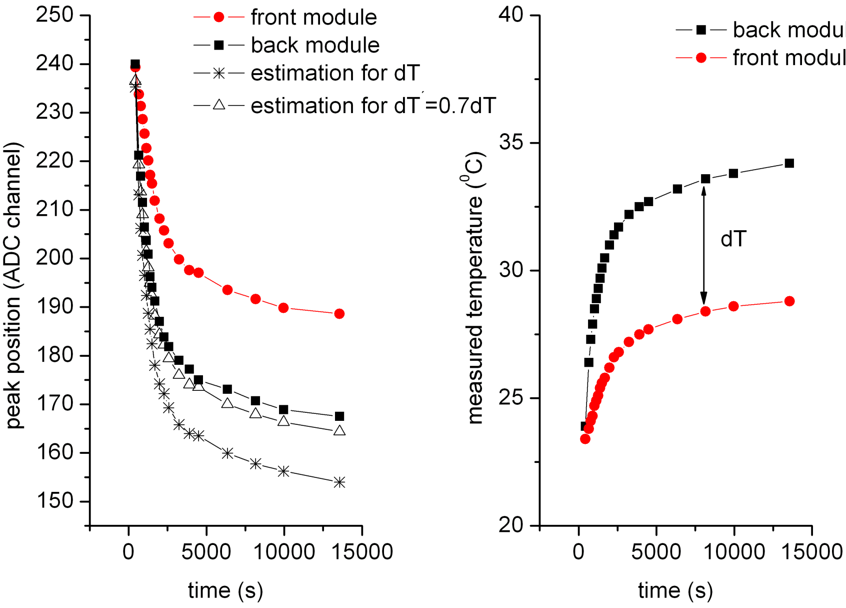

Figure 4.32: Apparent temperature gradients along the radial extent of the scanner (right) lead to significant differences in the photopeak shifts between detectors in the front and the rear layer (left).

The right graph of Figure 4.32 shows that the temperature increase measured for the front detector layer (5.4 °C) is almost half of the corresponding temperature increase for the rear layer (10.3 °C). In the dual-layer module, illustrated in Figure 4.21, the rear detector is enclosed within the front one such that it is closer to the preamplifier ASICs. The resulting temperature difference leads to a difference on the measured photopeak shift between the two layers, as demonstrated in Figure 4.31. The mean photopeak shift for 256 channels calculated above takes into account the temperature gradient between front and rear layer. In addition, Figure 4.32 demonstrates that a temperature difference of a factor 2 between the two layers leads to a factor 1.4 difference in the estimated photopeak shift. This discrepancy is mainly attributed to the deviation between the measured and the actual temperature within the detector module. In the same figure, the estimated photopeak drift for the rear layer is also plotted when taking into account the photopeak drift of the front layer, the calculated mean photopeak drift per degree Celsius and two different values for the temperature deviation between the front and the rear layer:

- a temperature difference of a factor 2 (designated as dT on the left plot of Figure 4.32), as measured from the right plot of Figure 4.32
- a temperature difference of a factor 1.4, as implied from the left plot of Figure 4.32.

In the latter case the estimated result approaches the measured curve, thus indicating the

Table 4.1: The operational characteristics of the APDs used in the measurements below ambient.

	$V_{breakdown}$	$V_{operation}$	I_{dark}	C
APD1	406 V	382 V	10 nA	12 pF
APD2	403 V	378 V	15 nA	10 pF

error in the estimation of the actual detector temperature.

4.3.2 Investigation of the LSO-APD behaviour at temperatures below ambient

The experimental setup for the measurements at temperatures below ambient consists of two 4 × 8 LSO-APD front-end detectors placed opposite to each other at a distance of approximately 40 mm. The operational characteristics of the used APDs in terms of breakdown bias, operating bias, dark current and terminal capacitance, were estimated at 25 °C and are summarized in Table 4.1 [2]. At equal distance from each detector array, a positron emitting line source (^{68}Ge) has been placed. Energy and time coincidence spectra have been acquired using a NIM multichannel analyzer (LeCroy QVt MultiChannel Analyzer (MCA), model 3001 and QVt Interface model 3157). Energy spectra acquisitions were gated using an external fast NIM pulse produced by a constant fraction discriminator (ORTEC 934 Quad CFD). For time coincidence acquisitions, the output signals of the two opposing detectors were fed to the ORTEC CFD, with one of the two NIM outputs connected to the start input of the MCA and the other connected via a delay line to the stop input of the MCA (operating in start-stop mode (t-mode)). As opposed to the measurements above ambient, the measurements below ambient were performed under stationary conditions, namely the temperature was not varying in time but was kept at a constant value for each measurement. This was achieved by adjusting the operating voltage of the cooling device to the desired value and allowing the system to stabilize at a corresponding temperature.

Each detector array was cooled using thermoelectric modules (Peltier coolers). Thermoelectric cooling has been used by other groups to compensate for much higher heat load to front-end electronics [46]. For the experiments presented in this study, two Peltier coolers of 30 mm×30 mm from AMS Technologies were chosen. In order to optimize the efficiency of the coolers, namely to maximize the heat transfer at a first stage from the object to be cooled to the Peltier cold side, then from the cold side to the hot side and finally from the hot side to the environment, the configuration illustrated in Figure 4.33 has been realized. A thin heat conductive layer was placed between the detector and the Peltier cooler. The Peltier hot side was in contact with a miniature heatsink-ventilator combination, similar to the ones used for CPU cooling in PCs. The operational characteristics of the cooling assembly are summarized in Table 4.2. In the experimental setup, the cold side of the thermoelectric cooler was in contact with the plastic housing of the front-end module.

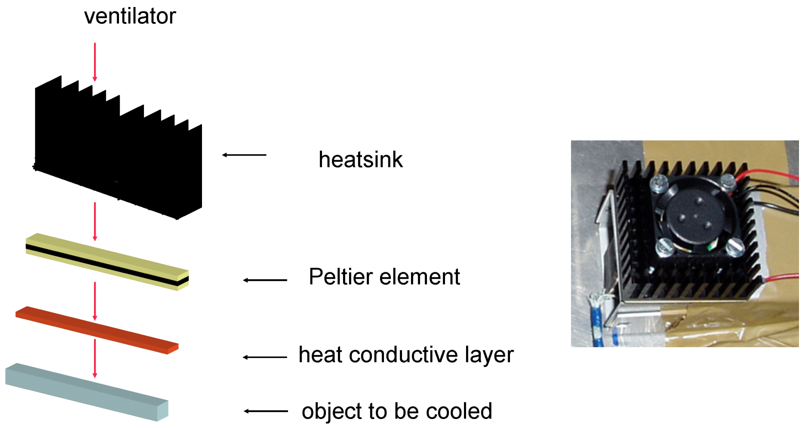

Figure 4.33: Basic structure of a thermoelectric cooler (left) and a thermoelectric cooler as implemented in a front-end module (right).

Table 4.2: The operational characteristics of the cooling assembly.

	V_{max}	I_{max}	Q_{max}	R_Q
Peltier	15.9 V	2.3 A	22.9 W	-
Heatsink/Ventilator	10 V	-	-	2.3 K/W

The thermal resistance R_Q is a critical property of the cooling assembly since it determines the temperature drop on the front-end detector caused by the Peltier coolers when pumping a specific amount of heat Q from it. A brief theoretical calculation can show the estimated efficiency of the selected Peltier cooler.

The maximum operation voltage of the Peltier cooler, as seen in Table 4.2, is 15.9 V. A general rule of thumb in the use of thermoelectric coolers is that their efficiency is maximum when operated at $\frac{2}{3}$ of their maximum operation voltage. According to the specifications of the Peltier cooler used in this study, if the voltage of operation is $V = 8$ V (and the corresponding current is $I = 1$ A), then the achieved temperature difference ΔT between the cold and the hot side of the Peltier cooler will be 50 K. The heat that has to be pumped from the hot side is approximately $Q = V \cdot I = 8$ W. In the case of the selected heatsink/ventilator combination, the thermal resistance is $R_Q = 2.3$ K/W, which means that there will be a 2.3 K temperature increase of the heatsink material for every 1 W of heat absorbed. Therefore, it is expected that the temperature of the hot side will be

$$T_{hot} = Q \cdot R_Q + T_{amb} \cong 318\ K \tag{4.6}$$

where $T_{amb} = 300$ K is the ambient temperature. In order to maximize the heat transfer between the Peltier module and the heatsink, a heat conductive layer has been added to the heatsink (Capton MT, WLFT 404, Fischer Elektronik, Germany). The layer has a thermal resistance of 0.5 K/W, consequently a temperature rise of approximately 4 K will be observed for 8 W absorbed heat. This temperature rise will be added to the calculated

T_{hot}, thus making the actual temperature on the hot side of the Peltier module approximately 22 K above ambient. Given the 50 K temperature difference between the cold and hot side of the Peltier, the achieved temperature on the cold side T_{cold} will be

$$T_{cold} = T_{hot} - \Delta T \cong 272\ K. \tag{4.7}$$

This would be true in the case of modest power consumption by the preamplifier ASICs. However in our case with 32×30 mW$\cong$ 1 W power consumption per detector array and given the fact that the 5 mm thick plastic housing of the detector has a thermal conductivity smaller than 0.05 W/(mm·K) (the amount of energy per unit time transferred through 1 mm of the material if a temperature difference of 1 K is applied along its thickness), the actual achieved temperature of the LSO-APD detector array will therefore be approximately 15 K below ambient.

The temperature drop of the two opposing LSO-APD detectors when cooled with thermoelectric coolers reaches approximately 10 °C below ambient. This value is lower, compared to the value extracted by the previous theoretical calculation, however it is the minimum value that can be achieved with the experimental setup shown in Figure 4.33. In the complete system, in order to enhance the Peltier coolers' efficiency, water cooling is used instead. Thus, the Peltier coolers can compensate for both the temperature increase due to the preamplifier power consumption and for the temperature drop below ambient.

The current I drawn by the two opposing LSO-APD detectors as a function of reciprocal temperature and APD bias voltage is shown in Figure 4.34. This current represents the sum of the mean photocurrent I_{ph} induced in the APDs and the dark current.

$$I = (I_B + I_{ph} + I_{th}) \cdot M + I_S \tag{4.8}$$

where M is the APD gain, I_B is the bulk leakage current due to diffusion of minority carriers within the depletion region of the avalanche photodiode, I_{th} is the bulk leakage current due to thermal generation of electron-hole pairs within the depletion region and I_S is the surface leakage current created due to large voltage gradients in the p-n junction interface.

From the equation, it is evident that since the bulk leakage current (minority carriers and thermal, $I_B + I_{th}$) is created inside the depletion region, it will be subjected to avalanche multiplication. The APD current is dependent on both the APD gain M, namely APD bias voltage V, and the temperature T. As seen in Section 4.3.1, the gain M is also temperature dependent. Assuming that the APD gain has a linear temperature dependence (Figure 4.24), the following expression can be derived for the combined dependency of M on both V and T:

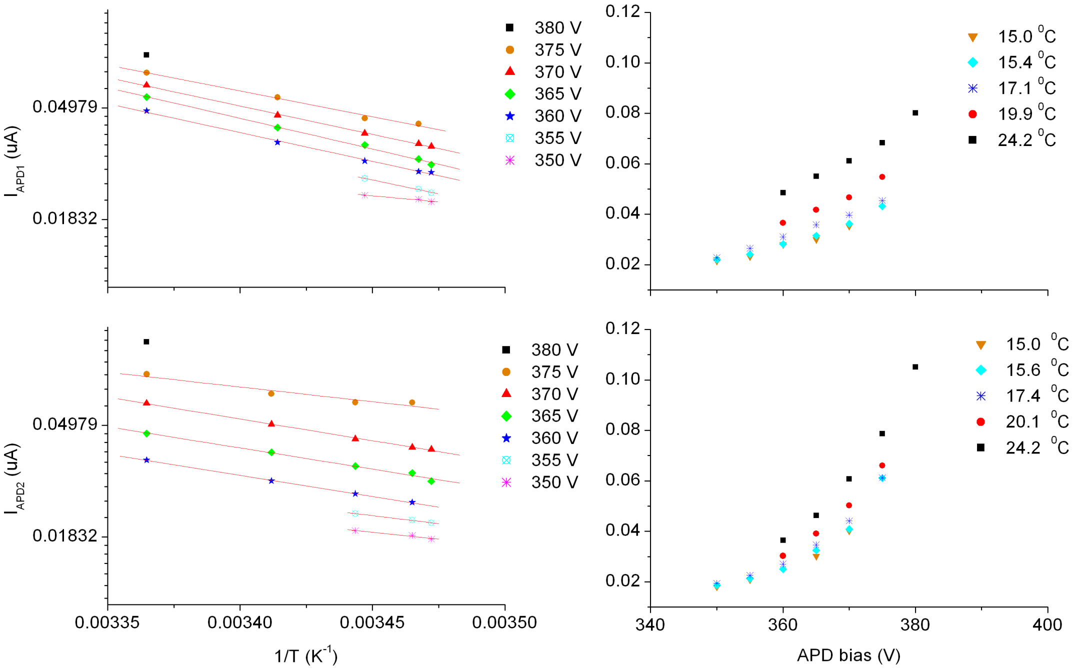

Figure 4.34: The current (dark current plus photocurrent) drawn by the two opposing detectors as a function of temperature (left) and APD bias (right).

$$M = M_0(V) \cdot (1 - \alpha \cdot (T - T_0)) \tag{4.9}$$

where α is the gain temperature coefficient as extracted in Section 4.3.1 and $M_0(V)$ is the APD gain at room temperature which depends only on the APD bias voltage. It should be mentioned that Equation 4.9 is expected to be valid for a wide temperature range provided that the difference between the operating and the breakdown voltage is sufficiently large in order to operate in the linear part of the APD characteristic. As will be seen later on in this section, at low temperatures, linearity may be disturbed and the temperature coefficient may change with temperature.

The detailed expression of the thermal leakage current I_{th} is given by the following equation [98]

$$I_{th} \propto F\left(T^{\frac{3}{2}}\right) \cdot \left(e^{\frac{-E_g}{2kT}}\right) \tag{4.10}$$

where E_g is the energy band gap of the specific semiconductor, namely 1.12 eV in the case of Silicon and k is the Boltzmann constant. The term having a $T^{\frac{3}{2}}$ dependence on temperature may be omitted since the exponential term is the dominant one. The diffusion current I_B is also temperature dependent [98], however in the case of Si diodes, it is generally considered small compared to I_{th} and for simplicity its temperature dependence will not be considered in the current analysis. Substituting the expressions for the gain and for the thermal current to Equation 4.8, the following expression for the temperature dependence of the APD current is obtained:

$$\begin{aligned} I \propto I_S + M_0 \cdot \left(I_{ph} + I_B\right) \cdot (1 + \alpha T_0) \\ -\alpha \cdot M_0 \cdot \left(I_{ph} + I_B\right) \cdot T + M_0 \cdot (1 + \alpha \cdot (T_0 - T)) \cdot e^{-\frac{E_g}{2kT}} \end{aligned} \tag{4.11}$$

In the above equation, the exponential $e^{-\frac{E_g}{2kT}}$ dependence dominates over the linear T dependence. The temperature dependence of the photocurrent I_{ph} due to the LSO temperature coefficient will contribute to the linear term of Equation 4.11, thus it may be disregarded. In Figure 4.34, the y-scale of the two plots on the left side is logarithmic and linear fits are applied to the measured data. The derived R^2 values are plotted versus the APD bias voltage in Figure 4.35. It can be observed that linearity is disturbed in the lower limits of the APD bias at which, for both APDs, the gain is significantly deteriorated, as well as in the higher limit for the APD which is closer to breakdown (bottom left plot of Figure 4.34). In addition, the current of the first APD reproduces fully the theoretical $e^{-\frac{E_g}{2kT}}$ behaviour, namely it changes at approximately a factor of 2 for a temperature change of 10 K. The same does not apply in the case of the second APD for which the same temperature change results in a current change of a factor 1.5. However, it is obvious that for both APDs decreasing the temperature and the APD bias leads to a decrease in the dark current, as predicted by the theory [98].

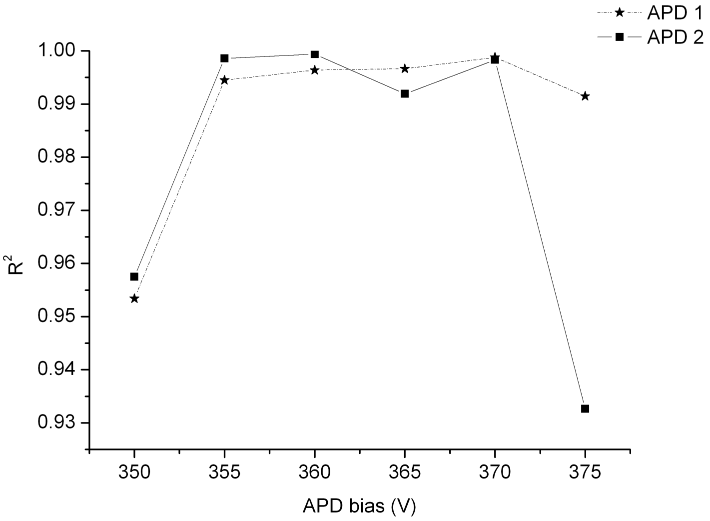

Figure 4.35: Plot of the Pearson correlation coefficients describing the linear fits of Figure 4.34 (left) versus APD bias for the two APDs studied.

All the above mentioned currents contribute to the estimated energy resolution $\frac{\Delta E}{E}$ as seen by the following model [41, 66, 67, 47]

$$\left(\frac{\Delta E}{E}\right)^2 = \left(2.35 \cdot \frac{\sqrt{F_{scint}}}{\sqrt{N_{opt}}}\right)^2 + (R_{int})^2 + \left(2.35 \cdot \frac{\sqrt{F_{APD}}}{\sqrt{N_{e-h}}}\right)^2 + \left(2.35 \cdot \frac{\sigma_{noise}}{N_{e-h}}\right)^2 \tag{4.12}$$

where $\left(2.35 \cdot \frac{\sqrt{F_{scint}}}{\sqrt{N_{opt}}}\right)$ is the scintillation crystal energy resolution related to the divergence from Poisson statistics in the number of the produced optical photons N_{opt} (as represented by the excess factor F_{scint}) and R_{int} is the energy resolution due to crystal inhomogeneities. The excess noise factor F_{APD} represents statistical fluctuations in the number of the produced electron-hole pairs, N_{e-h}, during avalanche multiplication [58, 98] and thus in the APD gain. The rms electronic noise imposed on the APD signal is σ_{noise} [5]. Every component in expression 4.12 depends in a direct or indirect way on the temperature:

- The contribution of the scintillation crystal to the measured energy resolution, represented by the sum between the first two terms in Equation 4.12, has been estimated experimentally in previous studies. In the case of LSO, it varies in the range of 6 to 10% at normal experimental conditions, namely for a constant number of produced optical photons N_{opt} at room temperature [66, 4]. In [68], a number of LSO samples with different Cerium concentrations has been investigated and for the majority of the samples, a linear decrease of the light output with increasing temperature within the temperature range of interest for this study has been found. Based on the formula and the results suggested in [68], a temperature coefficient of the LSO light output (N_{opt}) of 1% per degree Celsius around room temperature is assumed. It has to be mentioned that the above value is only an approximation since the Cerium concentration of the LSO crystals used in this study is not known.

- The contribution of the APD to the energy resolution due to statistical multiplication noise $\left(2.35 \cdot \frac{\sqrt{F_{APD}}}{\sqrt{N_{e-h}}}\right)$ is strongly dependent on gain M, through the excess noise factor F_{APD} [58], and thus on temperature T as seen from Equation 4.9. The dependence of F_{APD} on M is given by Equation 4.13 [98], where k is the ratio of hole to electron ionization rates and is equal to 0.024 in the case of the S8550 APDs from Hamamatsu.

$$F_{APD} = k \cdot M + (1-k) \cdot \left(2 - \frac{1}{M}\right) \tag{4.13}$$

- The electronic noise contribution $\left(2.35 \cdot \frac{\sigma_{noise}}{N_{e-h}}\right)$ depends on the APD and the subsequent electronics such as the preamplifier and the shaper. The quantity σ_{noise} is directly related to the Equivalent Noise Charge (ENC) which depends strongly on the overall current (Equation 4.8) and the thermal noise induced in the equivalent

> series resistance R_{eq} introduced by the APD junction, the load resistance and the input resistance of the amplifier [31, 81]. Thus, the temperature dependence of noise contribution may be approximated by the following equation:
>
> $$\sigma_{noise} = \frac{A \cdot \sqrt{T}}{M} \tag{4.14}$$
>
> where the coefficient A may be estimated from the measured noise slope of the front end. For a 50 ns shaping constant, a noise slope of 25 e^{-}/pF and an rms noise of approximately 700 e^{-}, at room temperature, for a 10 pF detector capacitance has been shown in [75]. The number of primary electron-hole pairs N_{e-h} for 511 keV incident radiation and 70% APD quantum efficiency at 420 nm has been estimated to 2000 given the light losses of approximately 80% at the crystal surface and at the interface between the crystal and the APD.

An example of the contribution to the energy resolution of each one of the above mentioned factors is plotted in Figure 4.36. The plots are shown as a function of temperature and for different crystal intrinsic resolutions at room temperature covering the above mentioned 6% to 10% range. An APD gain of 50 at room temperature (M_0 in Equation 4.9) and a temperature coefficient of 4% per degree Celsius for both the scintillator and the APD are assumed. In order to avoid singularities, the linear dependencies of the scintillator light output and the APD gain have been approximated by the closest exponential function [3].

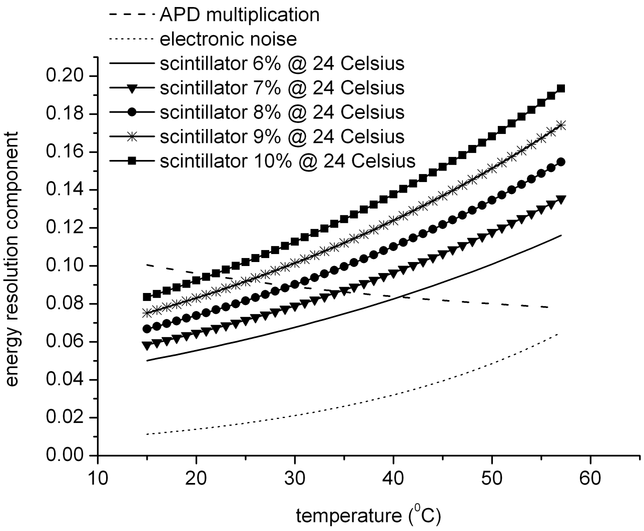

Figure 4.36: Dependence of the energy resolution on temperature as predicted by Equation 4.12.

From Figure 4.36, it can be observed that the contributions of the scintillator and the APD multiplication are competing depending on the temperature, while the contribution of electronic noise remains less significant for a wide temperature range. In the case that the contribution due to APD multiplication is the predominant one, a decreasing overall energy resolution with increasing temperature may be observed. This behaviour has been experimentally confirmed from the results of Figure 4.27.

Figure 4.37 shows the measured temperature dependence of the photopeak position and energy resolution for various APD bias voltages and at temperatures below ambient. Since the APD breakdown voltage decreases with decreasing temperature, the measurements presented in this figure were performed only at those temperatures and APD bias values that neither lead to saturation of the preamplifier due to high input charge nor to distorted pulse height spectra due to low gain. The left graph of Figure 4.37 shows that the linear trend demonstrated in the corresponding graph for temperatures above ambient (Figure 4.24) is, in this case, distorted for low temperatures. It is assumed that this discrepancy arises at low temperatures when the breakdown voltage is shifted to lower values, causing the difference between the operating and the breakdown voltage to become smaller, and therefore the APD is operated near the steep slope of its characteristic curve, where non-linear behaviour is expected.

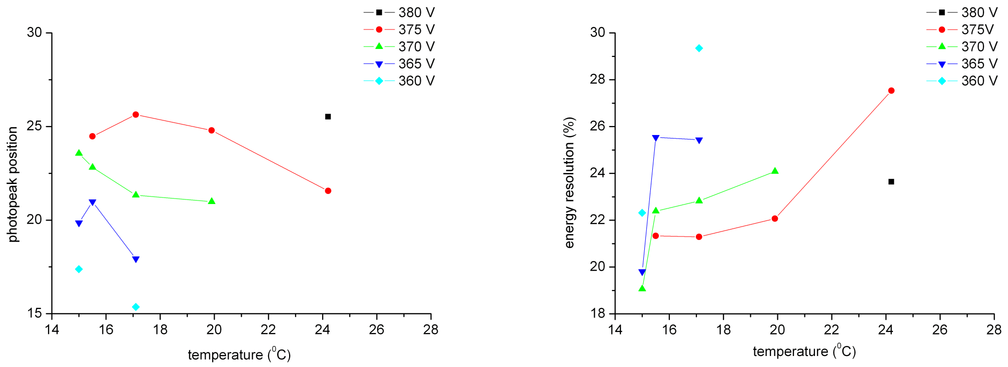

Figure 4.37: Photopeak position (left) and energy resolution (right) as a function of temperature.

According to the findings of Figure 4.37, the optimum values of APD bias and temperature that result in the lowest energy resolution (for the specific APD-LSO channel) are 370 V and 15 °C, respectively. Thus, temperature tuning of the front-end modules necessitates a simultaneous APD bias tuning for the achievement of an optimum, non-degraded energy resolution [19].

It should be noted that the above methodology applied to a single detector channel is an example which demonstrates the difficulties posed if the same methodology is applied to every individual detector of a scanner with a large number of detectors, such as MADPET-II. The detector tuning in this scanner in terms of APD bias and temperature is multiplexed, since the APD bias is not applied on every individual detector, but on every monolithic 2x8 array and the cooling system is able to regulate and maintain the temperature for every group of three dual layer 4x8 detector arrays. Therefore, the individual detector tuning becomes rather impossible. Given the random variations on detector performance even among detectors of the same array [56, 73], it may be concluded that an optimum operation point in terms of bias and temperature does not exist.

The time coincidence histogram between two opposing LSO-APD channels at the optimum APD bias voltage (370 V) and for two different temperatures (room temperature 24 °C and optimum 15 °C) is depicted in Figure 4.38. The time resolution was calculated from the FWHM of the corresponding Gaussian fits. The temperature effect is minor, and is expected not to affect the timing performance of the tomograph especially given the considerably poorer performance of the analog signal processing electronics in terms of walk and jitter, that results in a system-wide time resolution of the order 10 ns (see Section 4.1.2). For comparison, the achieved time resolution at a bias of 380 V (recommended operating voltage by the manufacturer) and at room temperature is in the order of 3.5-4 ns. The significant degradation of the time resolution may be due to the decrease in the achieved gain during the simultaneous tuning of temperature and APD bias, if the temperature dependence of the temperature coefficient at low temperatures is not taken into account, as illustrated in Figure 4.39.

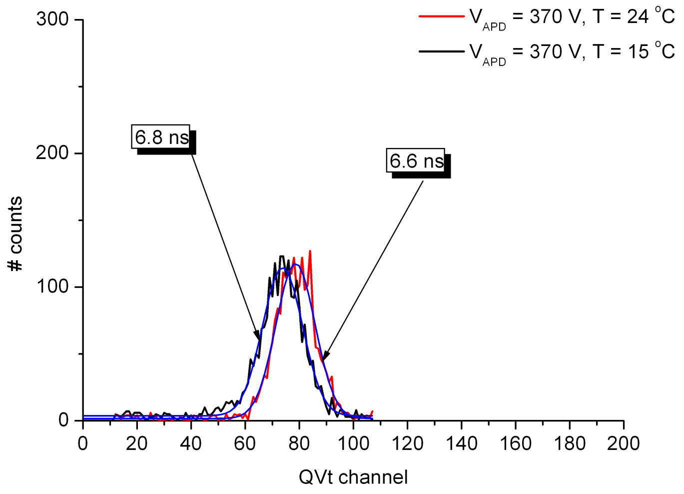

Figure 4.38: Time resolution as a function of temperature at an APD bias of 370 V.

- According to Figure 4.39, if initially, the APD is operated at bias V_2, a gain M_2 at temperature T_2 is achieved. If the temperature is lowered at a value T_1, but the gain is to be maintained at the same value M_2, in order to avoid being close to breakdown, the bias needs to be lowered at a value V_1, provided that the temperature coefficient of the breakdown voltage remains constant with temperature (left-hand graph). In that case, the difference in time resolution achieved at temperatures T_1 and T_2 (when operating the APD at V_1 bias) is related to the difference between the gains M_1 and M_2.

- If the temperature coefficient does not remain constant with temperature, then the bias of the APD should be V'_1 in order to maintain the gain at value M_2 (right-hand graph). In that case, the difference in time resolution achieved at temperatures T_1 and T_2 (when operating the APD at V'_1 bias) is related to the difference between the

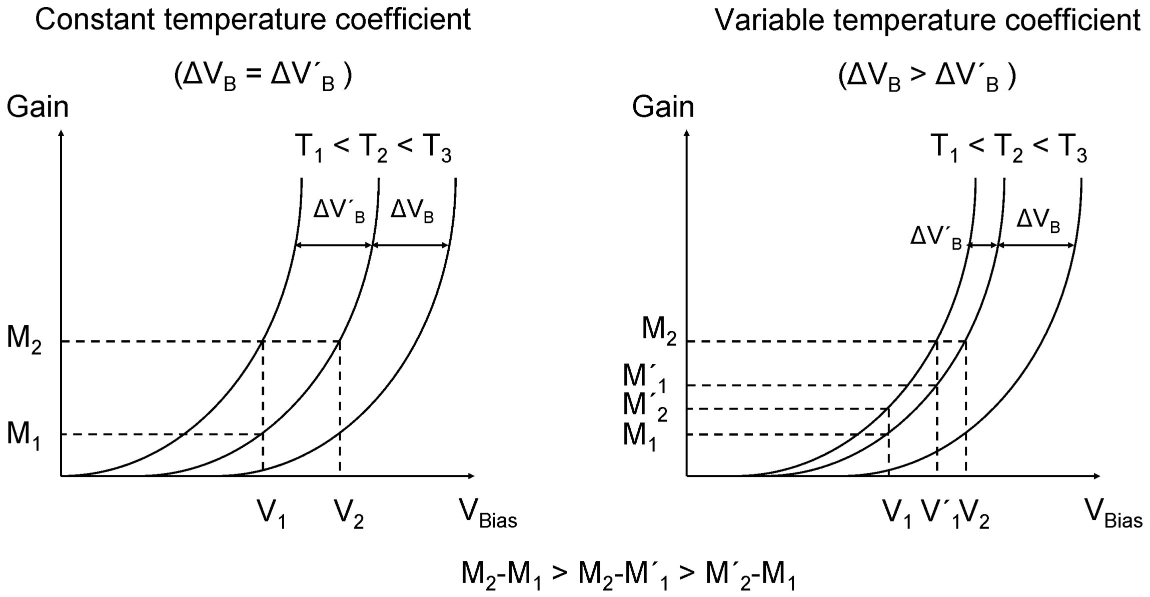

Figure 4.39: The effect of temperature dependence of the breakdown voltage temperature coefficient on the achieved gain.

gains M'_1 and M_2, which is smaller than the difference between the gains M_1 and M_2.

- In reality what happens is something between the two situations mentioned above: according to the manufacturer's specifications about the S8550 APD, the temperature coefficient of the breakdown voltage is 0.78 $\frac{V}{^0C}$, namely for a temperature difference of approximately 10 ^{0}C, the breakdown voltage decreases to approximately 8 V. The APDs used in coincidence in this study, have a breakdown voltage of 403 V and a recommended operating voltage of 378 V, meaning a difference of 25 V between breakdown and operation point. When reducing the temperature by 10 ^{0}C and assuming a constant temperature coefficient, the breakdown voltage will decrease to 395 V. If the gain is to be kept constant, the APDs should be operated at 25 V below breakdown, namely at 370 V, according to the right-hand graph. However, if the temperature coefficient is not constant, but decreases with decreasing temperature, then the achievable gain at the same operating voltage (370 V) would be lower and so would be the difference between the achievable gains (M'_2-M_1) at temperatures 24 and 15 ^{0}C.

4.4 Detector efficiency uniformity

In Section 2.1.5, the necessity for correction of variations in the detector efficiencies has been addressed. These differences are indeed evident in the case of MADPET-II, as shown in Figure 4.40. An example of the effect of differences on detector geometry is illustrated on the left graph of this figure, where the number of detected singles counts from each detector as a function of detector channel is plotted. For this measurement the detectors

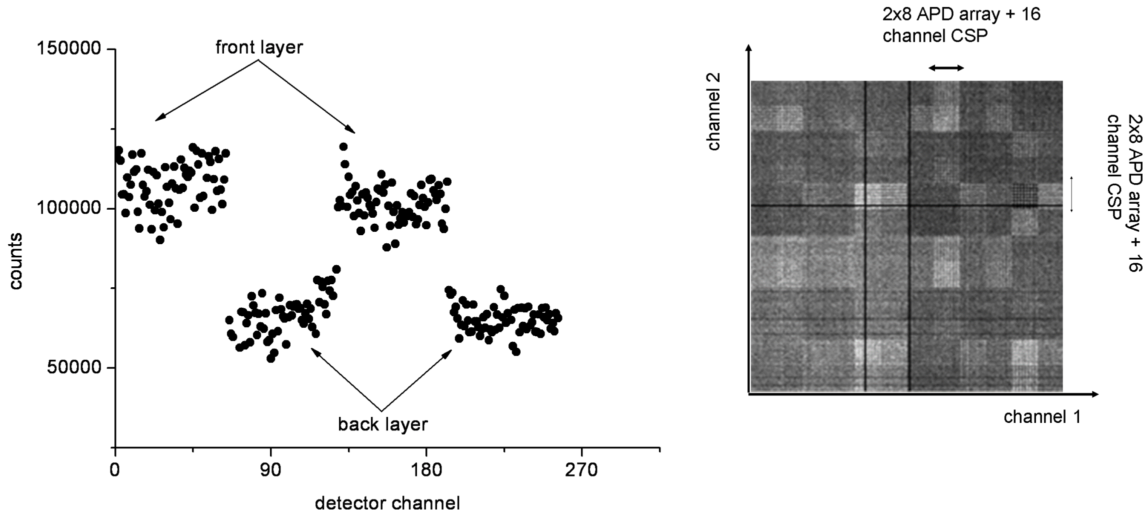

Figure 4.40: Left: number of detected singles counts as a function of channel number. Differences between detectors which belong to the front and to the rear layer are clearly visible. Right: a 384 × 384 coincidence sensitivity histogram indicative of the effect of detector gain on measured efficiencies.

were irradiated with a point-like ^{18}F-FDG source placed at the center of the FOV. The data are grouped into two separate regions corresponding to the front and to the rear detector layer. Thus, the rear detector layer always detects significantly less number of events within a given time frame since it is screened by the front layer. A mean efficiency for the rear detector layer which is approximately 60% of the front detector layer efficiency may be extracted from the data of Figure 4.40. This value is in good agreement with the expected value given the different crystal thicknesses and the solid angle coverage for the two detector layers as illustrated in Figure 4.41.

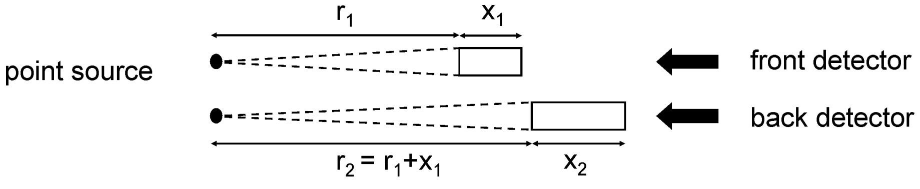

Figure 4.41: Illustration of the solid angle coverage by a point source placed at the center of the FOV when irradiating the front and the rear detector of a dual layer detector module.

Given a linear attenuation coefficient μ of 0.09 mm^{-1} for 511 keV gamma rays at LSO [59], the ratio of detected singles by the rear layer, I_{rear} to the detected singles by the front layer I_{front} is given by the equation:

$$\frac{I_{rear}}{I_{front}} = \frac{\left(e^{-\mu\cdot x_1} - e^{-\mu\cdot(x_1+x_2)}\right)\cdot r_1^2}{\left(1-e^{-\mu\cdot x_1}\right)\cdot r_2^2} = 53\% \tag{4.15}$$

The effect of detector gain on sensitivity is illustrated on the right plot of Figure 4.40. The detectors in the corresponding measurement were uniformly irradiated with a flood ^{18}F-

FDG source placed at the center of the FOV. The plot depicts a 384 × 384 intensity array of the detected coincidences along every LOR, as defined by Equation 3.3. A significant pattern may be observed for every 16 detector channels, namely for every monolithic 2 × 8 APD array read out by a 16-channel preamplifier ASIC which are characterized by relatively uniform gain.

The effect of intrinsic detector efficiency appears as a rather random fluctuation in both plots of Figure 4.40 and is mostly attributed to variations of the crystal non-uniformities for different crystal pixels.

4.5 Extraction of DOI information and the effect on reconstructed spatial resolution

As emphasized in Section 3.2.2, MADPET-II is able to provide DOI information by means of a dual radial detector layer. The DOI capability of the tomograph has been evaluated at an early stage of its construction with six dual layer detector modules, as illustrated in Figure 4.42. A mechanical structure (phantom) consisting of ten glass capillaries filled with ^{18}F-FDG, extending along both the axial and radial FOV has been imaged. The capillaries have an inner diameter of 0.25 mm and a pitch of 4.25 mm. Thus the phantom extends along the complete FOV that can be covered by the six detector modules (approximately 40 mm).

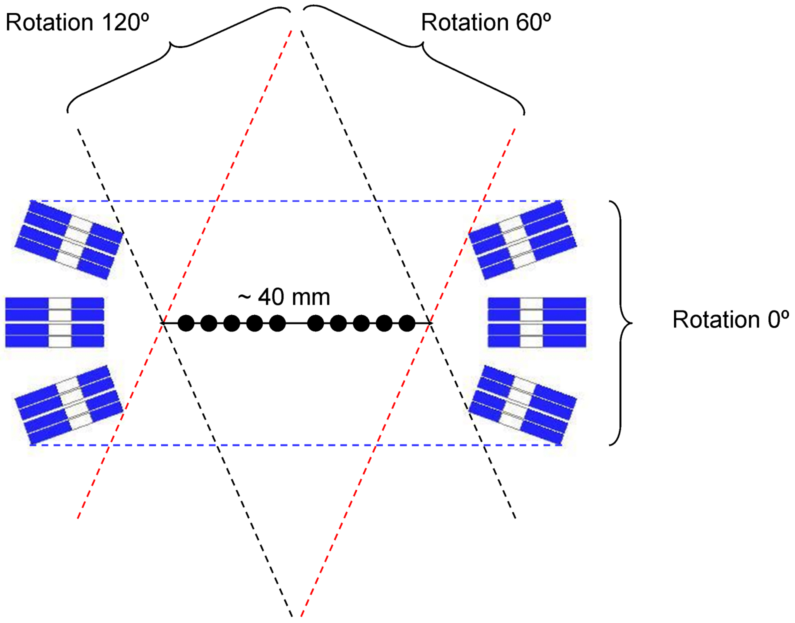

Figure 4.42: Experimental setup for the evaluation of the DOI capability of MADPET-II.

For the image reconstruction, the phantom was rotated in three steps of 60° each. A lower energy threshold of 400 keV and a time coincidence window of 20 ns has been applied to the coincidence sorting process. The acquired data were reconstructed in two different ways:

- Using a system matrix that models the dual radial detector geometry of the tomograph
- Using an alternative system matrix that sums the counts of the front and the rear detector layers, assuming thus a single detector layer of thickness approximately equal to the sum of the thicknesses of the two individual layers, namely 14 mm.

Figure 4.43 shows the reconstructed images after 30 iterations obtained with the two above mentioned ways. In the latter case (no DOI included), strong artifacts are introduced in the reconstructed image and the capillaries at the edges of the FOV are hardly resolved. On the contrary, the reconstructed images that take into account the dual detector layer demonstrate that the system is able to provide DOI information and thus compensate for the parallax error described in Section 2.1.4. The effect of DOI information on spatial resolution can be quantified by calculating the FWHM of the line profiles of the 10 capillaries shown in Figure 4.44. For simplicity, a 1 mm (FWHM) Gaussian smoothing filter has been applied to the line profiles in order to better distinguish the profiles of the edge capillaries. For the calculation of the FWHMs, Gaussian fits have been applied

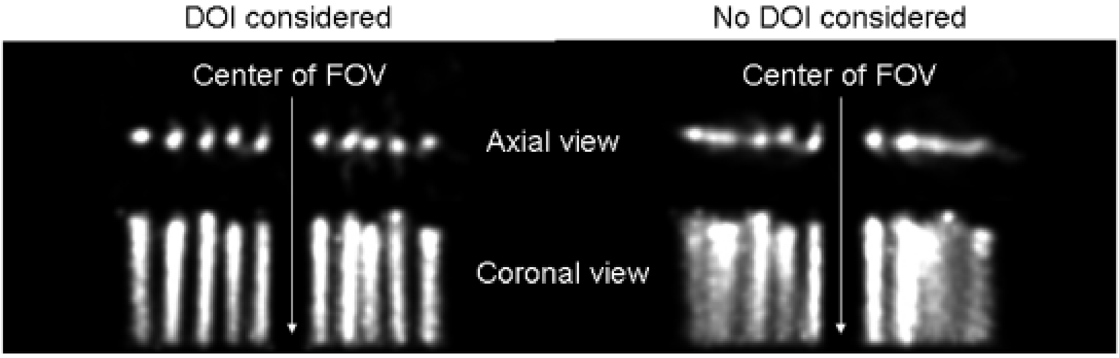

Figure 4.43: Reconstructed images of 10 capillaries extending along the FOV with (left) and without (right) DOI information.

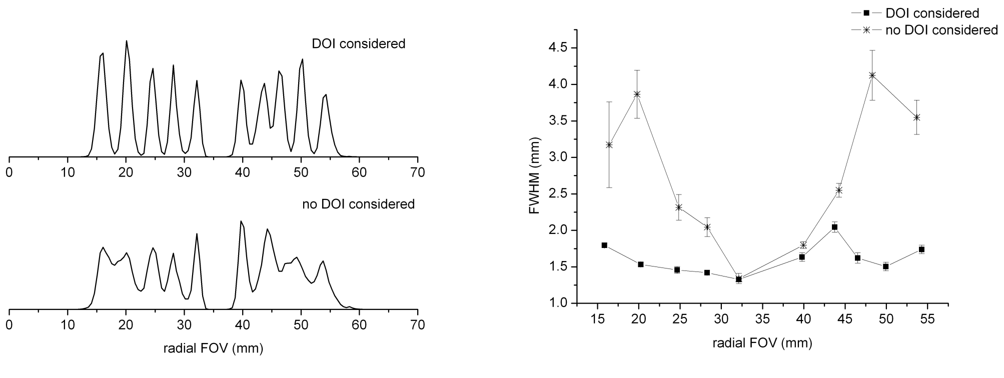

Figure 4.44: Dependence of spatial resolution on the object radial position within the FOV: line profiles of the activity distribution in the 10 imaged capillaries (left) and the calculated FWHM as a function of position within the FOV (right) are shown.

to the profiles and the extracted values have been corrected for the Gaussian smoothing filter. In the case where the DOI information is included in the system matrix, a mean FWHM of 1.3 mm has been calculated for the central capillaries and 1.8 mm for the edge indicating a resolution degradation of approximately 40% at the edges of the FOV compared to the center. In the case where the DOI information is not included in the system matrix, the degradation at the edges is severe resulting in an inaccurate estimation of the FWHM, as indicated by the large error bars.

The right graph of Figure 4.44 shows the dependence of the calculated spatial resolution on the radial position of the object for the two cases. The V-sized trend observed in the plot is similar to the trend followed by the theoretical dependence of the TOR width x as a function of the TOR obliqueness θ and the crystal thickness l shown in Figure 4.45. The left schematic of Figure 4.45 demonstrates an increasing TOR width x with increasing obliqueness θ of the detector pair (compared to the case x = d when $\theta = 0^{\circ}$) according to the following equation:

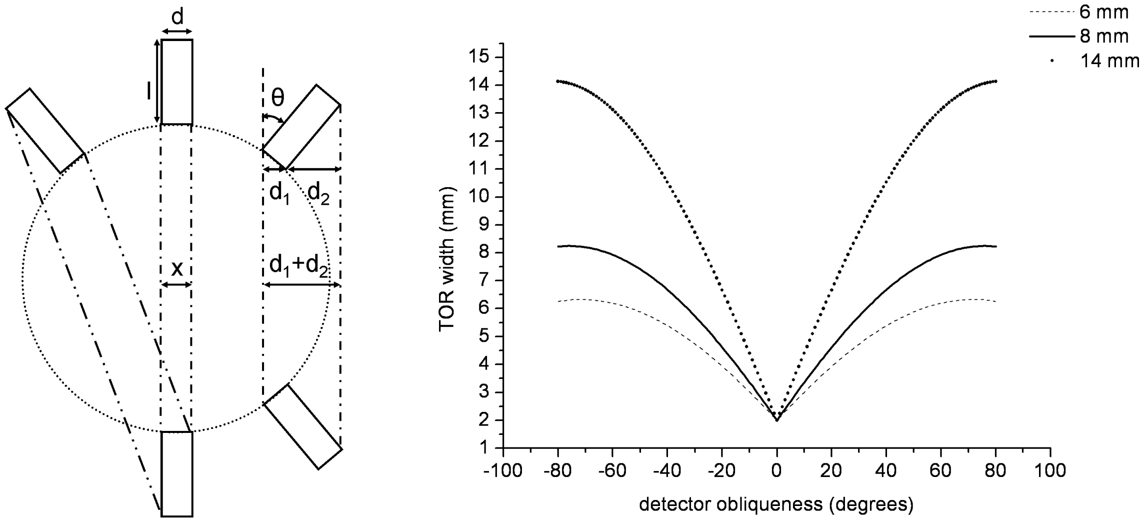

Figure 4.45: Left: illustration of the TOR broadening (dashed lines) for oblique detector pairs, also described in Section 2.1.4 (Figure 2.5). Right: dependence of the TOR width on detector obliqueness θ for a crystal thickness l=6, 8, 14 mm.

$$x = d_1 + d_2 = d \cdot |cos(\theta)| + l \cdot |sin(\theta)| \tag{4.16}$$

It should be noted that a quantitative comparison between the plots of Figures 4.44 and 4.45 is difficult, given the fact that the reconstructed spatial resolution is also affected by the system matrix used, namely the theoretical model of the tomograph which in the case of MADPET-II is extracted by Monte Carlo simulations, as well as by the reconstruction algorithm used.

4.6 Sensitivity compensation

As already emphasized, a key feature in MADPET-II hardware design is the dual radial crystal layer which allows for extraction of depth of interaction information. At the same time, the rear layer compensates for sensitivity, which would otherwise be hindered by the use of short crystals. In Figure 4.46, the relative sensitivity, in terms of number of detected coincidences normalized to the maximum number observed, is plotted as a function of lower energy threshold for two cases:

- for allowed coincidences only between detectors of the front layer and
- for allowed coincidences between any two detectors from either layer.

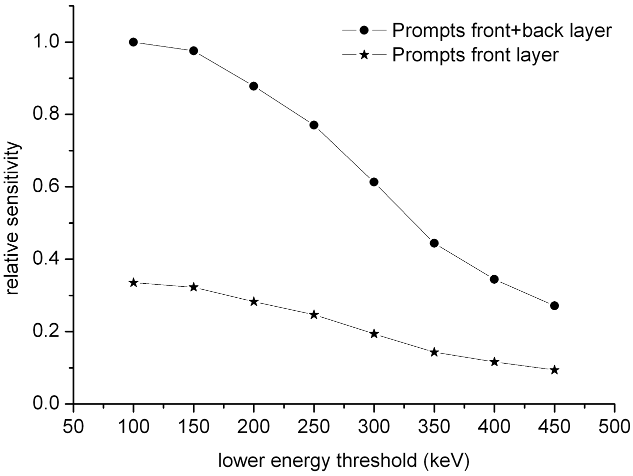

Figure 4.46: Dependence of sensitivity on the lower energy threshold when recording coincidences between detectors of the front layer only (stars) and between detectors of both layers (circles).

For the measurements presented in Figure 4.46, 6 detector modules, arranged as shown in Figure 4.42, were irradiated with a planar ^{18}F-FDG source of 1 mm thickness extending along the complete axial FOV. The thickness of the source was chosen as small as possible in order to minimize variations in the LOR sensitivity due to different amount of radioactivity "seen" by each LOR. Coincidences were detected between opposing detectors

It is obvious from the graph that the rear detector layer is able to enhance the system's sensitivity to approximately 70% and this enhancement is maintained for all lower energy thresholds. This result may be theoretically confirmed when assuming that the LOR efficiency is the product of the detector efficiencies ϵ. Under this assumption the ratio N of the sensitivity obtained when taking into account coincidences between detectors of the front layer to the sensitivity obtained when taking into account coincidences between detectors from both the front and the rear layer is given by the following equation:

$$N = \frac{\epsilon_{front} \cdot \epsilon_{front}}{\epsilon_{front} \cdot \epsilon_{front} + 2 \cdot \epsilon_{front} \cdot \epsilon_{rear} + \epsilon_{rear} \cdot \epsilon_{rear}} \cong 0.4 \tag{4.17}$$

where

$$\epsilon_{rear} \cong 0.6 \cdot \epsilon_{front} \tag{4.18}$$

as estimated in Section 4.4. In addition, simulation results have shown that a further improvement on sensitivity of approximately 30% is to be expected for low energy thresholds if intercrystal scatter events are properly identified and included [83].

4.7 Mouse cardiac imaging

A first assessment of the system's capability for in vitro animal imaging has been realized. A normal mouse was injected with approximately 10 MBq $^{18}F - FDG$ and images of the heart were acquired at first with a commercial small animal PET scanner (MicroPET Focus, CTI-Siemens) and at a later time point with MADPET-II. The transaxial, coronal and sagittal views of the reconstructed images are shown in Figure 4.47.

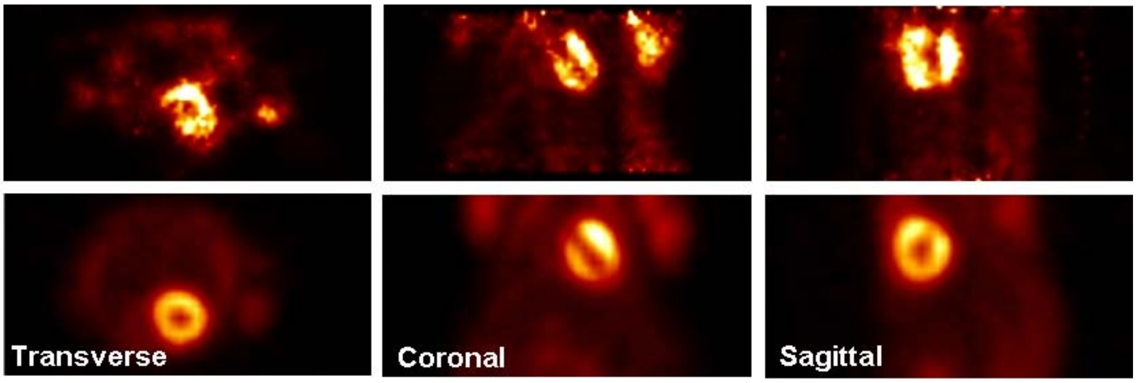

Figure 4.47: Transaxial, coronal and sagittal view of ^{18}F-FDG concentration in a mouse heart imaged with MADPET-II (top row). For comparison, the bottom row shows the same part of the body acquired with a commercial, state-of-the-art small animal PET scanner.

The acquired images from MADPET-II were reconstructed using the MLEM algorithm (20 iterations) at a 400-700 keV energy window and a 80 ns time coincidence window. No correction has been applied to the data, namely no time calibration, randoms subtraction or normalization. The images acquired with the commercial tomograph were reconstructed using Filtered Backprojection (ramp filter applied).

Evident artifacts and inhomogeneities apparent in the raw images demonstrate that application of the above mentioned corrections is indeed necessary in order to acquire artifact-free images, however the basic structures of interest such as the myocardium and the left ventricle, are clearly resolved in both cases with comparable resolution.

Chapter 5

Discussion of Part I

As outlined in Chapter 1, the investigation of various human diseases in nuclear medicine necessitates the development of new radiotracers which will furthermore require high-resolution, sensitive imagers in order to quantitatively determine the pharmacokinetics and consequently the various biological processes on animal models.

Towards this direction, a small animal Positron Emission Tomograph based on pixellated Lutetium Oxyorthosilicate scintillation crystals read out individually by Avalanche Photodiode arrays has been developed in the Nuclear Medicine Department of Klinikum rechts der Isar of the TU München. Its unique, complicated hardware structure is able to provide Depth of Interaction information by means of a dual radial detector layer, whereas at the same time the individual crystal readout minimizes the system's dead time and in addition may lead to an enhancement of sensitivity through the identification of intercrystal scatter. MADPET-II is thus a powerful research tool for investigating the limits that can be achieved between spatial resolution and sensitivity.

The investigation of these limits has been of interest for several groups. The use of long crystals with a pixel size smaller than 1×1 mm^2 is a rather straightforward way of achieving submillimeter spatial resolution and is currently being investigated for the use in small animal PET [95]. However the construction of arrays consisting of such minute elements and moreover their mounting to the photodetector area and the light collection may prove to be an extremely difficult procedure [49]. Different detector configurations using several layers of very thin scintillation crystals read out by Position Sensitive APDs (PSAPDs), opt for very high light collection providing at the same time high sensitivity and spatial resolution [50, 49]. Another approach to improve the spatial resolution is to use a virtual pinhole geometry by means of a detector insert within the FOV of the PET scanner [101]. Recent results have demonstrated that implementing this concept leads to submillimeter spatial resolution and a significant enhancement of sensitivity.

Even though the detector concept of MADPET-II is simple and more straightforward compared with the typically used block detector design, its implementation has been a long-lasting and complicated procedure demanding special considerations in both hardware and software development. In order to guarantee reliable and reproducible scanner performance, the exceptionally large number of detector and electronic channels of

MADPET-II needs to be separately monitored and tuned. In this work, a description of the front-end construction and of the complete system integration has been given, followed by the performance evaluation of the front-end and analog signal processing chain. An assessment of the system's DOI capabilities has been presented and first in vitro animal images have been shown.

It should be noted that the extrapolation of a similar hardware concept to the clinical range would be a cost inefficient process due to the tremendous amount of electronic channels required, however the results presented in this part of the work demonstrate the promising potential of a PET system employing the special features of MADPET-II, for quantitative, high-resolution imaging. It is evident that prior to this goal, a number of corrections need to be applied to the acquired data in order to compensate for effects that may degrade image quality. As mentioned in Chapter 2, normalization correction and randoms subtraction is a necessity and efforts in our group are currently focusing on implementing these corrections to the acquired data [106, 107, 82]. Further steps also involve performance evaluation of the tomograph in terms of spatial resolution, dead time, sensitivity and image quality.

Part II

Investigation of Novel Detector Technologies for Simultaneous PET/MR Imaging

Chapter 6

Characterization of LYSO-SiPM detector modules and comparison with an LSO-APD detector

Work published in Journal of Instrumentation, Institute of Physics Publishing (IOP) (V. C. Spanoudaki et al. 2007 JINST 2 P12002)

6.1 Introduction

As outlined in Chapter 5, detector technology for PET evolves rapidly towards designs that may warrant more accurate position information. In Chapter 1 it was mentioned that multimodality imaging, such as PET/CT, has successfully managed to merge functional and anatomical information in order to more accurately localize functional information. Currently, efforts are focusing on PET/MR, which is aiming at combining the higher MR soft tissue contrast with PET, minimizing at the same time the received radiation dose by the patient. Simultaneous PET/MR acquisition requires highly demanding detector design in order to avoid interference of one modality to the other [74]. The advantages of APDs compared to PMTs have been described in Section 2.2.1.3 and the feasibility of using APDs in PET imaging has been shown in several studies [114, 73, 76]. However, the low internal gain of APDs necessitates the use of sophisticated, low noise amplifiers, which furthermore will require stringent shielding against Electro-Magnetic Interference (EMI) inside the limited FOV of the MR scanner. In addition, the significantly worse timing of the APD signals due to low gain and higher noise, compared to PMT signals, limits the overall time resolution of the imaging device.

Recently SiPMs have attracted interest for their use as scintillator readout in PET applications since they combine a number of advantageous properties, also summarized in

Section 2.2.1.4 [71, 72, 62, 33, 32, 13, 17]:

- A similar gain as PMTs in the order of 10^6. Thus no complicated, application-specific front-end electronics is needed. This is expected to be of major advantage inside an MR tomograph since the number of processing electronics and therefore the shielding requirements are minimized.
- The single photoelectron resolution for modest photon fluxes facilitates very accurate time pick-off and in principle a sub-nanosecond time resolution.
- Their insensitivity to magnetic fields and their minimal EMI pickup make them appropriate for use in combined PET/MR imaging.

The SiPM architecture is based on an array of single channel APDs (cells) operating in limited Geiger mode (i.e. biased above breakdown) as shown in Figure 6.1. Due to the nature of the quenching mechanism each cell outputs a standardized pulse independent of the number of photons incident to it. Thus each cell is operating in binary mode only indicating if it has fired or not [26]. Quantitative information about the number of incident photons is given by the output signal of the SiPM array which is the sum of the signals of the individual APDs connected to each other through a polysilicon resistor. However, due to the limited number of APDs in a SiPM, for photon fluxes greater than 1 photon per cell and recovery time, non-linear effects take place which may limit the SiPM's performance in terms of energy and time resolution [96].

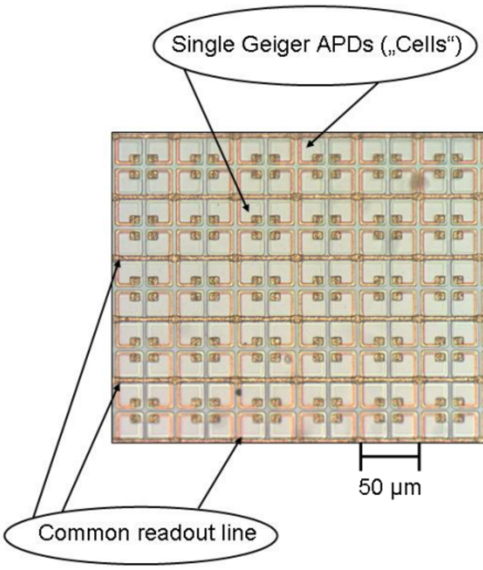

Figure 6.1: Microscopic view of the SiPM architecture.

The purpose of this study is to investigate a novel detector concept for simultaneous PET/MR imaging based on SiPMs read out by a sampling ADC based data acquisition system. The non-linear dependence of pulse height on the number of incident photons

Table 6.1: The operational characteristics of the SiPMs used in this study.

SiPM	Company	$V_{breakdown}$	No. of cells	Sensitive area	Cell size
1-4	Pulsar & MEPhI	80 V	1024	1×1 mm^2	25×25 μm
5-6	Hamamatsu	70 V	1600	1×1 mm^2	25×25 μm
7-8	Hamamatsu	70 V	400	1×1 mm^2	50×50 μm

and the influence of this effect on the energy resolution and timing properties of LYSO-SiPM detectors has been studied and compared to corresponding properties of an LSO-APD detector.

6.2 Materials and experimental setup

For this study four SiPMs from Moscow Engineering & Physics Institute, PULSAR Enterprise and four Multi Pixel Photon Counters (MPPCs, series S10362-11-025U/050C) from Hamamatsu Photonics have been used. Table 6.1 summarizes some characteristics of the devices used.

6.2.1 Single-channel SiPMs

The single channel SiPMs used are shown in Figure 6.2 (left). The SiPMs with cell sizes of 25 μm $\times$ 25 μm were used as single channel devices. Each SiPM is mounted in a metal can housing covered by a glass window. There is an air gap of approximately 1 mm between the entrance window and the sensor. These devices have been evaluated as light detectors when illuminated with light emitted from a LED. They were also coupled to $1.4 \times 1.4 \times 12$ mm^3 LYSO scintillation crystals (Saint-Gobain Crystals, Nemours Cedex, France) and energy spectra were acquired using a ^{22}Na source. In order to optimize the light collection, the crystals were wrapped in specular reflector (3M radiant foil) and coupled to the photodetectors by means of optical adhesive (Delo Photobond 400) with a refractive index of 1.6.

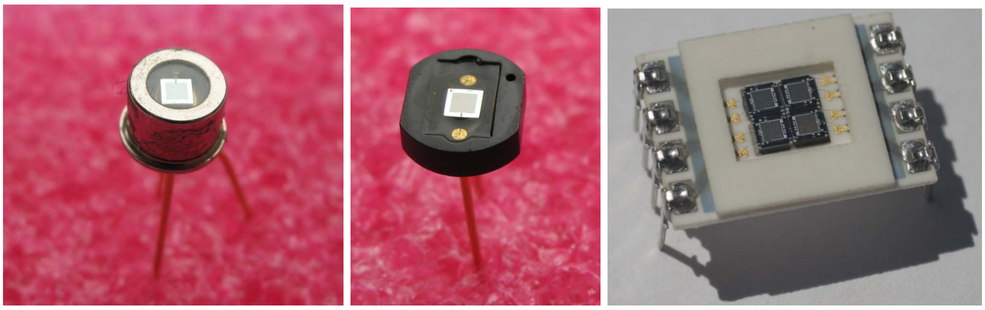

Figure 6.2: Photos of the single channel SiPMs with 1600 (left) and 400 (center) cells used in this study. The 2×2 SiPM array mounted on a ceramic chip carrier is also shown on the right photo.

The SiPMs with cell sizes of 50 μm × 50 μm were mounted in a ceramic housing and covered with resin. They were also coupled to the scintillation crystals in the same way as mentioned above and were operated in coincidence inside a clinical MR tomograph during various typical MR sequences used for clinical studies. The detector pair was irradiated by a ^{18}F-FDG point-like source placed in the center between the crystals.

6.2.2 2 × 2 SiPM array

The 4 SiPMs from Pulsar and MePhI were used to fabricate a 2 × 2 detector array, as shown in Figure 6.2 (right). The total area of one SiPM chip is 2 × 2 mm^2 and the sensitive area is 1 × 1 mm^2. In the array the sensors are separated by approximately 0.3 mm and mounted on a ceramic chip carrier. The chips and bond wires are protected by an epoxy coating of 0.8 mm thickness. A 0.5 mm thick silicon pad was placed on top of the SiPM array as a lightguide. A collimated light source was used to illuminate the array at various positions and the 2-D position histograms were determined based on the light sharing among the four photodetectors.

6.2.3 Data acquisition electronics

The detector signals were initially fed to standard NIM electronics. A Constant Fraction Discriminator (935 Quad CFD, Ortec) was used to produce trigger signals and a Multi-Channel Analyzer (3001 QVt MCA, LeCroy) was used for the acquisition of energy spectra when operating in charge integration mode. The same MCA was also used to record coincidences between the two opposing detectors when operating in start-stop mode.

For the measurements inside the MR tomograph, a sampling ADC based data acquisition system was used instead [54]. The detector signals are continuously digitized with an 80 MHz sampling rate and energy spectra are reproduced from the maximum pulse height. A time stamp was assigned post acquisition to every detected event by applying a software-based CFD timing pick-off method. Thus, coincidences between the detectors were sorted in software from these data.

For the position reconstruction using the SiPM array, the signals of the four detectors were fed to the analog inputs of a fast digital oscilloscope (1 GHz bandwidth, 4 Gsamples/s, Agilent Infiniium, 54832D).

6.3 Results

6.3.1 Measurements with light pulses produced by a LED: SiPM linearity and recovery time effects

Despite the large potential of SiPMs for their use in PET, their response may become non-linear under specific conditions:

- As already mentioned, the limited number of cells (N_{cells}) in a SiPM limits the detector's dynamic range. Hence, if the number of incident photons per unit time is

$\frac{dN_{inc}}{dt}$ and the number of incident photons within a time window Δt, $\frac{dN_{inc}}{dt} \cdot \Delta t$, exceeds the number of cells in a SiPM, the detector output will be non-proportional to the number of incident photons. Assuming an infinite recovery time τ, the detector output in terms of fired cells (N_{fired}) may be modelled by Equation 6.1:

$$N_{fired} \propto N_{cells} \cdot \left(1 - e^{-\frac{\frac{dN_{inc}}{dt} \cdot t \cdot PDE}{N_{cells}}}\right) \tag{6.1}$$

where PDE is the Photon Detection Efficiency of the device. For the derivation of Equation 6.1 a generalized Poisson distribution [42, 5] for the probability of photon detection by each cell is assumed (Appendix B). Figure 6.3 illustrates the dependence of the number of fired cells on the number of incident optical photons per cell as predicted by Equation 6.1 when assuming a long recovery time.

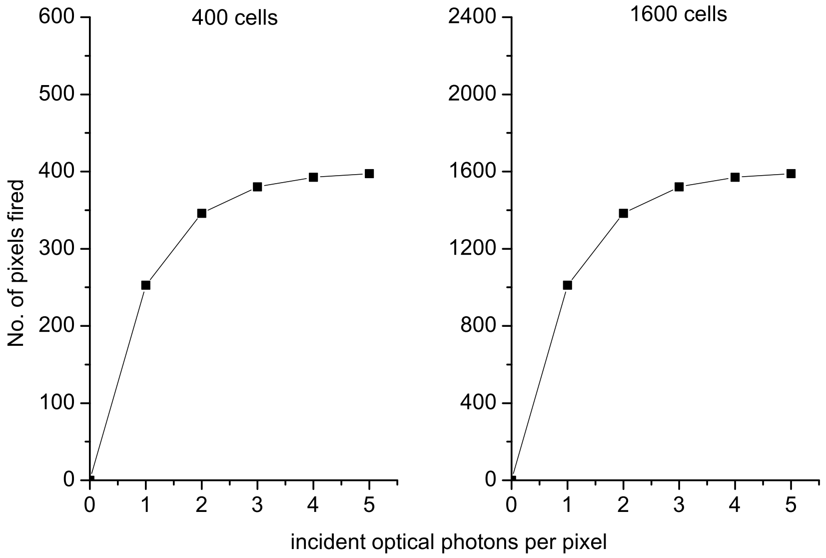

Figure 6.3: Dependence of the number of fired cells on the number of incident optical photons per cell as predicted by Equation 6.1 when assuming a long recovery time.

- In addition, the linear response of each SiPM cell to successive light stimuli is also affected by the limited recovery time of the individual Geiger APDs, namely by the time each cell needs to recover from a Geiger discharge and to refire [15]. This time is determined by the characteristic time constant of the cell defined by the product of its capacitance C_{cell} and the value of the polysilicon resistor R_{cell} attached to it [18].

Thus, for photon fluxes higher than 1 photon per cell and recovery time, non linearity effects will affect the output of the detector which may be approximated by Equation 6.2.

$$(6.2)\quad N_{fired} \propto N_{cells} \cdot \left(1 - e^{-\frac{\frac{dN_{inc}}{dt}\cdot t\cdot PDE}{N_{cells}}}\right) \cdot \left(2 - \frac{1}{1+\frac{N_{cells}}{\tau\cdot\frac{dN_{inc}}{dt}\cdot PDE}} \cdot \frac{1-e^{-\frac{\frac{dN_{inc}}{dt}\cdot t\cdot PDE}{N_{cells}}-\frac{t}{\tau}}}{1-e^{-\frac{\frac{dN_{inc}}{dt}\cdot t\cdot PDE}{N_{cells}}}}\right)$$

For the derivation of Equation 6.2 we assume an exponential recovery of each cell with a time constant τ. At the limit $\tau \longrightarrow \infty$, Equation 6.2 degenerates to Equation 6.1. As an example, for a SiPM with 1600 cells, a 25 % PDE and a 50 ns recovery time, the behaviour described in Equation 6.2 is illustrated in Figure 6.4. The PDE of a SiPM is defined in first order as the product of the geometric efficiency of the device, namely the $\frac{sensitive}{total}$ photodetector area, the QE and the probability of an avalanche breakdown. It is obvious from Figure 6.4 that the finite recovery time of the individual cells results in an increase of the effective dynamic range of the SiPM, however this increase may be non-linear depending on the intensity of the incident photon flux.

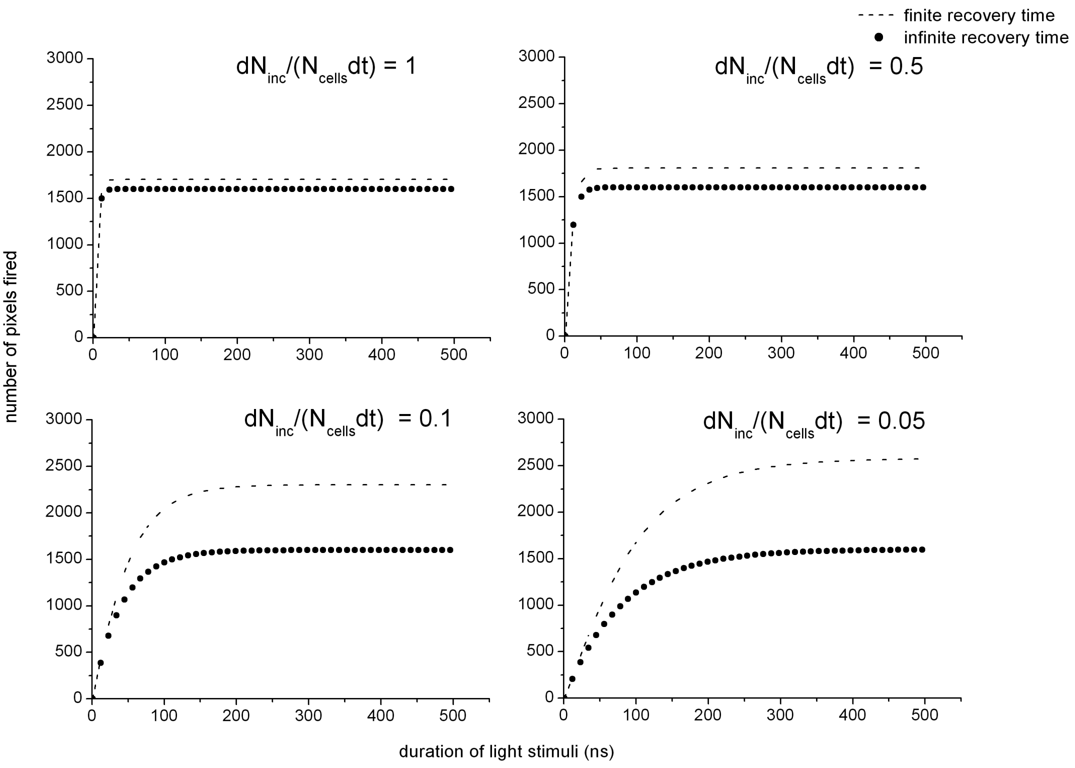

Figure 6.4: Theoretical prediction of SiPM output signal when considering a finite (dashed line) and an infinite (points) recovery time of the cells for various values of the incident photon fluxes per cell.

In order to experimentally confirm the non-linear behaviour predicted by theory, the device was illuminated with light pulses from a low intensity Light Emitting Diode (LED). The period of the light pulses was kept large enough so as to allow full recovery of the

SiPM. We studied the response of these devices in terms of linearity, by successively varying the duration of the light flashes. The full duration of the output's rising edge (defined as rise time in Figure 6.5) is determined by the duration of the incident light pulse, meaning that the device responds to the light stimuli of all durations. Figure 6.5 depicts the observed amplitude and rise time of the SiPM output pulse when illuminated with light pulses of varying durations from 10 ns to 500 ns with steps of 10 ns.

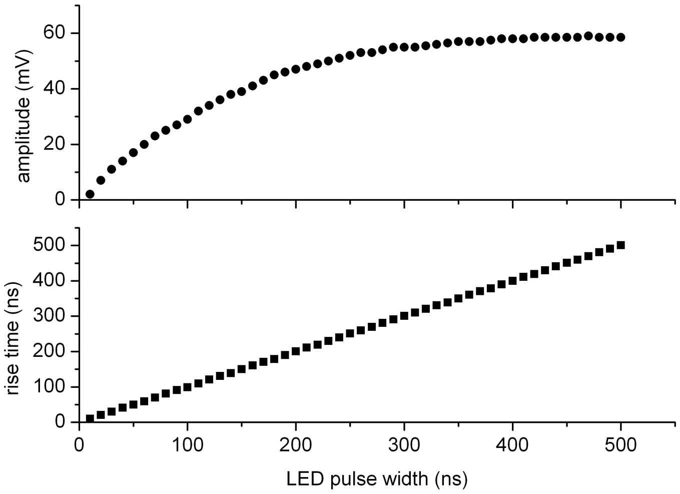

Figure 6.5: Top: SiPM output pulse height as a function of the LED pulse width. Non-linearities are visible for increasing duration of the light stimulus. Bottom: rise time of the SiPM output pulse as a function of the LED pulse width.

In the top plot of Figure 6.5, one observes that there is no change of the pulse height with increasing LED pulse width for widths above 400 ns, namely the device is fully saturated. The corresponding SiPM output signals are shown in Figure 6.6.

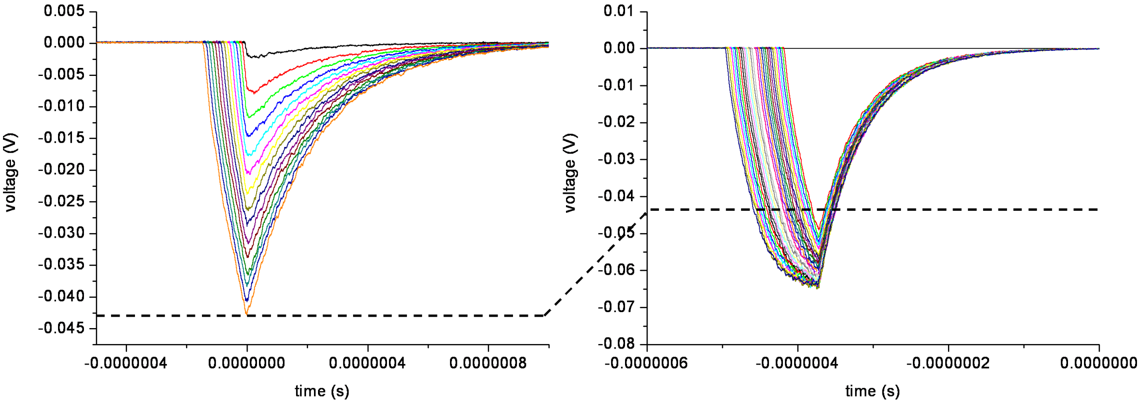

Figure 6.6: SiPM output signals for various widths of the incident LED light pulse for the case of linear (left) and non-linear behaviour (right). The dashed line indicates the relationship between the signal amplitudes for these two cases.

Variations on the dynamic range of a SiPM due to the limited number of cells and the finite recovery time may also lead to deviation of the SiPM response from Poisson statistics (Appendix B), as illustrated in Figure 6.7. Measurement of the SiPM intrinsic resolution, defined as $\frac{FWHM}{peak}$ of the pulse height distributions shown in the left plot of Figure 6.7 for various LED pulse durations, has shown a degradation when a large number of optical photons is incident to the detector. If the extracted values of intrinsic resolution are plotted as a function of the inverse square root of the incident LED pulse width, deviation from linearity is observed for excessive widths namely excessive photon fluxes (right plot of Figure 6.7). This behaviour indicates, as opposed to the excess noise factor of the APD F_{APD} defined in Section 4.3.2, a non-constant excess noise factor F_{SiPM} for the SiPM which is dependent on the incident photon flux and therefore on the number of the available cells on the detector's sensitive area.

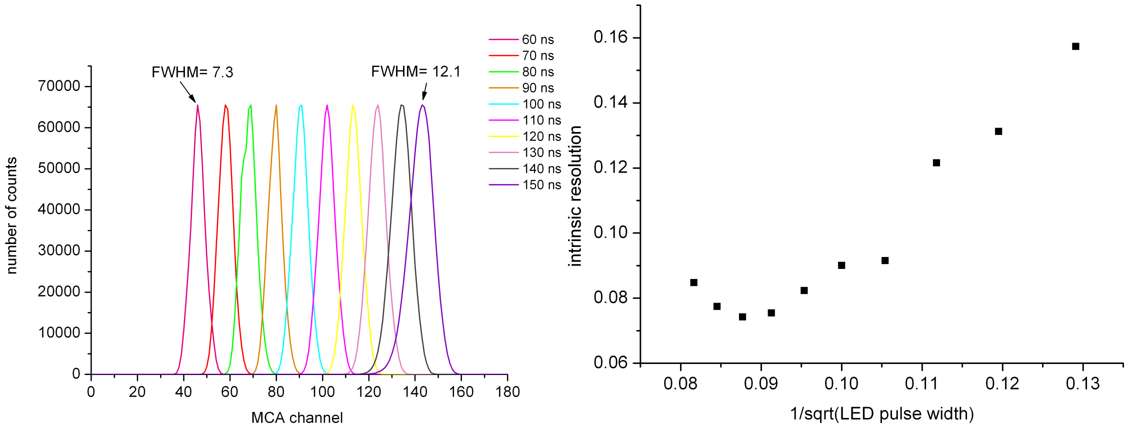

Figure 6.7: SiPM intrinsic resolution as a function of incident LED light pulse width. Left: broadening of the SiPM response with increasing number of incident optical photons. Right: deviation of the SiPM response from Poisson statistics for a large number of incident optical photons.

6.3.2 Measurements with scintillation light pulses: SiPM-LYSO vs. APD-LSO energy and time spectroscopy

^{22}Na spectra with a single channel LYSO-SiPM detector and with a $2 \times 2 \times 8$ mm^3 LSO (CTI, Knoxville, USA)-APD (S8550, Hamamatsu, Japan) detector are compared in Figure 6.8. The signals from the LSO-APD detector were fed to an integrated CSP [75] followed by the analog processing electronics described in Section 3.4 (100 ns shaping time). The achieved energy resolution is 20.9% for the 1600-cell SiPM (Figure 6.8) and 17.9% for the 400-cell SiPM (Figure 6.13) and is comparable to the LSO-APD energy resolution of 17%. These values can be expected to further improve taking into account the current factors that contribute to a degradation of the energy resolution:

- In the case of the 1600-cell SiPM, the air gap in the metal housing between the LYSO crystal and the sensitive area of the sensor results in total internal reflection of the produced scintillation light back to the scintillation crystal, due to mismatch

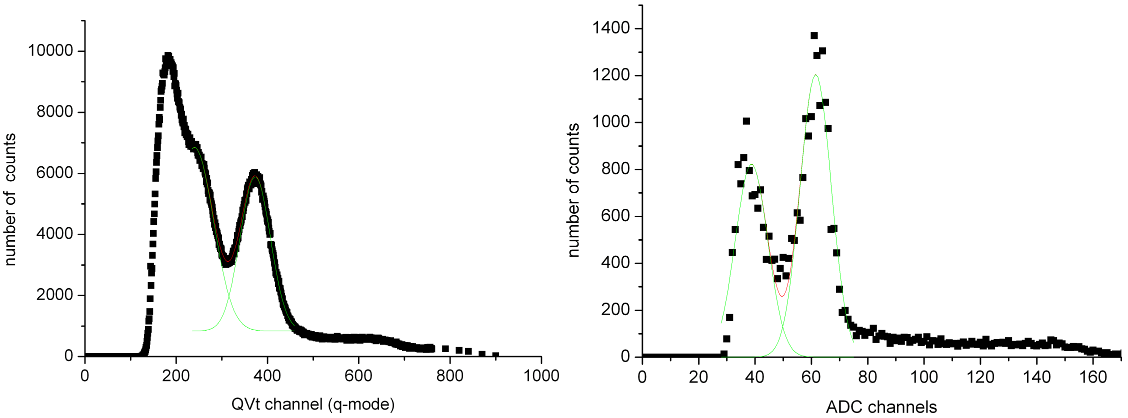

Figure 6.8: ^{22}Na energy spectra acquired with a LYSO-SiPM (left) and with a LSO-APD (right) detector.

among the refractive indices of the crystal ($n_{LYSO} = 1.82$) and the air ($n_{air} = 1.00$). Figure 6.9 (left) indicates a loss in the number of detected photons of approximately 70% originating from this mismatch.

- The 1.4 × 1.4 mm^2 LYSO crystals mounted to the 1 × 1 mm^2 sensitive area of the SiPMs led to a 1:2 mismatch between crystal pixel area (crystal pixel is defined as the side of the crystal facing the entrance window of the photodetector) and the photodetector sensitive area. Figure 6.9 (right) illustrates the dependence of the light detected by the SiPM on the crystal pixel size for various crystal lengths, as estimated by simulations performed using the DETECT2000 photon tracking simulation package. The light output demonstrates an exponential dependence on the crystal pixel size, leading to a 50% light loss for the case of the above mentioned mismatch. This would be of particular importance for a significantly small number of incident optical photons, in which case photon statistics is the dominant source of energy resolution degradation compared to intrinsic LSO resolution. It should be noted that there was also a mismatch between the areas of the crystal and the photodetector in the case of the LSO-APD detector (APD sensitive area: 1.6 × 1.6 mm^2).

The time resolution, on the other hand, may also be significantly influenced by non-linear effects depending on the time pick-off method used. In Figure 6.10, measured time coincidence histograms acquired with LYSO-SiPM and with LSO-APD detectors are shown. The CFD produces a trigger at a specific fraction of the input pulse independent of the pulse amplitude, assuming that the pulse shape remains constant. For pulse shapes that vary, however, this method may result in inaccurate timing. The achieved time resolution using this method (no shaping, 4 ns delay) is 1.9 ns FWHM for two LYSO-SiPMs in coincidence, that is 1.4 ns for each individual one (Figure 6.10, left graph). This value is expected to improve using a time pick off technique based on the signal shape and by increasing the light collection efficiency of the detector. It should be mentioned that the chosen CFD delay value does not correspond to the $\frac{2}{3}$ of the signal rise time (approximately 20 ns), which would theoretically result in the best timing. It has been chosen to be large enough in order to avoid arming trigger errors but small enough in order to

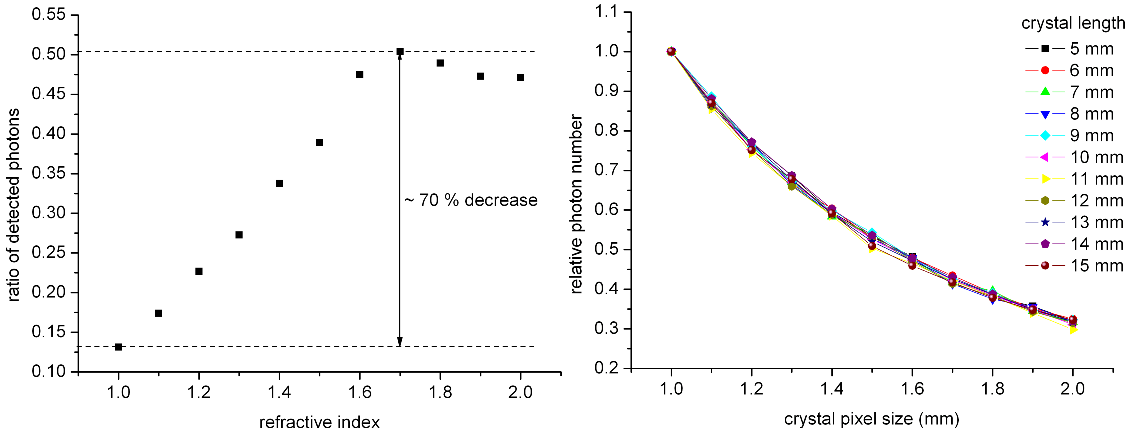

Figure 6.9: Left: number of detected optical photons as a function of the refractive index of the optical coupling. The numbers on the y-axis are normalized with respect to the number of photons initially produced in the scintillation crystal. Right: number of detected optical photons as a function of the crystal pixel size. The numbers on the y-axis are normalized with respect to the photon number for crystal pixel size 1 mm. The results from both graphs are based on simulations performed using DETECT2000.

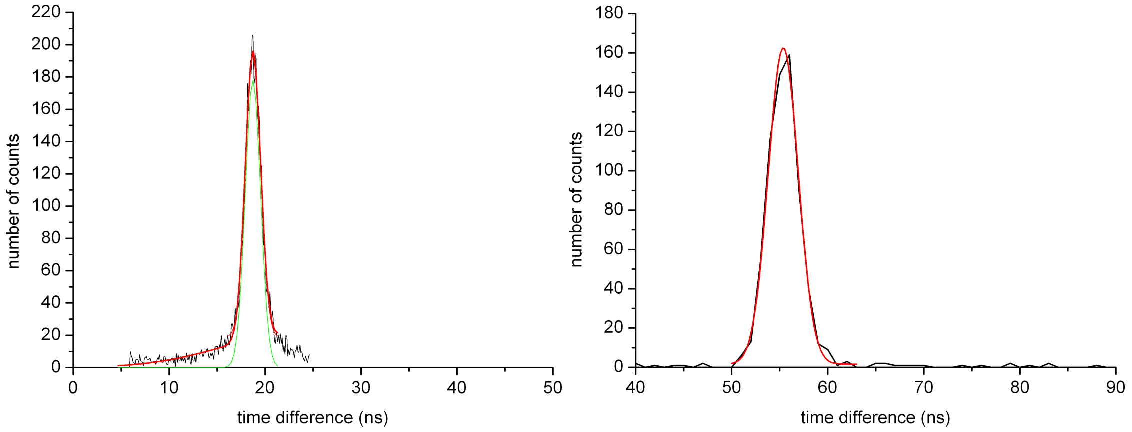

Figure 6.10: Time difference spectrum acquired with the two LYSO-SiPM detectors in coincidence (left). For comparison the time spectrum of an LSO-APD detector in coincidence with a plastic scintillator-PMT is also shown (right). Gaussian fits were applied to the histograms.

simulate the Amplitude and Rise time Compensated (ARC) time pick-off method [42]. For comparison, the time resolution (3.65 ns FWHM, CFD time pick off) of an LSO-APD detector against a plastic scintillator-PMT is also shown in Figure 6.10 (right graph).

As already discussed in Section 4.1, the theoretical limit of the time resolution σ_{res} is imposed by the signal rms noise σ_{rms} and the signal slope $\frac{dV}{dt}$ according to Equation 4.1. Figure 6.11 shows an oscilloscope view of LYSO-SiPM output signals when the detector is irradiated with 511 keV gamma rays. With no amplification and a 10 ns shaping time (integration/low pass), the signals are characterized by a 30 ns rise time and a 60 mV maximum amplitude. In the same figure, the rms noise of the SiPM has been measured for three different shaping times (integration) as a function of the applied bias. For the rms measurement, a 1 GHz bandwidth digital oscilloscope (Agilent Infiniium 54832) was used. Based on these data, a theoretical limit in the achievable SiPM time resolution

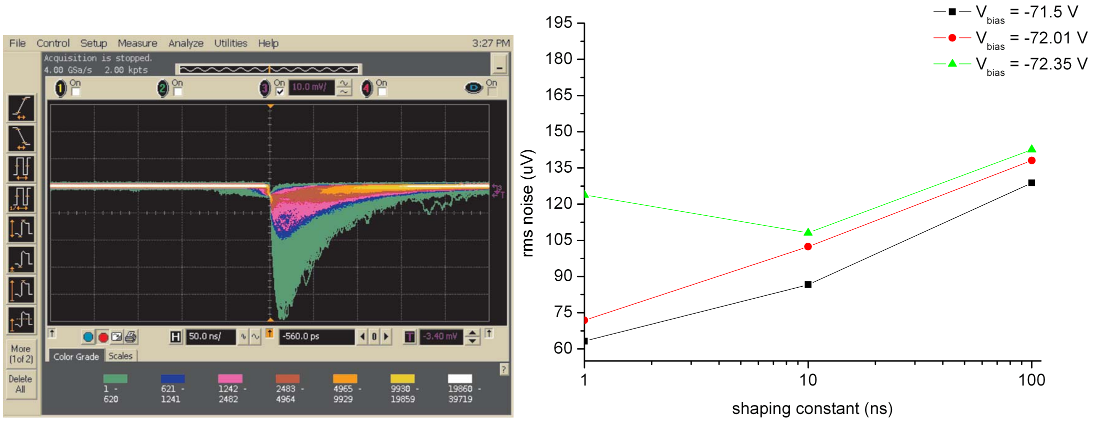

Figure 6.11: Left: Persistence view of LYSO-SiPM output signals. The rise time is 30 ns and the amplitude is approximately 60 mV read at a 50 Ohm load. Right: rms noise of the SiPM photodetectors as a function of shaping time for different bias voltages.

can be estimated, which in the case of 100 μV rms noise, can be as low as 50 ps. If the transit time spread of the SiPM is also taken into account, the lower limit of the achievable time resolution may reach a few hundreds of picoseconds [2]. This lower limit could potentially demonstrate SiPMs as appropriate photodetectors for use in Time-of-Flight (TOF) PET imaging, where subnanosecond time resolution is required [16, 43].

However, deviation from the above mentioned theoretical limit may be observed due to photoelectron statistics which, in the case of SiPMs, is strongly affected by the limited number of cells and by the fact that each cell may be triggered by only one photon during its recovery time. The number of fired cells has been calculated for the 400-cell SiPM by comparing the position of the 511 keV peak in a ^{22}Na spectrum to the position of the single electron peaks in the dark count spectrum. After correcting for different amplification of the signals when acquiring dark count spectra compared to gamma spectra, in which case the signals needed to be attenuated, a number of 300 ± 80 fired cells has been estimated. A theoretical prediction based on Equation 6.1 using a PDE of 50% and an incident optical photon number of 3700, as estimated by optical simulations performed with DETECT2000, yields a number of 396 fired cells. As it can be seen from the left graph of Figure 6.3, for this number of fired cells the SiPM response becomes non-linear, therefore an accurate calculation of the produced photoelectrons $N_{phe} = N_{inc} \cdot PDE$ (solution of Equation 6.1 given the experimentally derived N_{fired}) is difficult. In addition, optical crosstalk induced from a fired cell to the neighbouring ones (Section 6.3.3) may result in overestimation on number of fired cells and consequently, provided that the SiPM has a linear response, in an overestimation of the quantity N_{phe}.

The predicted values of fired cells and produced photoelectrons for the 1600-cell SiPM (25% PDE) are 704 and 924, respectively. When the photoelectron number is the dominant factor in the accuracy of time estimation, a linear dependence of time resolution on the inverse square root of the photoelectron number (and therefore on the inverse square root of the number of fired cells, in case of linear response) may be assumed as a first approximation [20]. Thus, in the case of the 1600-cell SiPM an improvement of approximately 20% is to be expected. Experimentally, an improvement in time resolution of 12% has been observed for the 1600-cell SiPM compared to the 400-cell one.

In order to fully exploit the excellent timing properties of such detectors and reach the above mentioned timing limits, efforts are focused towards early digitization of the detector signal, thus minimizing the analog signal processing [54, 12], as well as towards timing pick-off methods based on the first photoelectron.

6.3.3 Effect of dark counts and optical crosstalk on energy and time resolution

Thermally produced electron-hole pairs within the depletion layer of individual cells in a SiPM may induce a Geiger discharge, resulting thus in a pulse which is not associated with any optical stimulation (dark counts). In addition, an individual cell which is either thermally or optically excited may induce optical crosstalk to the neighbouring cells [44], namely an optical photon produced during the Geiger discharge of the excited cell may be transmitted to a neighbouring cell through either the device substrate, the device coating (typically epoxy or resin) or even through the scintillation crystal coupled to the SiPM. Both dark counts and optical crosstalk may affect the accuracy of photon detection:

1. Single electron pulses resulting from the Geiger discharge of each cell have a very well defined shape. Dark counts as such, if detected as individual events, may be easily discriminated in the acquired energy spectra simply by setting an appropriate energy threshold. The same is valid in the case of optical crosstalk induced by a thermally excited cell, since the output pulse will be the sum of a limited number of cells. The well defined crosstalk "peak" is shown on the left graph of Figure 6.12. On the right graph of Figure 6.12, a relative measurement of the dark count rate as a function of threshold is shown. The lower value of the energy threshold corresponds to 100 keV.

2. Alternatively, since the output signal of the SiPM is the sum of the output signals of each individual cell, dark counts or optical crosstalk, induced by a thermally excited cell, may as well randomly add to the output pulse, in which case energy thresholding cannot eliminate them. The contribution of these effects to the broadening of the photopeak, namely the degradation of the energy resolution, may be significant especially in the case of limited photoelectron statistics. For the energy spectrum of Figure 6.12, the contribution of crosstalk to the energy resolution is approximately 4%, which was estimated by dividing the FWHM of the far left crosstalk peak by the photopeak position. It should be mentioned that the accuracy of this estimation is hindered by the lower energy threshold which was set in order to discriminate the dark counts from electronic noise. On the other hand, optical crosstalk induced by an optically excited cell will result in a larger number of firing cells for a specific number of incident optical photons, since for every "primary" fired cell, there will be a number of "secondary" cells which will fire with a given probability. The

net effect in the acquired energy spectra will be a shift of the photopeak to higher channels.

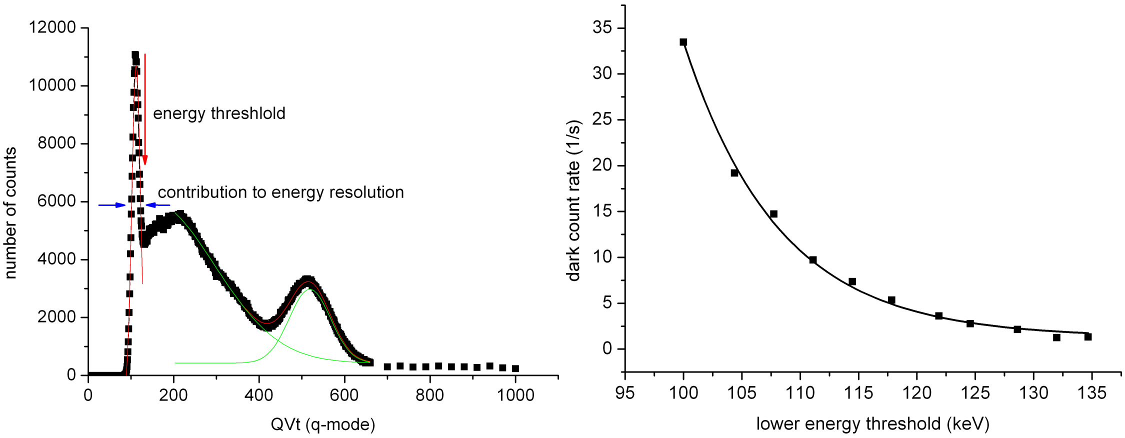

Figure 6.12: Contribution of dark counts and optical crosstalk to energy resolution: on the left graph, the first peak corresponds to individual dark count/crosstalk events that may be discriminated by energy thresholding (read arrow) due to their well defined shape. In addition, the FWHM of the crosstalk peak may be used to estimate its contribution to the degradation of energy resolution. On the right graph a decreasing number of dark counts with increasing threshold setting is observed.

Concerning time resolution, dark counts may contribute to an increased number of recorded accidental coincidences, thus adding an enhanced background to the time coincidence histogram. Increasing the energy threshold may eliminate this effect.

6.3.4 Measurements inside a magnetic resonance tomograph

The SiPM functionality inside a strong magnetic field was tested by placing two LYSO-SiPM detector modules in coincidence inside the bore field of view of a 1.5 Tesla Achieva whole body Magnetic Resonance scanner (Philips Medical Systems, Best, Netherlands). The acquisition electronics was placed remotely outside the MR scanner room. No special care was taken for shielding of the coincidence setup. Energy spectra and time coincidence histograms were acquired during a typical Diffusion Weighted Imaging (DWI) sequence used for standard clinical brain studies. Figure 6.13 shows the acquired energy spectra and time coincidence histograms (right), as well as the simultaneously acquired MR image showing two water bottles placed at opposing ends of the coincidence setup as a reference signal (left). Except from the evident artifacts in the MR image caused by the RF coupling of the unshielded magnetic components of the coincidence setup, the PET acquisition remains unaffected by the presence of static and gradient magnetic fields, thus making the SiPMs appropriate for use in simultaneous PET/MR imaging. A slight effect of additional shaping on the output signals may appear due to the long coaxial cables (approx. 10 m long) used to lead the detector signals on the remote data acquisition system. The sampled detector signals prior and during the concurrent MR measurements are shown in Figure 6.14. The energy spectrum was extracted from the

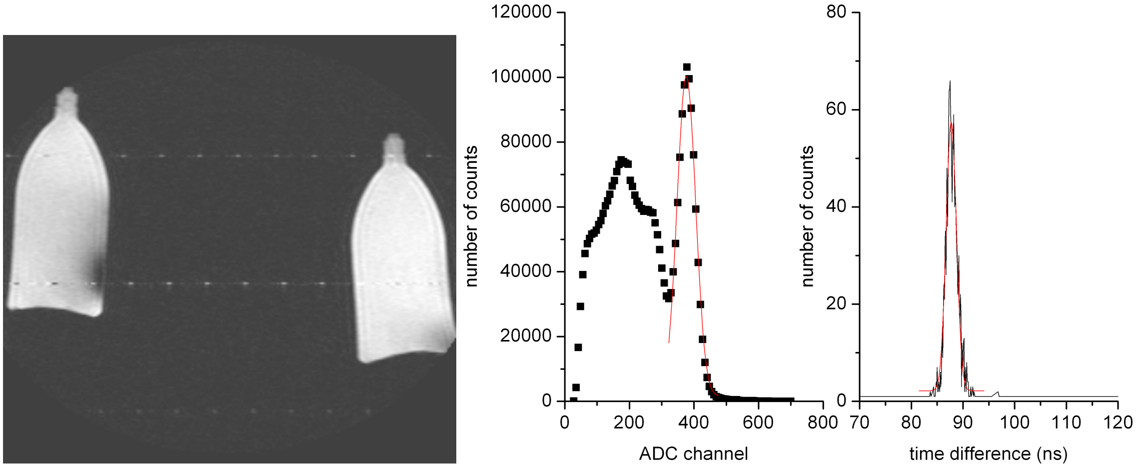

Figure 6.13: MR image (left) and simultaneously acquired energy spectra and time coincidence histograms (right) with two LYSO-SiPM detectors in coincidence. No degradation in energy and time resolution was observed. Two bottles filled with water were used as phantoms doing MR imaging.

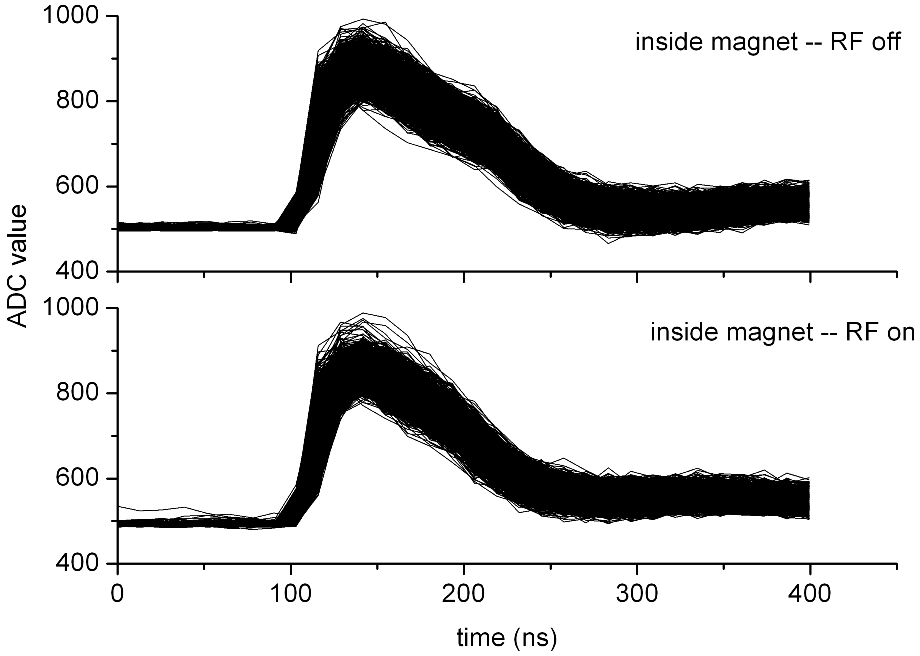

Figure 6.14: Sampled detector signals inside the MR scanner during the presence of static (top) and gradient (bottom) magnetic fields.

digitized amplitude of the detector pulses and showed a 17.9 % energy resolution. As mentioned in Section 6.2, the time resolution of 1.6 ns for each LYSO-SiPM detector was extracted using a digital, FPGA-based CFD algorithm. No amplification or shaping was included on the front-end, only the op-amp stage preceding the sampling ADCs was used. The above values are possibly degraded due to the limited sampling points on the rising edge of the detector signal (rise time approximately 30 ns, digitization every 12.5 ns). Currently alternative algorithms are evaluated in order to fit the detector signals more accurately.

6.3.5 Event localization in a SiPM-based block detector architecture for PET

Light sharing techniques are widely applied to PET scanners which implement block detector architectures. The scintillation light, produced by either a finely pixellated array of crystals or by a continuous crystal layer, is shared within an array of photodetectors by means of a light guide. The origin of the interaction point is defined by the relative weights of the photodetector signals using appropriate algorithms (Anger logic) [104]. Detector linearity is therefore a key feature for the reliable event localization within a block detector. The effect of SiPM non-linearities, as demonstrated in Section 6.3.1, in the performance of a possible block detector design based on SiPMs has been simulated and experimentally verified.

The measurements presented in this section have been performed using a red LED instead of a scintillation crystal in order to better match the array's peak sensitivity. The light source was collimated and placed at 9 different positions across the whole surface of the array, as illustrated on the top schematic of Figure 6.15. A silicon pad of 0.5 mm thickness was used as a light guide in order to facilitate the distribution of light from the LED to the four photodetectors. For every position, the maximum pulse amplitudes from each of the four SiPMs (denoted as A, B, C and D in Figure 6.15) were recorded and the position of the light source was reconstructed using the following equations:

$$X = \frac{(B+D)-(A+C)}{A+B+C+D}, \qquad Y = \frac{(A+B)-(C+D)}{A+B+C+D} \tag{6.3}$$

The effect of the non-linear SiPM behaviour on the position reconstruction was studied in the same way as in Section 6.3.1, by varying the LED pulse width. In Figure 6.15, the 2D position histograms are shown for various LED pulse widths, as well as the simulated one. The measured position histograms depicted in Figure 6.15 show that all nine positions of the light source can be resolved independent of the duration of the light stimuli. Apparent differences in the resolution of the reconstructed positions can be mainly attributed to the precision of the mechanical setup.

The light sharing technique results in distribution of light among the four photodetectors and, therefore, in four signals whose relative proportionality is indicative of the position of the light source. It is thus expected that the non-linear SiPM response may quantitatively affect the position information extracted from the array.

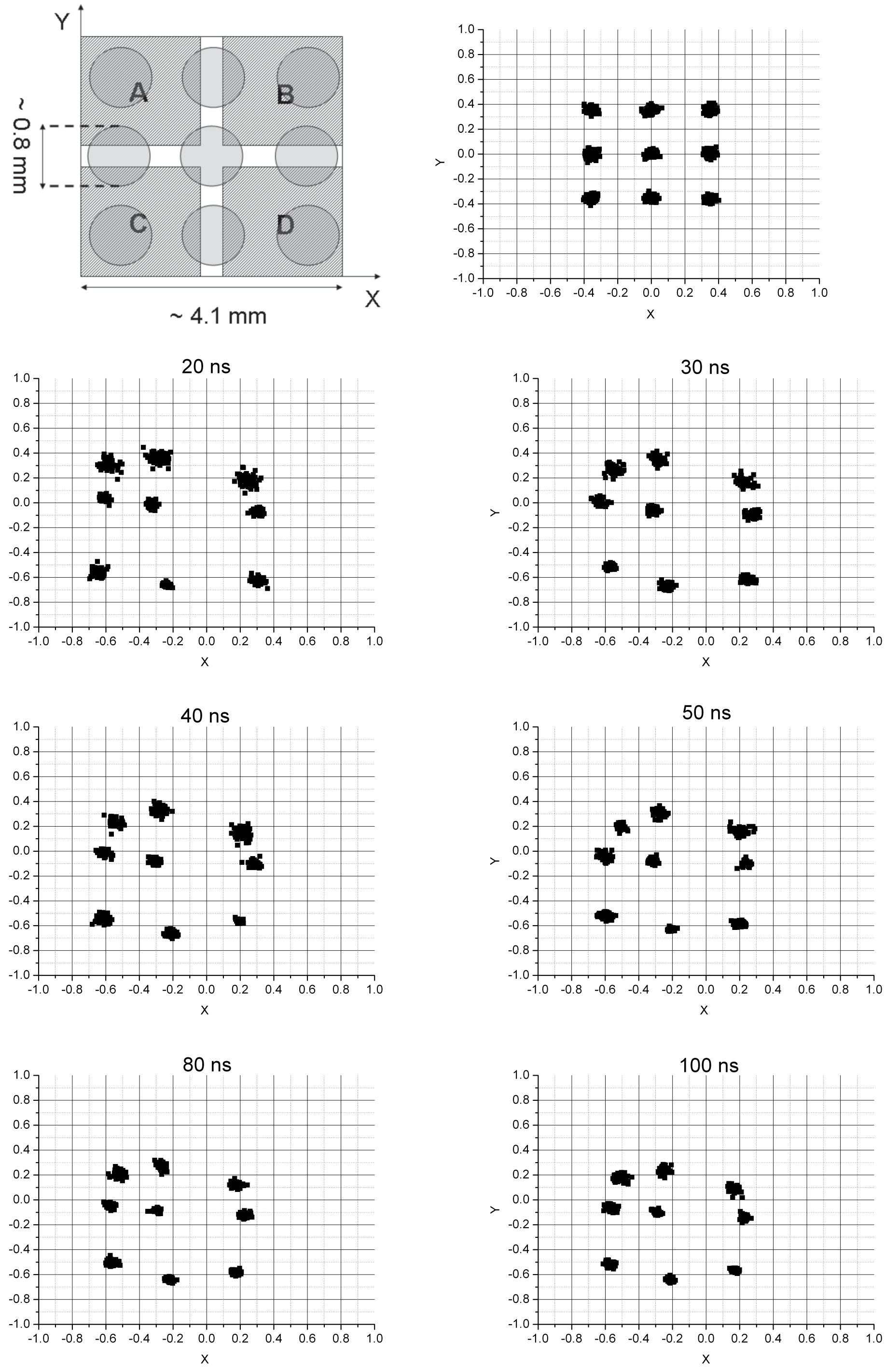

Figure 6.15: Top row: illustration of the various positions of the light source with respect to the position of the SiPMs in the 2 × 2 array (left graph) and the 2-D position histogram using simulated data from DETECT2000 (right graph). Next 3 rows: measured position histograms for various durations of the LED pulse width.

Chapter 7

Discussion of Part II

In Sections 1.2 and 6.1 the advantages of multimodality imaging have been outlined with particular emphasis to PET/MR imaging. Even though PET/CT is currently the dominant imaging modality implemented in clinical routine, results from an LSO-APD based PET insert prototype inside a 7 T Magnet have demonstrated the feasibility of performing a simultaneous PET and MR acquisition without significant degradation of neither modality [39].

In this study the feasibility of implementing a simplified detector concept using SiPMs as photodetectors for scintillator readout, as well its potential for use in combined PET/MR imaging is investigated. The experimental findings demonstrate that SiPMs exhibit a similar performance to proportional APDs in terms of energy resolution and a superior performance in terms of timing. These features can be achieved even by eliminating additional amplification stages due to the high gain of these devices. Pulse shape variations due to non-linear detector response to light stimuli of extended duration may be compensated for by performing early digitization of the signal and by using dedicated algorithms to fit the pulse shape. Minimizing the processing electronics is of great advantage in the case of simultaneous PET/MR imaging where reduction of shielding requirements is of great importance.

It has also been shown that the performance of current SiPM designs is hindered by the restricted number of available cells in a given area and by the corresponding PDE. There should be a good compromise between these two factors that would guarantee sufficient dynamic range of detected wavelengths (large number of cells) and at the same time high detection probability (high PDE). Recent studies have demonstrated that a SiPM design involving a large number of cells per mm^2 is indeed possible and may lead to excellent performance in terms of energy and time resolution [52].

No degradation of the SiPM performance has been observed during simultaneous operation of a high gradient clinical MR sequence. A first assessment of the use of SiPM arrays for block detector readout has shown promising results even when the SiPM response is non-linear.

Efforts currently focus on the construction of a MR compatible SiPM-based PET detector module and different detector configurations are investigated, as shown in Figure 7.1.

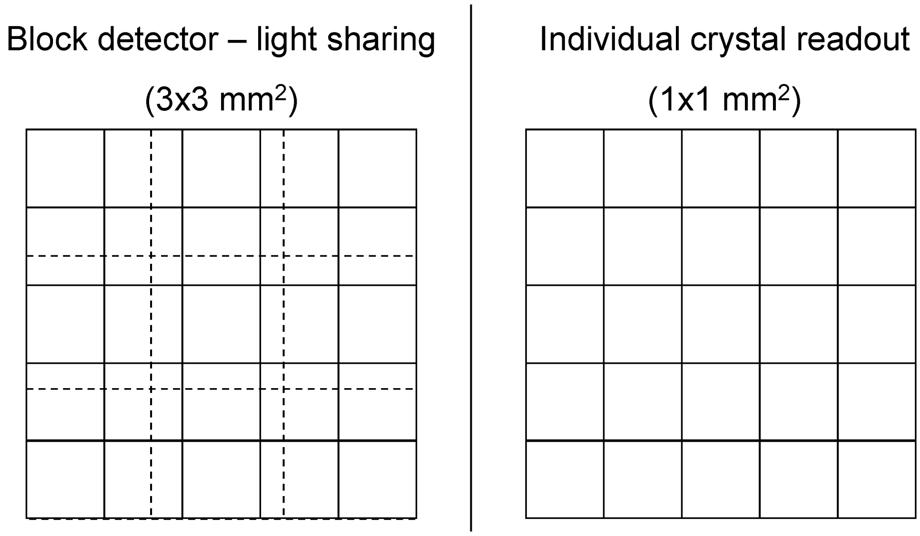

Figure 7.1: Block detector configuration based on 1×1 mm^2 scintillation crystals (solid lines) read out by 3×3 mm^2 SiPMs (dashed lines) (left) and individual crystal readout by 1×1 mm^2 SiPMs (right).

Commercially available SiPM detectors with sensitive areas of 1×1 and 3×3 mm^2 allow for both the traditional block detector design and the individual crystal readout design similar to the one implemented in MADPET-II. Even though, as discussed in Chapter 5, readout of 1×1 mm^2 crystal pixels by 1×1 mm^2 SiPMs would be beneficial in terms of spatial resolution, the limited number of cells within the 1×1 mm^2 sensitive area becomes an evident challenge that needs to be taken into account when designing a high resolution detector module for PET.

Appendix A

Temperature coefficient of an LSO-APD detector

For the temperature range of interest for this study a linear dependence of the LSO light yield L on temperature T

$$L(T) = L_0 \cdot (1 - \alpha_{LSO} \cdot (T - T_0)) \tag{A.1}$$

and a linear dependence of the APD gain M on temperature T

$$M(T) = M_0 \cdot (1 - \alpha_{APD} \cdot (T - T_0)) \tag{A.2}$$

is assumed.

The LSO-APD detector signal is proportional to the product of the LSO light yield and the APD gain thus

$$\begin{aligned} signal_{LSO-APD}(T) \propto L(T) \cdot M(T) &= 1 - \alpha_{APD} \cdot (T - T_0) - \alpha_{LSO} \cdot (T - T_0) + \\ &+ \alpha_{APD} \cdot \alpha_{LSO} \cdot (T - T_0)^2 \approx 1 - (\alpha_{LSO} + \alpha_{APD}) \cdot (T - T_0) \end{aligned} \tag{A.3}$$

Assuming small temperature coefficients α_{LSO} and α_{APD}, the quadratic term $\alpha_{APD} \cdot \alpha_{LSO} \cdot (T - T_0)^2$ may be neglected.

Appendix B

An approximate estimation of the effect of saturation and recovery time on the SiPM signal

Let us assume N_{inc} optical photons which are instantly incident to the sensitive area of a SiPM with N_{cell} total number of cells. Based following conditions:

1. every cell may detect optical photons independent of the other cells with a constant probability and
2. assuming infinite recovery time of each cell, only one photon may be detected by that cell

the number of fired cells N_{fired} will be the sum of the probabilities $P_i(x)$ for photon detection over all N_{cell} cells of the SiPM:

$$N_{fired} = \sum_{i}^{N_{cells}} P_i(x) = N_{cells} \cdot P(x \geq 1) \tag{B.1}$$

According to the above mentioned conditions the SiPM may be considered as a collection of binary devices each of which may succeed or may fail in detecting a photon with success probability equal to the PDE of the SiPM. Thus, photon detection by every cell of the SiPM obeys the Poisson law and the probability that at least one photon will be detected by a cell, when $\frac{N_{inc}}{N_{cell}}$ photons are incident to every cell, is given by the following equation:

$$P(x \geq 1) = 1 - P(0) \tag{B.2}$$

where

$$P(0) = P(x)_{x=0} = \left(\left(\frac{N_{inc} \cdot PDE}{N_{cell}} \right)^{x} \cdot \frac{1}{x!} \cdot e^{-\frac{N_{inc} \cdot PDE}{N_{cell}}} \right)_{x=0} = e^{-\frac{N_{inc} \cdot PDE}{N_{cell}}} \tag{B.3}$$

From equations B.1, B.2 and B.3 the number of fired cells is calculated to be

$$N_{fired} = N_{cells} \cdot \left(1 - e^{-\frac{N_{inc} \cdot PDE}{N_{cell}}}\right) \tag{B.4}$$

The above analysis is valid in the case that the optical photons are instantly incident to the sensitive area of the SiPM. In the case of extended duration of the incident light pulse, N_{inc} should be replaced by $\frac{dN_{inc}}{dt} \cdot t$ thus yielding

$$N_{fired} = N_{cells} \cdot \left(1 - e^{-\frac{\frac{dN_{inc}}{dt} \cdot t \cdot PDE}{N_{cell}}}\right) \tag{B.5}$$

where $\frac{dN_{inc}}{dt}$ is the incident photon rate and t is the light pulse duration.
If the finite recovery time of each cell τ is taken into account, the photon detection probability during the infinitively small time interval (dt, 2dt) for the cells that have already fired during the preceding time interval (0, dt) needs to be convolved with the recovery $1 - e^{-\frac{dt}{\tau}}$ of each cell. In this case the photon detection probability of each cell deviates from the Poisson probability defined in equations B.2 and B.3 and the postulates 1 and 2 described above are no longer valid. Summation of the photon detection probabilities over all time intervals dt and all cells N_{cells} yields in a first approximation Equation 6.2.

Bibliography

[1] EG&G ORTEC Principles and applications of timing spectroscopy. *Application Note AN-42*. (Cited on pages 28 and 41.)

[2] MPPC Multi-Pixel Photon Counter. *Hamamatsu Photonics*, 2007. (Cited on pages 57, 67, and 97.)

[3] G. B. Arfken and H. J. Weber. *Mathematical Methods For Physicists*. Academic Press, 4th edition, 1995. (Cited on page 73.)

[4] M. Balzerzyk, M. Moszynski, M. Kapusta, D. Wolski, J. Pawelke, and C. L. Melcher. YSO, LSO, GSO and LGSO. A Study of Energy Resolution and Nonproportionality. *IEEE Transactions on Nuclear Science*, 47:1319–1323, 2000. (Cited on page 72.)

[5] H. H. Barrett and K. J. Myers. *Foundations of image science*. Wiley Interscience, 1st edition, 2004. (Cited on pages 72 and 91.)

[6] S. Berko and F. L. Hereford. Experimental Studies of Positron Interactions in Solids and Liquids. *Reviews of Modern Physics*, 28(3):299–307, 1956. (Cited on page 6.)

[7] D. M. Binkley. Optimization of Scintillation-Detector Timing Systems Using Monte Carlo Analysis. *IEEE Transactions on Nuclear Science*, 41:386–393, 1994. (Cited on page 28.)

[8] D. M. Binkley. Performance of Non-Delay-Line Constant-Fraction Discriminator Timing Circuits. *IEEE Transactions on Nuclear Science*, 41:1169–1175, 1994. (Cited on page 28.)

[9] D. M. Binkley, B. S. Puckett, B. K. Swann, J. M. Rochelle, M. S. Musrock, and M. E. Casey. A 10-Mc/s, 0.5-m CMOS Constant-Fraction Discriminator Having Built-In Pulse Tail Cancellation. *IEEE Transactions on Nuclear Science*, 49:1130–1140, 2002. (Cited on page 28.)

[10] J. B. Birks. *The Theory and Practice of Scintillation Counting*. Wiley, 1964. (Cited on page 58.)

[11] G. Böning. *Verbesserte statistische Bildrekonstruktion für die hochauflösende PET: Bestimmung der Systemmatrix aus Monte Carlo Simulationen, Validierung und Anwendung auf TierMessungen, sowie Erweiterung für einen Doppellagen-Tomographen*. Phd thesis, Technische Universität München, 2002. (Cited on page 37.)

[12] A. Bousselham and C. Bohm. Sampling Pulses for Optimal Timing. *IEEE Transactions on Nuclear Science*, 54(2):320–326, 2007. (Cited on page 98.)

[13] I. Britvitch, E. Lorenz, A. Olshevski, D. Renker, Z. Sadygov, R. Scheuermann, A. Stoykov, A. Werner, I. Zheleznykh, and V. Zhuk. Study of avalanche microchannel photodiodes for use in scintillation detectors. *Journal of Instrumentation, P08002*, 1, 2006. (Cited on page 88.)

[14] I. Britvitch, Y. Musienko, and D. Renker. Investigation of a photon counting avalanche photodiode from Hamamatsu photonics. *Nuclear Instruments and Methods A*, 567:276–280, 2006. (Cited on page 15.)

[15] I. Britvitch and D. Renker. Measurements of the recovery time of Geiger-mode avalanche photodiodes. *Nuclear Instruments and Methods A*, 567:260–263, 2006. (Cited on page 91.)

[16] T. F. Budinger. Time-of-flight positron emission tomography: Status relative to conventional PET. *Journal of Nuclear Medicine*, 47:73–78, 1983. (Cited on page 97.)

[17] P. Buzhan, B. Dolgoshein, L. Filatov, A Ilyin, V. Kantzerov, V. Kaplin, A. Karakash, F. Kayumov, S. Klemin, E. Popova, and S. Smirnov. Silicon Photomultiplier and its possible applications. *Nuclear Instruments and Methods A*, 504:48–52, 2003. (Cited on page 88.)

[18] P. Buzhan, B. Dolgoshein, A. Ilyin, V. Kantserov, V. Kaplin, A. Karakash, A. Pleshko, E. Popova, S. Smirnov, and Y. Volkov. An advanced study of silicon photomultiplier. *ICFA Instrumentation Bulletin*, 23:28–41, 2001. (Cited on pages 15 and 91.)

[19] J. Cadorette, S. Rodrigue, and R. Lecomte. Tuning of avalanche photodiode PET camera. *IEEE Transactions on Nuclear Science*, 40:1062–1066, 1993. (Cited on page 74.)

[20] M. E. Casey, C. Reynolds, D. M. Binkley, and J. M. Rochelle. Analysis of timing performance for an APD-LSO scintillation detector. *Nuclear Instruments and Methods A*, 504:143–148, 2003. (Cited on page 98.)

[21] C. Catana, Y. Wu, M. S. Judenhofer, J. Qi, and S. R. Cherry. Simultaneous Acquisition of Multislice PET and MR Images: Initial Results with a MR-Compatible PET Scanner. *Journal of Nuclear Medicine*, 47(12):1968–1976, 2006. (Cited on page 3.)

[22] S. R. Cherry. Multimodality In Vivo Imaging Systems: Twice the Power or Double the Trouble? *Annu. Rev. Biomed. Eng.*, ANRV281-BE08-02:2–27, 2006. (Cited on page 2.)

[23] S. R. Cherry, J. A. Sorenson, and M. E. Phelps. *Physics in Nuclear Medicine*. Saunders, 3rd edition, 2004. (Cited on page 8.)

[24] A. M. Cooper, G. J. Laidlaw, and B. G. Hogg. Oxygen Quenching of Positron Lifetimes in Liquids. *Journal of Chemical Physics*, 46:2441–2442, 1967. (Cited on page 6.)

[25] F. Corsi, C Marzocca, A. Perotta, A. Dragone, M. Foresta, A. Del Guerra, S. Marcatilt, G. LLosa, G. Collazzuol, G-F. Dalla Betta, N. Dinu, C. Piemonte, G Pignatel, and G. Levi. Electrical Characterization of Silicon Photo-Multiplier Detectors for Optimal Front-End Design. *NSS/MIC Conference Record, San Diego, California*, 2006. (Cited on page 15.)

[26] S. Cova, M. Ghioni, A. Lacaita, C. Samori, and F. Zappa. Avalanche photodiodes and quenching circuits for single-photon detection. *Journal of Applied Optics*, 35(12):1956–1976, 1996. (Cited on page 88.)

[27] S. DeBenedetti and R. T. Siegel. The Three-Photon Annihilation of Positron and Electrons. *Physical Review*, 94(4):955–959, 1954. (Cited on page 6.)

[28] B. Dolgoshein, V. Balagura, P. Buzhan, M. Danilov, L. Filatov, E. Garutti, M. Groll, A. Ilyin nd V. Kantserov, V. Kaplin, A. Karakash, F. Kayumov, S. Klemin, V. Korbel, H. Meyer, R. Mizuk, V. Mogunov, E. Novikov, P. Pakhlov, E. Popova, V. Rusinov, F. Sefkow, E. Tarkovsky, I. Tikhomirov, and Calice/SiPM Collaboration. Status report on silicon photomultiplier development and its applications. *Nuclear Instruments and Methods A*, 563:368–376, 2006. (Cited on page 15.)

[29] E. Garutti et al. Magnetic Field Dependence Studies for Silicon Photomultiplier. *LC-DET-2004-025*. (Cited on page 15.)

[30] G. Germano and E. J. Hoffman. A Study of Data Loss and Mispositioning due to Pileup in 2-D Detectors in PET. *IEEE Transactions on Nuclear Science*, 37(2):671–675, 1990. (Cited on page 23.)

[31] E. Gramsch, E. M. Gullikson, W. W. Moses, and R. Avila. Operating characteristics of avalanche photodiodes for PET systems. *NSS/MIC Conference Record*, 1996. (Cited on page 73.)

[32] D. J. Herbert, N. D'Ascenzo, N. Belcari, A. Del Guerra, F. Morsani, and V. Saveliev. Study of SiPM as a potential photodetector for scintillation readout. *Nuclear Instruments and Methods A*, 567:356–359, 2006. (Cited on page 88.)

[33] D. J. Herbert, V. Saveliev, N. Belcari, N. D'Ascenzo, A. Del Guerra, and A. Golovin. First Results of Scintillator Readout With Silicon Photomultiplier. *IEEE Transactions on Nuclear Science*, 53:389–394, 2006. (Cited on page 88.)

[34] E. J. Hoffman, T. M. Guerrero, G. Germano, W. M. Digby, and M. Dahlbom. PET System Calibrations and Corrections for Quantitative and Spatially Accurate Images. *IEEE Transactions on Nuclear Science*, 36(1):1108–1112, 1989. (Cited on page 11.)

[35] E. J. Hoffman, S-C. Huang, M. E. Phelps, and D. E. Kuhl. Quantitation in Positron Emission Computed Tomography: 4. Effect of Accidental Coincidences. *Journal of Computed Assisted Tomography*, 5(3):391–400, 1981. (Cited on page 28.)

[36] B. Hopkins and T. W. Zerda. Oxygen Quenching of Positronium in Silica Gels. *Physics Letters A*, 145(2,3):141–145, 1990. (Cited on page 6.)

[37] M. C. Huisman, S. Reder, A. W. Weber, S. I. Ziegler, and M. Schwaiger. Performance evaluation of the Philips MOSAIC small animal PET scanner. *European Journal of Nuclear Medicine*, 34:532–540, 2007. (Cited on page 14.)

[38] A. P. Jeavons, R. A. Chandler, and C. A. R. Dettmar. A 3D HIDAC-PET Camera with Sub-millimetre Resolution for Imaging Small Animals. *IEEE Transactions on Nuclear Science*, 46(3):468–473, 1999. (Cited on page 16.)

[39] M. S. Judenhofer, C. Catana, B. K. Swann, S. B. Siegel, W.-I. Jung, R. E. Nutt, S. R. Cherry, C. D. Claussen, and B. J. Pichler. PET/MR Images Acquired with a Compact MR-compatible PET Detector in a 7-T Magnet. *Radiology*, 244(3):807–814, 2000. (Cited on pages 3 and 103.)

[40] K. Kacperski and N. M. Spyrou. Performance of three-photon PET imaging: Monte Carlo simulations. *Physics in Medicine and Biology*, 50:5679–5695, 2005. (Cited on page 6.)

[41] M. Kapusta, M. Moszynski, M. Balzerzyk, K. Lesniewski, and M. Szawloski. Avalanche Photodiodes in Scintillation Detection for High Resolution PET. *IEEE Transactions on Nuclear Science*, 47:2029–2033, 2000. (Cited on page 71.)

[42] G. F. Knoll. *Radiation Detection and Measurement*. Pergamon press, 3rd edition, 2001. (Cited on pages 28, 32, 44, 58, 91, and 96.)

[43] A. Kuhn, S. Surti, J. S. Karp, P. S. Raby, K. S. Shah, A. E. Perkins, and G. Muehllehner. Design of a Lanthanium Bromide Detector for Time-of-Flight PET. *IEEE Transactions on Nuclear Science*, 51(5):2550–2556, 2004. (Cited on page 97.)

[44] A. L. Lacaita, F. Zappa, S. Bigliardi, and M. Manfredi. On the Bremsstrahlung origin of Hot-Carrier-Induced Photons in Silicon Devices. *IEEE Transactions on Electron Devices*, 40(3):577–582, 1993. (Cited on page 98.)

[45] R. M. Leahy and J. Qi. Statistical approaches in quantitative positron emission tomography. *Statistics and Computing*, 10:147–165, 1999. (Cited on page 37.)

[46] R. Lecomte, J. Cadorette, P. Richard, S. Rodrigue, and D. Rouleau. Design and Engineering Aspects of a High Resolution Positron Tomograph for Small Animal Imaging. *IEEE Transactions on Nuclear Science*, 41:1446–1452, 1994. (Cited on page 67.)

[47] R. Lecomte, C. Pepin, D. Rouleau, A. Saoudi, M. S. Andreaco, M. Casey, R. Nutt, H. Dautet, and P. P. Webb. Investigation of GSO, LSO and YSO scintillators using reverse avalanche photodiodes. *IEEE Transactions on Nuclear Science*, 45(3):478–482, 1998. (Cited on page 71.)

[48] W. R. Leo. *Techniques for Nuclear and Particle Physics Experiments*. Springer-Verlag, 2nd edition, 1994. (Cited on page 28.)

[49] C. S. Levin. Design of a high-resolution and high-sensitivity scintillation crystal array for PET with nearly complete light collection. *IEEE Transactions on Nuclear Science*, 49:2236–2243, 2002. (Cited on page 83.)

[50] C. S. Levin, A. M. K. Foudray, P. D. Olcott, and F. Habte. Investigation of Position Sensitive Avalanche Photodiodes for a New High-Resolution PET Detector Design. *IEEE Transactions on Nuclear Science*, 51(3):805–810, 2004. (Cited on page 83.)

[51] C. S. Levin and E. J. Hoffman. Calculation of positron range and its effect on the fundamental limit of positron emission tomography system spatial resolution. *Physics in Medicine and Biology*, 44:781–799, 1999. (Cited on page 6.)

[52] E. Lorenz, I. Britvich, D. Ferenc, N. Otte, D. Renker, Z. Sadygov, and A. Stoykov. Some studies for a development of a small animal PET based on LYSO crystals and Geiger mode-APDs. *Nuclear Instruments and Methods A*, 572:259–261, 2007. (Cited on page 103.)

[53] L. Ludhova, F.D. Amaro, A. Antognini, F. Biraben, J.M.R. Cardoso, C.A.N. Conde, D.S. Covita, A. Dax, S. Dhawan, L.M.P Fernandes, T.W. Hänsch, V.W. Hughes, O. Huot, P. Indelicato, L. Julien, P.E. Knowles, F. Kottmann, J.A.M. Lopes, Y.W. Liu, C.M.B Monteiro, F. Muhlhauser, F. Nez, R. Pohl, P. Rabinowitz, J.M.F. dos Santos, L.F. Schaller, D. Taqqu, and J.F.C.A Veloso. Planar LAAPDs: Temperature Dependence, Performance, and Application in Low Energy X-Ray Spectroscopy. *Nucl. Instr. Meth. A*, 540:169–179, 2005. (Cited on page 57.)

[54] A. Mann, B. Grube, I. Konorov, S. Paul, L. Schmidt, D. P. McElroy, and S. I. Ziegler. A Sampling ADC Data Acquisition System for Positron Emission Tomography. *IEEE Transactions on Nuclear Science*, 53(1):297–303, 2006. (Cited on pages 90 and 98.)

[55] D. P. McElroy, M. Hoose, W. Pimpl, V. Spanoudaki, T. Schüler, and S. I. Ziegler. A true singles list-mode data acquisition system for a small animal PET scanner with independent crystal readout. *Physics in Medicine and Biology*, 50:3323–3335, 2005. (Cited on page 33.)

[56] D. P. McElroy, W. Pimpl, B. J. Pichler, M. Rafecas, T. Schüler, and S. I. Ziegler. Characterization and Readout of MADPET-II detector modules: Validation of a unique design concept for high resolution small animal PET. *IEEE Transactions on Nuclear Science*, 52(1):199–204, 2005. (Cited on page 74.)

[57] D.P. McElroy, C.J. Thompson, V. Spanoudaki, and S.I. Ziegler. Use of a Central Positron Emitting Reference Source to Improve the Timing Alignment of a Singles List-Mode Small Animal PET Scanner. *IEEE Transactions on Nuclear Science*, 54:50–54, 2007. (Cited on pages 51 and 55.)

[58] R. J. McIntyre. Multiplication Noise in Uniform Avalanche Diodes. *IEEE Transactions on Electron Devices*, 13:164–168, 1966. (Cited on page 72.)

[59] C. L. Melcher. Scintillation Crystals for PET. *Journal of Nuclear Medicine*, 41:1051–1055, 2000. (Cited on page 77.)

[60] MINUIT home page. www.cern.ch/minuit. (Cited on page 54.)

[61] R. S. Miyaoka and T. K. Lewellen. Effect of Detector Scatter on the Decoding Accuracy of a DOI Detector Module. *IEEE Transactions on Nuclear Science*, 47(4):1614–1619, 2000. (Cited on page 23.)

[62] S. Moehrs, A. Del Guerra, D. J. Herbert, and M. A. Mandelkern. A detector head design for small-animal PET with silicon photomultipliers (SiPM). *Physics in Medicine and Biology*, 51:1113–1127, 2006. (Cited on page 88.)

[63] W. W. Moses, S. E. Derenzo, and T. F. Budinger. PET detector modules based on novel detector technologies. *Nuclear Instruments and Methods A*, 353:189–194, 1994. (Cited on page 16.)

[64] W. W. Moses and C. J. Thompson. Timing Calibration in PET Using a Time Alignment Probe. *IEEE Transactions on Nuclear Science*, 53(5):2660–2665, 2006. (Cited on page 55.)

[65] J-B. Mosset, O. Devroede, M. Krieguer, M. Rey, J-M. Vrieira, J.H. Jung, C. Kuntner, M. Streun, K. Ziemons, E. Auffray, R. Semper-Roldan, P. Lecoq, P. Bruyndonckx, J-F. Loude, S. Tavernier, and C. Morel. Development of an Optimized LSO/LuYAP Phoswich Detector Head for the Lausanne ClearPET Demonstrator. *IEEE Transactions on Nuclear Science*, 51(1):25–29, 2006. (Cited on page 18.)

[66] M. Moszynski, M. Kapusta, D. Wolski, and M. Szawloski. Energy Resolution of Scintillation Detectors Readout with Large Area Avalanche Photodiodes and Photomultipliers. *IEEE Transactions on Nuclear Science*, 45:472–477, 1998. (Cited on pages 71 and 72.)

[67] M. Moszynski, M. Szawloski, M. Kapusta, and M. Balcerzyk. Large Area Avalanche Photodiodes in Scintillation and X-rays Detection. *Nuclear Instruments and Methods A*, 485:504–521, 2002. (Cited on page 71.)

[68] J. D. Naud, T. A. Tombrello, C. L. Melcher, and J. S. Schweitzer. The Role of Cerium Sites in the Scintillation Mechanism of LSO. *IEEE Transactions on Nuclear Science*, 43:1324–1328, 1996. (Cited on pages 58, 61, and 72.)

[69] J. M. Ollinger. Detector Efficiency and Compton Scatter in Fully 3D PET. *IEEE Transactions on Nuclear Science*, 42(4):1168–1173, 1995. (Cited on page 11.)

[70] A. Ore and J. L. Powell. Three-Photon Annihilation of an Electron-Positron Pair. *Physical Review*, 75(11):1696–1699, 1949. (Cited on page 6.)

[71] A. N. Otte, J. Barral, B. Dolgoshein, J. Hose, S. Klemin, E. Lorenz, R. Mizroyan, E. Popova, and M. Teshima. A test of silicon photomultipliers as readout for PET. *Nuclear Instruments and Methods A*, 545:705–715, 2005. (Cited on page 88.)

[72] N. Otte, B. Dolgoshein, J. Hose, S. Klemin, E. Lorenz, R. Mizroyan, E. Popova, and M. Teshima. The SiPM- A new Photon Detector for PET. *Nuclear Physics B Suppl*, 150:417–420, 2006. (Cited on page 88.)

[73] B. J. Pichler, F. Bernecker, G. Böning, M. Rafecas, W. Pimpl, M. Schwaiger, E. Lorenz, and S. I. Ziegler. A 4 × 8 APD Array, Consisting of Two Monolithic Silicon Wafers, Coupled to a 32-Channel LSO Matrix for High-Resolution PET. *IEEE Transactions on Nuclear Science*, 48:1391–1396, 2001. (Cited on pages 25, 74, and 87.)

[74] B. J. Pichler, M. S. Judenhofer, C. Catana, J. H. Walton, M. Kneilling, R. E. Nutt, S. B. Siegel, C. D. Claussen, and S. R. Cherry. Performance Test of an LSO-APD Detector in a 7-T MRI Scanner for Simultaneous PET/MRI. *Journal of Nuclear Medicine*, 47(4):639–647, 2006. (Cited on pages 3 and 87.)

[75] B. J. Pichler, W. Pimpl, W. Buttler, L. Kotoulas, G. Böning, M. Rafecas, E. Lorenz, and S. I. Ziegler. Integrated Low-Noise Low-Power Fast Charge-Sensitive Preamplifier for Avalanche Photodiodes in JFET-CMOS Technology. *IEEE Transactions on Nuclear Science*, 48:2370–2374, 2001. (Cited on pages 24, 73, and 94.)

[76] B. J. Pichler, B. K. Swann, J. Rochelle, R. E. Nutt, S. R. Nutt, S. R. Cherry, and S. B. Siegel. Lutetium oxyorthosilicate block detector readout by avalanche photodiode arrays for high resolution animal PET. *Physics in Medicine and Biology*, 49:4305–4319, 2004. (Cited on pages 17 and 87.)

[77] B.J. Pichler. *Entwiklung eines Detektors für die hochauflösende Positronen-Emissions-Tomographie basierend auf Lutetium-Oxxyorthosilikat-Szintillatoren, Lawinen-Photodioden-Matrizen, integrierter Elektronik und Doppellagenauslese*. Phd thesis, Technische Universität München, 2001. (Cited on page 24.)

[78] C. Piemonte, R. Battiston, M. Boscardin, G-F Dalla Betta, A. Del Guerrra, N. Dinu, A. Pozza, and N. Zorzi. Characterization of the First Prototypes of Silicon Photomultiplier Fabricated at ITC-irst. *IEEE Transactions on Nuclear Science*, 54(1):236–244, 2007. (Cited on page 15.)

[79] J.-F. Pratte, G. De Geronimo, S. Junnakar, P. O'Connor, B. Yu, S. Robert, V. Radeka, G. Woody, Stoll S., Vaska P., A. Kandasamy, R. Lecomte, and R. Fontaine. Front-End Electronics for the RatCap Mobile Animal PET Scanner. *IEEE Transactions on Nuclear Science*, 51:1318–1323, 2004. (Cited on page 28.)

[80] W. H. Press, S. A. Teukolsky, W. T. Vetterling, and B. Flannery. *Numerical Recipes in C*. Cambridge University Press, 2nd edition, 2002. (Cited on page 54.)

[81] V. Radeka. Low noise techniques in detectors. *Ann. Rev. Nucl. Part. Sci.*, 38:217–277, 1998. (Cited on page 73.)

[82] M. Rafecas. *High Resolution Animal PET with Granulated Detectors: Pre-reconstruction Processing and Evaluation of Novel Design Options*. Phd thesis, Universitat de València, 2001. (Cited on pages 24, 26, and 84.)

[83] M. Rafecas, G. Böning, B. J. Pichler, E. Lorenz amd M. Schwaiger, and S. I. Ziegler. Inter-crystal scatter in a dual layer, high resolution LSO-APD positron emission tomograph. *Physics in Medicine and Biology*, 48:821–848, 2003. (Cited on page 82.)

[84] M. Rafecas, G. Böning, B. J. Pichler, E. Lorentz, M. Schwaiger, and S.I. Ziegler. A Monte Carlo Study of High-Resolution PET with Granulated Dual-Layer Detectors. *IEEE Transactions on Nuclear Science*, 48(4):1490–1495, 2001. (Cited on page 18.)

[85] M. Rafecas, B. Mosler, M. Dietz, M. Pogl, A. Stamatakis, D. P. McElroy, and S.I. Ziegler. Use of a Monte Carlo-based probability matrix for 3-D iterative reconstruction of MADPET-II data. *IEEE Transactions on Nuclear Science*, 51(2):2597–2605, 2004. (Cited on page 37.)

[86] D. Renker. Geiger-mode avalanche photodiodes, history, properties and problems. *Nuclear Instruments and Methods A*, 567:48–56, 2006. (Cited on page 15.)

[87] A. Saoudi, C. M. Pepin, and R. Lecomte. Study of Light Collection in Multi-Crystal Detectors. *IEEE Transactions on Nuclear Science*, 47(4):1634–1639, 2000. (Cited on page 26.)

[88] V. Saveliev. The recent development and study of silicon photomultiplier. *Nuclear Instruments and Methods A*, 535:528–532, 2004. (Cited on page 15.)

[89] C. Scheiber and G. C. Giakos. Medical applications of CdTe and CdZnTe detectors. *Nuclear Instruments and Methods A*, 458:12–25, 2001. (Cited on page 16.)

[90] Y. Shao, S. R. Cherry, S. Siegel, and R. W. Silverman. A study of Inter-Crystal Scater in Small Scintillator Arrays Designed for high Resolution PET Imaging. *IEEE Transactions on Nuclear Science*, 43(3):1938–1944, 1996. (Cited on page 23.)

[91] Y. Shao, K. Meadors, R. W. Silverman, R. Farrell, L. Cirigano, R. Grazioso, K. S. Shah, and S. R. Cherry. Dual APD Array Readout of LSO Crystals: Optimization of Crystal Surface Treatment. *IEEE Transactions on Nuclear Science*, 49(3):649–654, 2002. (Cited on page 18.)

[92] R. Slates, A. Chatziioannou, B. Fehlberg, T. Lee, and S. Cherry. Chemical Polishing of LSO Crystals to Increase Light Output. *IEEE Transactions on Nuclear Science*, 47(3):1018–1023, 2000. (Cited on page 26.)

[93] V. Spanoudaki, D.P. McElroy, C.J. Thompson, and S.I. Ziegler. A Software Based Iterative Method of Improving the System Wide Timing Resolution of the MADPET-II Small Animal PET Tomograph. *Biomedizinische Technik, Proceedings of the 14th ICMP conference, Nürnberg*, 50:899–900, 2005. (Cited on pages 51 and 53.)

[94] J. R. Stickel and S. R. Cherry. High-Resolution PET detector design: modelling components of intrinsic resolution. *Physics in Medicine and Biology*, 50:179–195, 2005. (Cited on page 16.)

[95] J. R. Stickel, J. Qi, and S. R. Cherry. Fabrication and Characterization of a 0.5-mm Lutetium Oxyorthosilicate Detector Array for High-Resolution PET Applications. *Journal of Nuclear Medicine*, 48:115–121, 2007. (Cited on page 83.)

[96] A. Stoykov, Y. Musienko, A. Kuznetsov, S. Reucroft, and J. Swain. On the limited amplitude resolution of multipixel Geiger-mode APDs. *Journal of Instrumentation, P06005*, 2, 2007. (Cited on page 88.)

[97] M. Streun, G. Brandenburg, H. Larue, H. Saleh, E. Zimmermann, K. Ziemons, and H. Halling. Pulse Shape Discrimination of LSO and LuYAP Scintillators for Depth of Interaction Detection in PET. *IEEE Transactions on Nuclear Science*, 50(3):344–347, 2003. (Cited on page 18.)

[98] S. M. Sze. *Physics of Semiconductor Devices*. Wiley Interscience, 2nd edition, 1979. (Cited on pages 57, 70, 71, and 72.)

[99] Y.-C. Tai and R. Laforest. Instrumentation Aspects of Animal PET. *Annu. Rev. Biomed. Eng.*, 7:255–285, 2005. (Cited on page 3.)

[100] Y.-C. Tai, A. Ruangma, D. Rowland, S. Siegel, D. Newport, P. L. Chow, and R. Laforest. Performance Evaluation of the microPET Focus: A Third-Generation microPET scanner Dedicated to Animal Imaging. *Journal Of Nuclear Medicine*, 46:455–463, 2005. (Cited on page 14.)

[101] Y.-C. Tai, H. Wu, D. Pal, J. A. O'Sullivan, and S. Komarov. A sub-millimiter resolution full-ring micro-insert for microPET-F220. *Supplement to the Journal of Nuclear Medicine*, 48(6):39P, 2007. (Cited on page 83.)

[102] M. A. Tetrault, M. D. Lepage, N. Viscogliosi, F. Belanger, J. Cadorette, C. M. Pepin, R. Lecomte, and R. Fontaine. Real Time Coincidence Detection System for Digital High Resolution APD-based Animal PET scanner. *NSS/MIC Conference Record, Puerto Rico, USA*, pages 2850–2853, 2005. (Cited on page 37.)

[103] C. J. Thompson, M.-L. Camborde, and M. E. Casey. A Central Positron Source to Perform the Timing Alignment of Detectors in a PET Scanner. *IEEE Transactions on Nuclear Science*, 52(5):1300–1302, 2005. (Cited on page 55.)

[104] M. P. Tornai, G. Germano, and E. J. Hoffman. Positioning and energy response of PET block detectors with different light sharing schemes. *IEEE Transactions on Nuclear Science*, 41(4):1458–1463, 1994. (Cited on page 101.)

[105] I. Torres-Espallardo, M. Rafecas, V. Spanoudaki, D. P. McElroy, and S. I. Ziegler. Effect of Inter-Crystal Scatter on Estimation Methods for Random Coincidences and subsequent correction. *Submitted to Physics in Medicine and Biology, under review*, 2008. (Cited on pages 35 and 37.)

[106] I. Torres-Espallardo, M. Rafecas, V. Ch. Spanoudaki, D. P. McElroy, and S. I. Ziegler. Evaluation of different random estimation methods for the MADPET-II small animal PET scanner using GATE. *NSS/MIC Conference Record, San Diego, USA*, 5:3148–3150, 2006. (Cited on page 84.)

[107] I. Torres-Espallardo, V. Ch. Spanoudaki, M. Rafecas, J. Schirmer, and S. I. Ziegler. Quantification Issues in Imaging Data of MADPET-II small animal PET scanner using a System Matrix based on Monte Carlo Techniques. *NSS/MIC Conference Record, Hawaii, USA*, 2007. (Cited on page 84.)

[108] P. Vaska, S. P. Stoll, C. L. Woody, D. J. Schlyer, and S. Shokouhi. Effects of Intercrystal Crosstalk on Multielement LSO/APD Detectors. *IEEE Transactions on Nuclear Science*, 50:362–366, 2003. (Cited on page 23.)

[109] P. Vaska, C. L. Woody, D. J. Schlyer, S. Shokouhi, S. P. Stoll, J.-F. Pratte, P. O'Connor, S. S. Junnarkar, S. Rescia, B. Yu, M. Purschke, A. Kandasamy, A. Villanueva, A. Kriplani, V. Radeka, N. Volkow, R. Lecomte, and R. Fontaine. RatCAP: Miniaturized Head-Mounted PET for Conscious Rodent Brain Imaging. *IEEE Transactions on Nuclear Science*, 51(5):2718–2722, 2004. (Cited on page 4.)

[110] Y. Wang, J. Seidel, B. M. W. Tsui, J. J. Vaquero, and M. G. Poper. Performance evaluation of the GE Healthcare eXplore VISTA Dual-Ring Small-Animal PET Scanner. *Journal of Nuclear Medicine*, 47:1891–1900, 2006. (Cited on page 14.)

[111] S. Weber, D. Christ, M. Kurzeja, R. Engels, G. Kemmerling, and H. Halling. Comparison of LuYAP, LSO, and BGO as Scintillators for High Resolution PET Detectors. *IEEE Transactions on Nuclear Science*, 50:1370–1372, 2003. (Cited on page 57.)

[112] Y. Yang, P. A. Dokhale, R. W. Silverman, K. S. Shah, M. A. McClish, R. Farrell, G. Entine, and S. R. Cherry. Depth of interaction measurements for a high resolution PET detector using position sensitive avalanche photodiodes. *Physics in Medicine and Biology*, 51:2131–2142, 2006. (Cited on page 18.)

[113] M. Yokohama, T. Nobuhara, M. Taguchi, T. Nakaya, T. Murakami, T. Nakadaira, K. Yoshimura, K. Kawagoe, Y. Tamura, T. Iijima, Y. Mazuka, K. Miyabayashi, S. Iba, H. Miyata, and T. Takeshita. Development of Multi-Pixel Photon Counters. *SNIC Symposium, Stanford, California*, 2006. (Cited on page 15.)

[114] S. I. Ziegler, B. J. Pichler, G. Böning, M. Rafecas, W. Pimpl, E. Lorenz, N. Schmitz, and M. Schwaiger. A prototype high-resolution animal positron tomograph with avalanche photodiode arrays and LSO crystals. *European Journal of Nuclear Medicine*, 28:136–143, 2001. (Cited on page 87.)

Acknowledgments

First of all I would like to thank my boss, Dr. Sibylle Ziegler, one of the most knowledgeable persons I have ever met, who accepted me in her group and gave me the opportunity to work in this exciting field. Sibylle, there are no proper words to express to you my gratitude for being a great teacher but also for being so supportive in all aspects, for tolerating my emotional "bursts" and always keeping me motivated. I feel very proud having been your student for over four years.

I am very thankful to Prof. Stephan Paul who enabled the realization of this thesis in the E18 chair for experimental physics. My very special thanks would go to Prof. Fridjof Nüsslin, who is the reason I came to Germany. Without his support I would not have made it. Herzlichen Dank Prof. Nüsslin.

I feel extremely thankful towards all of my direct colleagues and roommates in the clinic; working and interacting with them helped me learn a lot about research, as well as about myself. Many thanks to my closest colleague Irene Torres-Espallardo, to Alexander Mann whose constant help has been invaluable, to Dr. David McElroy, Dr. Magdalena Rafecas, Dr. Marc Huisman, Dr. Maria-Jose Martinez, Marisa Basañez-Borgert, Axel Weber, Ralph Bundschuh and Axel Martinez-Möller. I would also like to thank Igor Konorov as well as Dr. Nepomuk Otte, for their help and the fruitful discussions we had.

It has also been a pleasure to work with many new colleagues the last months: Arne Tapfer, Melanie Hohberg, Jozef Pulko, Astrid Verloyen and Sebastian Fürst. Even though we met and had to work under the pressure of the stressful period before the thesis defense, thank you so much for all the help and support. I am extremely thankful to Dr. Gaspar Delso and Dr. Jasmine Schirmer who helped me a lot improving the english and the appearance of this manuscript.

I would also greatly acknowledge the help of Markus Schneider and Fritz Weigl with whom I have spent many hours assembling and testing hardware until late at night. Danke Markus, danke Herr Weigl!

Last but not least I would like to thank the most precious people in my life, my sister, Eirini, to whom this work is dedicated and my parents Eleni and Charalampos, the greatest parents one could wish for.. Sas efxaristw